Conceptual Design of an Aircraft Using Hydrogen in a Dual-Fuel Configuration

MSc Thesis

M.G. Kadijk

Delft University of Technology

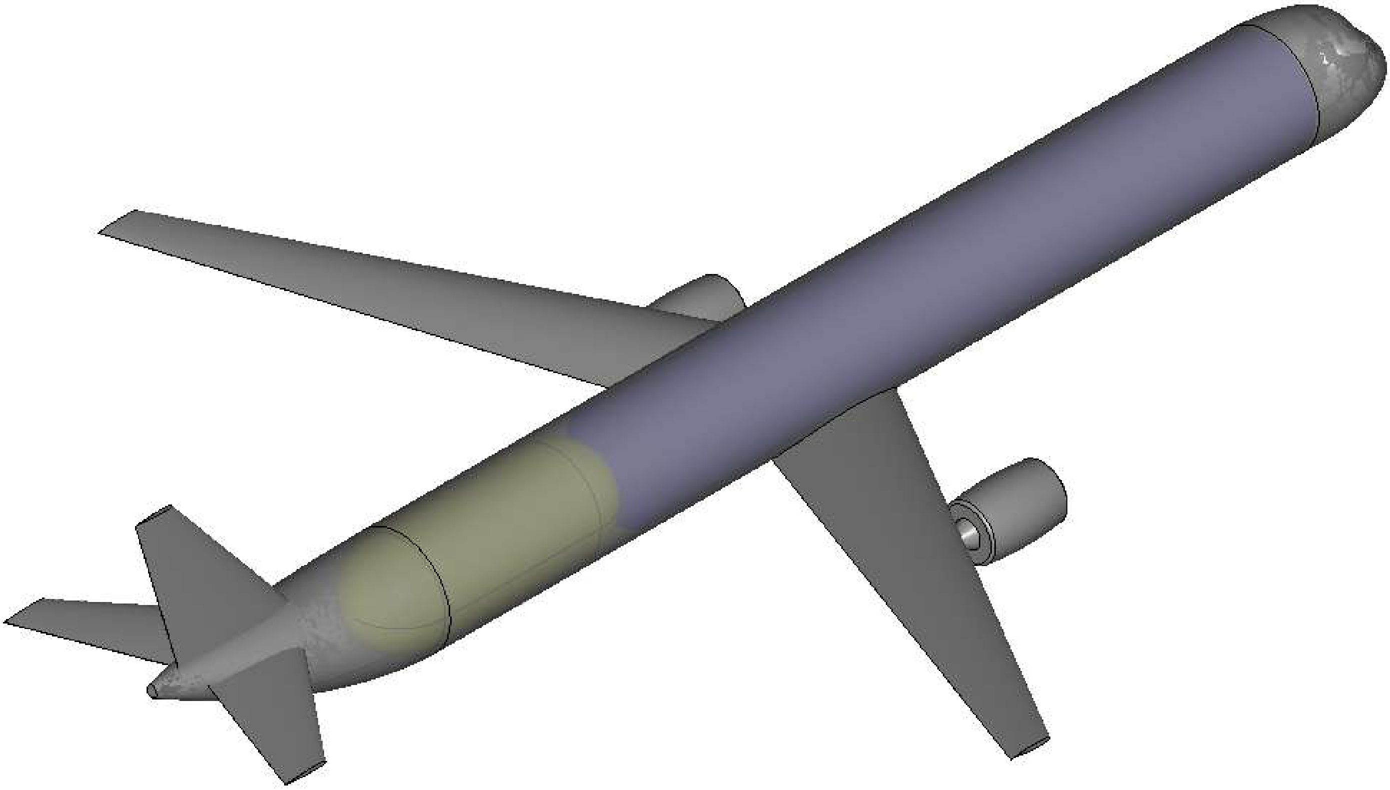

TUDelft

Conceptual Design of an Aircraft Using Hydrogen in a Dual-Fuel Configuration

by

M.G. Kadijk

to obtain the degree of Master of Science in Aerospace Engineering
at Delft University of Technology,

to be defended publicly on Monday the 12th of January 2026 at 14:00.

Student number:	4874617	
Supervisors:	Dr. F. Oliviero	Delft University of Technology
	Dr.ir. W.J. Vankan	Royal Netherlands Aerospace Centre
Thesis committee:	Dr.ir. M.F.M. Hoogreef	Delft University of Technology, chair
	Dr.ing. P. Proesmans	Delft University of Technology
	Dr. F. Oliviero	Delft University of Technology
	Dr.ir. W.J. Vankan	Royal Netherlands Aerospace Centre

Cover Image: ParaPy model of a dual-fuel aircraft

Preface

This thesis marks the end of my time as a student at Delft University of Technology. A time that was challenging, required a lot of hard work and provided many learning opportunities. Above all, it was a time that I thoroughly enjoyed and look back on with great memories.

This thesis was performed at the Royal Netherlands Aerospace Centre. I am grateful for the opportunity to get to know this renowned research institute during this thesis. I would also like to take this opportunity to express my gratitude to my supervisors Fabrizio Oliviero and Jos Vankan for their guidance and support throughout the thesis process. The interesting discussions during meetings allowed me to critically reflect on my own work and make continuous improvements and progress.

Next to that, I would like to sincerely thank my friends for the all the joy they brought to my life over the past years. Also, I am forever grateful to my family and loved ones for their continuous and tireless support during my studies. Especially the last year during which I worked on this thesis has been tough and I could not have done it without you.

Maarten Kadijk
Delft, December 2025

Abstract

The aviation sector faces increasing pressure to significantly reduce its climate impact. Particularly in the medium-range narrowbody aircraft segment, which accounts for a large share of global passenger traffic and emissions, large gains can be made. While hydrogen propulsion offers the potential for zero in-flight CO_2 emissions, its implementation is challenged by volumetric storage penalties, operational limitations and infrastructure development. A dual-fuel aircraft concept, capable of operating on both liquid hydrogen and kerosene or sustainable aviation fuel (SAF), may provide a transitional solution that balances environmental benefits with operational flexibility. While previous studies into dual-fuel propulsion concepts showed the potential to reduce CO_2 emissions, a research gap was identified in the development of a conceptual aircraft design method employing sequential dual-fuel use throughout the mission.

This thesis investigates the impact of implementing a dual-fuel propulsion system using hydrogen and kerosene (or SAF replacement) on the design and performance of a medium-range narrowbody tube-and-wing turbofan aircraft. A parametric conceptual design model is developed using Python and the commercial ParaPy Python package, incorporating preliminary aircraft sizing, hydrogen tank structural and thermal modelling, aerodynamic analysis, engine performance modelling, mission analysis and well-to-wake energy and emission evaluation. Several fuel-use scenarios are evaluated, including full kerosene, full hydrogen, hydrogen-kerosene combinations, and varying fuel splits during cruise, for design ranges of 2500 km and 5000 km.

The results show that introducing dual-fuel capability mainly affects aircraft design through an increase in fuselage length due to hydrogen tank integration, with this effect being more pronounced at 5000 km than at 2500 km range. Across both ranges, increasing hydrogen use reduces total fuel weight, but increases operational empty weight, resulting in only small changes in maximum take-off weight due to these counteracting effects. Dual-fuel operation partially mitigates the fuselage length and passenger capacity penalties observed for full-hydrogen configurations at both ranges. Although tank-to-wake CO_2 emissions decrease with increasing hydrogen use, overall equivalent CO_2 emissions remain strongly dependent on hydrogen production pathways, with dual-fuel operation offering advantages over full-hydrogen concepts under near-term electricity grid assumptions. Overall, this study demonstrates that dual-fuel aircraft concepts offer a promising intermediate pathway towards aviation decarbonisation, enabling gradual integration of hydrogen while maintaining competitive operational performance.

Contents

List of Figures

List of Tables

Nomenclature

Abbreviations

Abbreviation	Definition
AC	Aerodynamic centre
APU	Auxiliary Power Unit
APSI	Accessory drives, powerplant controls, starting and ignition systems
AVL	Athena Vortex Lattice
CG	Centre of Gravity
CGR	Climb rate gradient
CI	Carbon Intensity
CO_2	Carbon dioxide
CS	Certification Specification
EASA	European Union Aviation Safety Agency
EW	Empty weight
FW	Fuel weight
GSP	Gas turbine Simulation Program
HW	Hydrogen weight
KW	Kerosene weight
LHV	Lower Heating Value
MAC	Mean aerodynamic chord
MASS	Mission, Aircraft and Systems Simulation
MTOW	Maximum take-off weight
NACA	National Advisory Committee for Aeronautics
NLR	Netherlands Aerospace Centre
NO_x	Nitrous oxide
OEI	One engine inoperative
OEW	Operational empty weight
PAX	Number of passengers
PW	Payload weight
RoC	Rate of climb
SAF	Sustainable Aviation Fuel
SEC	Specific energy consumption
SM	Static margin
TIT	Turbine inlet temperature
TLAR	Top-level aircraft requirement
TO	Take off
TOP	Take-Off Parameter
TTW	Tank-to-wake
WTT	Well-to-tank
WTW	Well-to-wake

Symbols

Symbol	Definition	Unit
Latin symbols		
A	Aspect ratio of wing	–
A_{HT}	Aspect ratio of horizontal tailplane	–
A_{VT}	Aspect ratio of vertical tailplane	–
b	Wing span	m
b_f	Fuselage width	m
b_{max}	Maximum wing span	m
b_n	Nacelle width	m
C_D	Drag coefficient	–
C_{D_0}	Zero-lift drag coefficient	–
$C_{D_{eng}}$	Engine drag coefficient	–
$C_{D_{0_{ht}}}$	Horizontal tailplane contribution to the zero-lift drag coefficient	–
C_{D_i}	Induced drag coefficient	–
$C_{D_{misc}}$	Miscellaneous drag coefficient	–
$C_{D_{nac}}$	Nacelle drag coefficient	–
C_{D_w}	Wave drag coefficient	–
$C_{D_{visc}}$	Viscous drag coefficient	–
$C_{D_{0_{vt}}}$	Vertical tailplane contribution to the zero-lift drag coefficient	–
C_f	Flat plate skin friction coefficient	–
$C_{f_{lam}}$	Laminar flat plate skin friction coefficient	–
$C_{f_{turb}}$	Turbulent flat plate skin friction coefficient	–
CI	Carbon intensity	kg$_{CO_2}$/MJ
C_l	Wing strip lift coefficient	–
C_L	Lift coefficient	–
$C_{L_{TO}}$	Take-off lift coefficient	–
$C_{L_{\alpha_h}}$	Lift curve slope of horizontal tail	1/deg
$C_{L_{\alpha_{A-h}}}$	Lift curve slope of the aircraft less horizontal tail	1/deg
CO_2eq	Equivalent CO_2 emissions	g/PAX/km
c_g	Geometric chord	m
c_r	Root chord length	m
c_t	Tip chord length	m
$\bar{c}$	MAC length	m
D	Drag	N
D	Engine diameter	m
D_{nac}	Nacelle diameter	m
D_{tank}	Tank diameter	m
d_f	Fuselage diameter	m
E	Endurance	s
E_{w-t}	Well-to-tank energy consumption	J
E_{t-w}	Tank-to-wake energy consumption	J
e	Oswald efficiency factor	–
e_l	Energy of hydrogen liquefaction	kWh/kg
e_w	Weld efficiency factor	–
e_0	Emissivity of tank surface	–
FF	Form factor	–
f	Equivalent parasite area	m^2
f	Fineness ratio	–
ff	Fuel weight fraction	–
g	Gravitational acceleration	m/s^2

Symbol	**Definition**	**Unit**
h	Altitude	m
h_f	Fuselage height	m
h_{rad}	Coefficient of heat transfer from radiation	W/m^2/K
k	Conductivity of tank layer	W/m/K
k	Skin roughness height	m
k_a	Thermal conductivity of air	W/m/K
$k_{boiloff}$	Scaling factor for boil-off rate	–
k_{dry}	Dry wing correction factor	–
k_n	Engine type correction factor	–
$k_{semidry}$	Semi-dry wing correction factor	–
k_{tc}	Scaling factor for fuselage tailcone length to diameter	–
L	Lift	N
L_{cyl}	Length of cylindrical centre section of the tank	m
L/D	Lift-to-drag ratio	–
$L/D\ midcruise$	Lift-to-drag ratio at the middle of the cruise phase	–
LHV	Lower heating value	J/kg
l	Characteristic length to compute Reynolds number	m
l_{fn}	Distance from fuselage nose to wing-fuselage intersection	m
l_{fus}	Fuselage length	m
l_{H2tank}	Length of fuselage hydrogen tank section	m
l_h	Moment arm horizontal tailplane	m
$l_h\ l_n$	Nacelle length	m
l_{nc}	Length of fuselage nose cone	m
l_{pax}	Length of fuselage passenger accommodation	m
l_{tank}	Total tank length	m
$l_{tank,cs}$	Length of tank centre section	m
l_{tc}	Length of fuselage tailcone	m
l_v	Moment arm vertical tailplane	m
M	Mach number	–
M_{fuel}	Fuel mass	kg
M_{cr}	Critical Mach number	–
M_{cruise}	Cruise Mach number	–
M_{DD}	Drag divergence Mach number	–
$M^{\dagger}$	Mach number for supercritical airfoils	–
m_{CO_2}	Mass of CO_2 emissions	kg
$m_{cap,tank}$	Weight of wing fuel tank capacity	kg
m_{emp}	Empennage weight	kg
$m_{engines}$	Engine weight	kg
$m_{fuelsys,H2}$	Weight of fuel system for H_2	kg
$m_{fuelsys,JetA1}$	Weight of fuel system for Jet-A1	kg
m_{fus}	Fuselage weight	kg
m_{gear}	Landing gear weight	
m_{H2}	Hydrogen weight	kg
m_{JetA}	Jet-A1 weight	kg
m_{tank}	Hydrogen tank weight	kg
m_w	Wing weight	kg
$\dot{m}_{boiloff}$	mass flow of hydrogen boil-off	kg/s
$\dot{m}_{cruise}$	Fuel mass flow rate at take-off	kg/s
$\dot{m}_{TO}$	Fuel mass flow rate at take-off	kg/s
N_{eng}	Number of engines	–
N_{ft}	Number of fuel tanks	–
N_{ult}	Ultimate load factor	–

Symbol	**Definition**	**Unit**
Nu	Nusselt number	–
n_{aisle}	Number of aisles	–
n_{SA}	Number of seats abreast	–
Pr	Prandtl number	–
P_{out}	Pressure outside the hydrogen tank	Pa
P_{vent}	Vent pressure of the hydrogen tank	Pa
Q	Interference factor for drag calculations	–
$\dot{Q}$	Heat flux rate	W
q	Dynamic pressure	Pa
R	Range	m
R	Thermal resistance	K/W
Ra	Rayleigh number	–
Re	Reynolds number	–
Re_{cutoff}	Cut-off Reynolds number	–
Re_{trans}	Transition Reynolds number	–
R_{air}	Thermal resistance of air layer	K/W
R_{conv}	Thermal resistance of convection	K/W
R_{cond}	Thermal resistance of conduction	K/W
R_{ins}	Thermal resistance of insulation layer	K/W
R_{rad}	Thermal resistance of radiation	K/W
R_{wall}	Thermal resistance of tank wall	K/W
R_1	Stress ratio at cryogenic temperatures at reverse loading conditions	–
R_2	Stress ratio at operational conditions	–
RoC	Rate of climb	m/s
r_{fus}	Fuselage radius	m
r_{shell}	Internal radius structural shell	m
r_{tank}	Total tank radius	m
r_0	Outer radius of tank layer	m
S	Wing area	m^2
SEC	Specific energy consumption	MJ/PAX/km
S_h	Horizontal tail surface area	m^2
S_{max}	Maximum wing surface area	m^2
S_{ref}	Reference wing surface area	m^2
S_v	Vertical tail surface area	m^2
S_{wet}	Wetted surface area	m^2
$s_{clearance}$	Clearance between outer seat armrest and cabin wall	m
s_{LF}	Landing field length	m
T_{amb}	Ambient temperature	K
T_{cruise}	Cruise thrust	N
T_{H_2}	Hydrogen temperature	K
T_{ins}	Insulation temperature	K
T_{TO}	Take-off thrust	N
T_{surf}	Outer surface temperature	K
$TSFC$	Thrust specific fuel consumption	kg/(N s)
T/W	Thrust loading	–
t	Thickness of tank layer	m
t_r	Thickness of wing root	m
t/c	Thickness-to-chord ratio	–
t_{cap}	Wall thickness of hemispherical cap	m
t_{ins}	Insulation thickness	m
$t_{shell,cs}$	Wall thickness of tank centre section	m
T_{t4}	Turbine inlet temperature	K

Symbol	Definition	Unit
V	Velocity	m/s
V_A	Approach velocity	m/s
V_{caps}	Volume of end caps	m^3
$V_{cap,tank}$	Volume of wing fuel tank capacity	m^3
V_h	Horizontal tail volume coefficient	–
V_{H2}	Hydrogen volume	m^3
V_h/V	Tail to wing velocity ratio	–
V_{stall}	Stall velocity	m/s
$V_{tank,allowance}$	Hydrogen volume corrected for allowances	m^3
V_v	Vertical tail volume coefficient	–
v_{climb}	Average climb velocity	m/s
W	Weight	kg
W/S	Wing loading	N/m^2
W_{apsi}	Weight of APSI	kg -
W_{fs}	Fuel system weight	kg
W_w	Wing weight	kg
W_{ZF}	Zero fuel weight	kg
w_{aisle}	Aisle width	m
$w_{armrest}$	Armrest width	m
w_{cabin}	Cabin width	m
w_f	Fuselage outer width	m
w_s	Seat width	m
X_{CG}	X-coordinate of centre of gravity	m
$X_{CG,aft}$	X-coordinate of the most aft centre of gravity	m
$X_{CG,fwd}$	X-coordinate of the most forward centre of gravity	m
X_{lemac}	X-coordinate of the leading edge of MAC	m
X_{np}	X-coordinate of neutral point	m
$X_{np,corr}$	X-coordinate of corrected neutral point	m
$\bar{x}_{ac}$	Non-dimensional X-position aerodynamic centre	–
$\bar{x}_{cg}$	Non-dimensional X-position centre of gravity	–
$(x/c)_m$	Chordwise position of maximum thickness	–
$\bar{Y}$	Spanwise position of MAC	
	Greek symbols	
α	Angle of attack	deg
α_a	Diffusivity of air	m^2/s
β	Volumetric thermal expansion coefficient	1/K
ΔH_e	Heat of evaporation	J/kg
ΔT	Temperature difference	K
δ_{lam}	Fraction of laminar flow	–
ε	Downwash angle	deg
η_e	Efficiency of hydrogen electrolysis	–
η_{tank}	Tank gravimetric efficiency index	–
κ_A	Korn factor	–
$\Lambda_{c/2}$	Half-chord sweep angle	deg
$\Lambda_{c/4}$	Quarter-chord sweep angle	deg
Λ_m	Sweep angle at maximum thickness	deg
λ	Wing taper ratio	–
λ_{HT}	Horizontal tailplane taper ratio	–
λ_{VT}	Vertical tailplane taper ratio	–
ν	Kinematic viscosity of air	m^2/s
ϕ	Fuel split	–
ρ	Density	kg/m^3
σ	Design stress tank shell	Pa
σ_b	Ultimate stress	Pa

Symbol	**Definition**	**Unit**
$\sigma_{a,-1}$	Stress corrected for reverse loading	Pa
σ_{a,R_1}	Design stress tank wall material	Pa
σ_{bolt}	Stefan-Boltzmann constant	W/m^2/K^4
τ	Ratio of thickness-to-chord ratio of wing tip and root	–

1

Introduction

In today's world, air travel has become an integral part of our society. It enables people to travel across the globe within 24 hours. In 2019, around 4.5 billion passengers used this mode of transport, thereby connecting societies and economies [1]. In other words, the aviation is an important interconnecting backbone of our society, and it is impossible to imagine a strongly connected world without it.

It is estimated that aviation is currently responsible for around 2.5% of global carbon dioxide emissions and 3.5% to global warming [2]. Over the past decades, aircraft have become substantially more fuel-efficient and less polluting. However, this improvement is more than compensated by the increasing demand for air travel, thereby raising concerns about the environmental impact of aviation [1]. Figure 1.1 reflects this trend and highlights the need for radically new technological developments that can help decarbonising aviation to meet emission reduction targets.

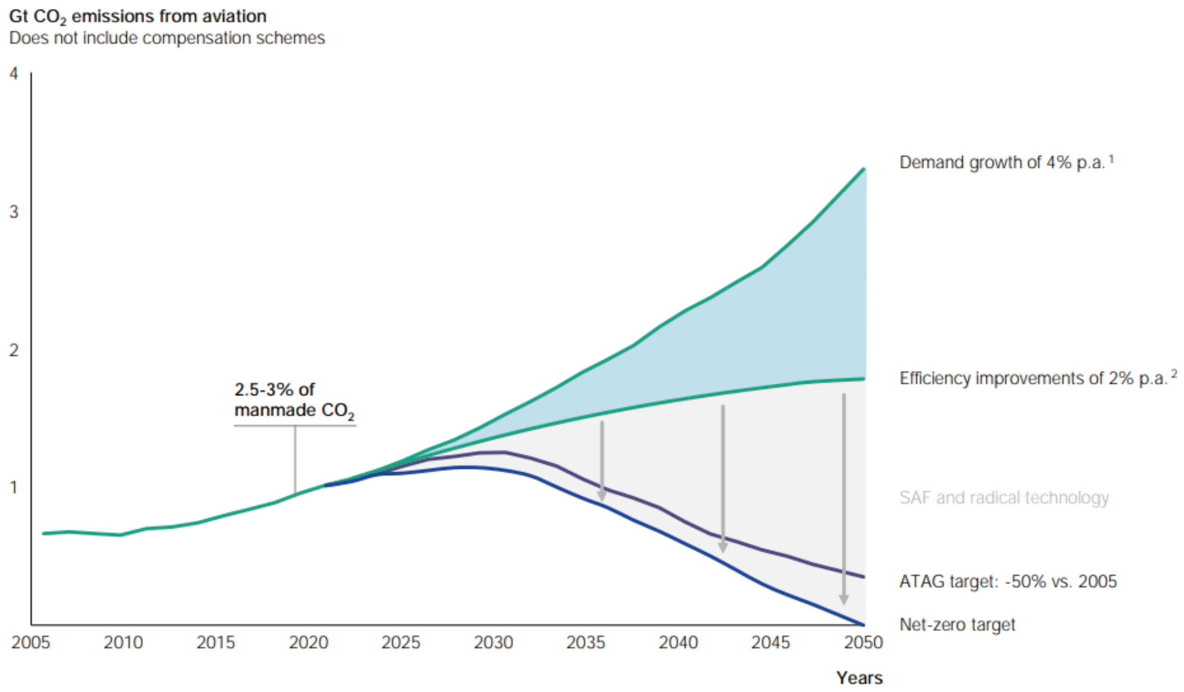

1. Assumption based on growth projections from ATAG, IATA, ICCT, WWF, UN
2. ICAO ambition incl. efficiency improvements in aircraft technology, operations and infrastructure

Figure 1.1: Projection of CO_2 emissions from aviation according to various scenarios and technology developments. Reprinted from [3]

There are several options for decarbonising technologies. First of all, battery-electric propulsion, but with current and near future battery energy densities, deemed unviable for the aircraft type considered in this study, i.e. for (short-)medium range [4]. Secondly, hydrogen propulsion. With the high energy density of hydrogen, this has potential. Focus will be on hydrogen storage in liquid form to the best possible specific energy, and propulsion using combustion in turbofan engines as these have higher specific power compared to fuel cells [5]. Finally, using Sustainable Aviation Fuel (SAF) can reduce climate impact in its life cycle and can be used in aircraft in similar fashion as conventional kerosene [6]. These alternative technologies illustrate that a range of decarbonisation pathways exists, but each comes with distinct challenges that influence feasibility, performance and implementation timelines.

The application of hydrogen as aviation fuel has been looked into in many previous studies, from retrofits in existing aircraft to more conceptual studies. However, payload and range are often negatively impacted by the implementation of large and heavy liquid hydrogen tanks, which harms the competitiveness of such aircraft compared to present-day technology and delays its implementation. This raises the question if a dual-fuel aircraft concept flying on both hydrogen and kerosene (or SAF replacement) proposes a good intermediate solution. The accompanying advantage is that in the energy transition towards a more hydrogen based economy this may help as an intermediate step, before shifting to hydrogen completely. Such a dual-fuel approach may offer operational flexibility while reducing the performance penalties associated with hydrogen-only aircraft, making it a potentially valuable transitional technology. Next to that, the risk and uncertainty around hydrogen infrastructure development highlights the interest of dual-fuel aircraft [7].

This study aims to better understand how dual-fuel capability affects both the aircraft design and operational performance and whether it can serve as a credible pathway towards long-term decarbonisation. To investigate this, a conceptual aircraft design of a turbofan-powered tube and wing aircraft that flies on both hydrogen and kerosene is modelled. This study focuses on medium-range narrowbody aircraft, which are used to operate 60% of passenger flights [8]. Next to that, it is estimated that 50% of CO_2 emissions from commercial aviation result from flights under 2500 km distance operated using narrowbody aircraft [5]. This leads to the following main research question:

“What is the impact of implementing a dual-fuel propulsion system using hydrogen and kerosene (or SAF replacement) on the performance of a narrowbody tube and wing turbofan aircraft?”

The following sub questions are posed to answer the main research question:

1. How is the aircraft design affected by the combination of a hydrogen and kerosene propulsion system and storage?
2. How does the use of hydrogen and kerosene (or SAF replacement) during the mission affect aircraft maximum take-off weight, operational empty weight and fuel weight?
3. What is the effect of the implementation of hydrogen and kerosene dual-fuel capability on the operational performance, including emission effects, of the aircraft?

These research questions assess both the technical and operational implications of a dual-fuel aircraft concept, ultimately contributing to the broader discussion on how aviation can transition towards a more sustainable future.

This report is structured as follows: Chapter 2 describes the findings from literature that support the research objective. Subsequently, Chapter 3 presents the methodology. Chapter 4 present verification and validation methods of the model, after which the results of the model are presented in Chapter 5. Finally, conclusions are drawn and recommendations discussed in Chapter 6.

2

Literature Study

The aviation industry faces a significant challenge to reduce its climate impact to meet targets and goals set by governments and international organisations. Several technological developments exist that can contribute to the decarbonisation of the aviation industry. This chapter will elaborate on these technologies and their challenges and opportunities in Section 2.2. Subsequently, Section 2.3 discusses the opportunities and previous research related to dual-fuel aircraft concepts. First of all, however, Section 2.1 will briefly discuss the need for decarbonisation and the focus on the narrowbody aircraft segment.

2.1. Climate Impact Aviation

Transporting people and goods across the globe and thereby connecting societies and economies globally is one of the most important drivers behind the vast use of aircraft nowadays [5]. However, the impact of this fossil-fuel powered aviation on the climate has become increasingly apparent and a source of worry for many.

It is estimated that aviation is currently responsible for 2.5% of global anthropogenic CO_2 emissions, and with that contributes for 3.5 to 5% to anthropogenic radiative forcing and thereby to global warming [1, 2]. This also includes non-CO_2 effects of aviation emissions on radiative forcing. Although these non-CO_2 effects form a substantial part of the total climate impact of aviation, this study focusses solely on CO_2 emissions.

In general, passenger aircraft have become substantially more efficient over the past decades, and are expected to continue to do so in the future. However, these developments to decarbonise the aviation industry are more than compensated by the growth of the aviation market [5]. To make this more concrete, Rao et al. [1] state that the fuel consumption per revenue passenger-kilometre has been reduced by more than 50% over the past three decades, whereas revenue passenger-kilometres from over this time period increased by around 440%. More specific, in the period between 2013 and 2019, passenger air traffic increased almost four times faster than the improvement in fuel efficiency [8]. It leaves no question to the fact that the aviation industry needs to act fast and rigorously to reduce its climate impact. Therefore, government bodies and organisations take the lead by targeting innovation and emission reduction goals. An example of this is the European Commission's FlightPath 2050 plan, a long-term strategy in order to decarbonise aviation [9].

As can be seen in Figure 2.1, decarbonisation of the aviation industry will mostly rely on novel technologies that drastically reduce emissions [10]. The next section will elaborate on the most relevant technological developments.

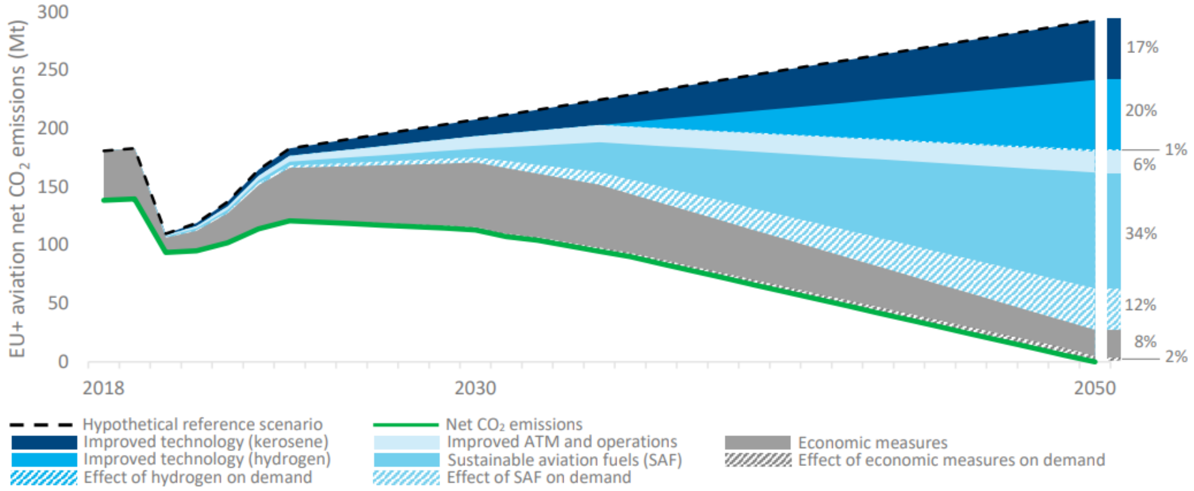

Figure 2.1: Decarbonisation Roadmap for European Aviation. Adapted from [10]

Commercial passenger aviation can be roughly divided into three segments: regional aircraft operating short-range, often domestic, routes, narrowbody aircraft operating short-to-medium range, often continental, routes, and widebody aircraft operating long-range, mainly intercontinental routes. The last two segments account for the vast majority of emissions from commercial aviation [5]. In 2019, narrowbody aircraft like the Boeing 737 and Airbus A320 were operated on more than 60% of all passenger flights, accounting to 43% of the total CO_2 emissions from aviation. In addition, one-third of CO_2 emissions occurred on flights between 1500 and 4000 km, with 50% of cumulative CO_2 emissions from flights under 2500 km [8, 5]. Therefore, this study will focus on medium-range narrowbody aircraft, as decarbonising this aircraft type would be a big step in reducing the overall climate impact of aviation.

There are several technological pathways that can contribute to the reduction of carbon emissions from passenger aircraft. In the next section, the most prominent technologies will be outlined.

2.2. Decarbonisation Technologies for Aviation

There are various options being investigated that could reduce the climate impact of aviation. As could be seen in Figure 2.1, hydrogen and sustainable aviation fuels are expected to be the most prominent technological factors in the decarbonisation of the aviation industry. Therefore, this section will elaborate on these technologies in Section 2.2.2 and Section 2.2.3, respectively. Before that, Section 2.2.1 will briefly touch upon battery-electric propulsion in aviation, as developments are made in this area as well.

2.2.1. Battery-electric propulsion

Battery-electric propulsion is a promising technology to reduce climate impact from aviation. It has several advantages, such that no in-flight emissions are produced. Next to that, it is simple from a system point of view, as the main components are a battery pack and an electric motor to power a propeller. Also, well-to-tank efficiency is highest for battery-electric propulsion compared to (liquid) hydrogen and SAF [4]. Several companies are working on hybrid- or fully-electric aircraft concepts such as Elysian Aircraft [11], Maeve [12] and Heart Aerospace [13]. However, the specific energy of a state-of-the-art battery is approximately 50 times lower than kerosene, meaning the weight of the batteries are a big limiting factor in the achievable range [4, 14]. The Velis Electro is a fully electric two seater aircraft by Pipistrel, but can fly only for 50 minutes [15]. Therefore, unless big technological advancements are made which improve the specific energy of batteries, battery-electric propulsion is not realistic for medium range aircraft like the Boeing 737 or Airbus A320 and will not be considered further in this study [5].

2.2.2. Hydrogen propulsion

Hydrogen is widely regarded as a promising energy carrier for the future of aviation as it enables to fly without in-flight CO_2 emissions and can be a truly zero-carbon solution when produced using renewable resources [1, 5]. Whereas interest in hydrogen-powered aircraft temporarily increased in the previous century during the 1970s oil crisis, the climate impact of aviation has renewed this interest more firmly during this century [5]. Using hydrogen as aircraft fuel poses several advantages, but also some technological and operational challenges. These will be further elaborated on below.

First of all, hydrogen has the advantage that its specific energy, i.e. the amount of energy per unit mass, is 2.8 times higher than kerosene, meaning fuel mass can be reduced when using hydrogen. However, this advantage is opposed by an energy density, i.e. the amount of energy per unit of volume, that is around 4 times lower for hydrogen in liquid form [5, 16]. This means the volume of the stored liquid hydrogen is about 4 times the volume of kerosene for the same energy content. Hydrogen can also be stored in gaseous form. However, the volumetric energy density of this method is even worse [5]. Next to that, storing hydrogen in gaseous form requires heavy compression, resulting in heavy tanks to retain the pressure. In liquid form, hydrogen is stored at cryogenic temperatures of around -253 degrees Celsius (20 Kelvin) [16]. Although this requires increased thermal insulation, this is more mass efficient than gaseous storage of hydrogen. The storage efficiency of hydrogen tanks is expressed using the gravimetric efficiency index η_{tank}, defined in Equation 2.1 [5]. In this equation, W_{H_2} is weight of hydrogen stored in the tank and W_{tank} is the weight of the tank itself.

$$\eta_{tank} = \frac{W_{H_2}}{W_{H_2} + W_{tank}} \tag{2.1}$$

The higher this index, the more fuel can be stored per unit mass of tank weight, and thus the better. The gravimetric efficiency index of the storage system affects the overall performance of the hydrogen aircraft drastically. When comparing estimated energy use of a hydrogen aircraft compared to a kerosene aircraft, Adler and Martins [5] estimate that a tank gravimetric efficiency of 55% is the tipping point beyond which hydrogen aircraft become more efficient with increasing range, independent of whether it concerns a short-, medium- or long-range aircraft. This is reflected in Figure 2.2. Thus, for the aircraft type considered in this study, a tank gravimetric efficiency above 55% is very desirable.

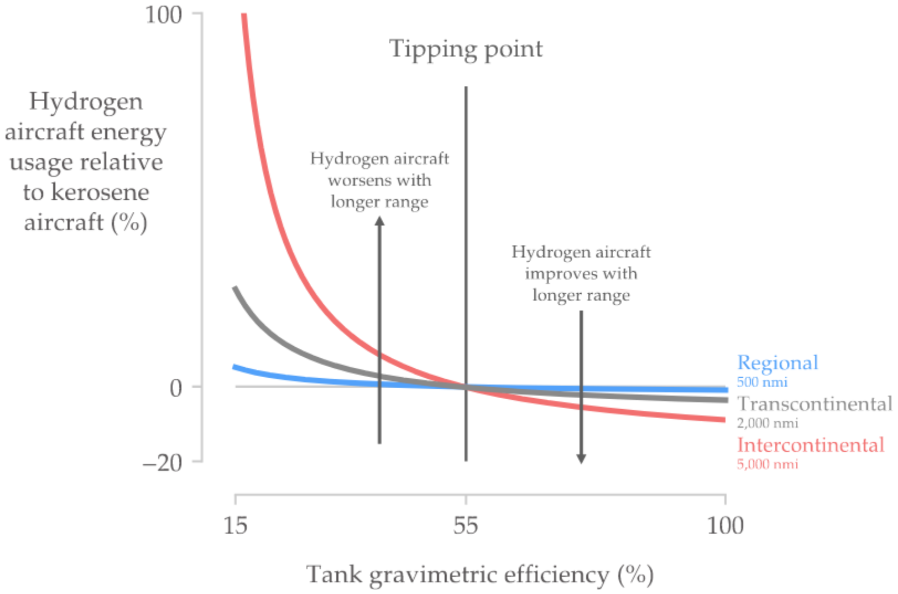

Figure 2.2: Relative energy usage of hydrogen aircraft compared to kerosene aircraft. Beyond 55% gravimetric efficiency, hydrogen aircraft become more energy efficient with increasing range, independent of mission range [5].

Current gravimetric efficiencies for non-integral tanks as used in studies range from 0.5 for a small short-range aircraft to 0.8 for a large long-range blended-wing body, whereas for integral tanks the range is broader, from 0.25 for a small short-range aircraft to almost 0.8 for a very large long range aircraft [17].

Prewitz et al. [18] modelled an A320 with an integral tank with a gravimetric efficiency of around 0.75. Although there are examples of such high tank gravimetric efficiencies, like the liquid hydrogen tank in the Boeing Phantom Eye unmanned vehicle [19] and the composite liquid hydrogen tank prototype by GTL [20], the developments and practical implementation of high-gravimetric efficiency tanks is still uncertain. However, with current insulation technologies, gravimetric efficiencies of 60% seem possible and 70% or above could be achievable in 5 to 10 years [5, 7]. In this study, liquid hydrogen storage will be considered, as it is deemed the only feasible solution to reach sufficient gravimetric efficiency for the use in the aircraft type considered in this study [21, 5, 22].

For liquid hydrogen storage, heat leak into the tank needs to be minimised to reduce boil-off of hydrogen from liquid to gaseous state and thereby increasing the pressure inside the tank. For this, cryogenic tanks need to have a low surface-area-to-volume ratio [5]. This makes hydrogen storage in the wings impossible and necessitates hydrogen tanks to be placed inside the fuselage. In the fuselage, hydrogen tanks can be integrated in the aircraft in either integral or non-integral tanks [5, 23]. In the first case, the tank wall is integrated with the fuselage structure, whereas in the latter case the tank carries only fuel-related loads, which makes non-integral more straightforward to model. Next to that, non-integral tanks are more flexible in their placement inside the aircraft. Therefore, in the conceptual design phase, non-integral tanks are often opted for [5]. However, integral tanks can result in mass savings, especially for larger aircraft [23]. Integral tanks also have the potential for a better surface area-to-volume ratio which helps to reduce heat influx and thereby boil-off [5]. In this conceptual study, non-integral hydrogen tanks will be considered.

Multiple options exist for thermal insulation of the hydrogen tank. Tank insulation can be foam-based, like spray-on foam, or vacuum-based based, possibly combined with multiple layers of reflective foil in the vacuum-gap to form multi-layer insulation. The former option has higher technology readiness level, but the latter option has the potential to reduce tank weight if storage for hours to days is required as boil-off is lower and therefore less fuel is needed initially [5]. This goes to show that cryogenic storage needs a mission specific design approach taking into account the mission and design requirements of that mission. For safety considerations, dormancy time, i.e. the time a hydrogen tank of an aircraft can spend under internal pressure build up due to boil off without fuel extraction or venting is also an important design parameter for passenger air transport on hydrogen [24, 25]. In this study, thermal sizing will focus on dormancy time, rather than the stepwise build-up of pressure inside the hydrogen tank during the mission.

Storing hydrogen in tanks inside the fuselage has implications on the aircraft design. The fuselage length needs to be increased or the passenger accommodation of the aircraft shortened to ensure the tank fits. Fuselage length increases of up to 30% can be expected, which also poses potential challenges from a stability point of view for tube and wing aircraft operating on hydrogen [17].

This also means the wings are now empty, or in other words, ‘dry’ wings, and do not experience load alleviation from kerosene storage and the accompanying structural benefits [5, 26]. Therefore, structural reinforcement is necessary and wing mass will increase, reducing the overall fuel efficiency of the aircraft. In the case of a dual-fuel hydrogen and SAF aircraft concept, the wings are partly filled with fuel, or ‘semi-dry’ wings. Since the fuel volume in the wing is a less determining factor in defining the wing geometry in the case of semi-dry wings, this opens up the possibility to re-evaluate the wing geometry of the reference aircraft designed to fly on kerosene. Increasing the wing aspect ratio with decreasing wing area subsequently reduces the lift induced drag [27]. However, increasing the aspect ratio also requires structural reinforcement due to increased bending moment. Therefore, a trade-off needs to be made between a gain aerodynamic efficiency and resulting reduction in fuel consumption, and the increase in the required energy to overcome the increase in wing weight [28]. This conceptual study will limit to weight estimation of semi-dry wings, but disregards further analysis of aerostructural interactions.

Taking into account a decrease in conventional fuel capacity and the addition of hydrogen as a fuel, there are also possibilities for weight reduction and efficiency increase of hydrogen aircraft compared to kerosene aircraft. Since hydrogen has a higher energy density than kerosene, less fuel is needed to carry the same weight. This can trigger a reverse ‘snowball effect’, as lower fuel weight results in an overall weight decrease, which allows the wing area and engine size to reduce [16].

These aircraft-level mass savings are surrounded by many uncertainties. It depends mostly on the gravimetric efficiency of the hydrogen storage, with a tipping point around 55%, as was mentioned before. Gravimetric efficiencies of 70% could to be achievable in 5 to 10 years, but it is by no means certain [7]. Next to that, hydrogen propulsion will require novel, complex systems, and it is uncertain what the effect of the implementation of these systems will be for the weight.

Just like kerosene, hydrogen is an energy carrier that needs to be converted to release its energy content. This can be done in two ways: through a chemical reaction in a fuel cell generating electricity to drive a propeller or ducted fan, or through combustion in either a reciprocating engine (e.g. in general aviation) or turbofan engines as generally used in larger transport aircraft [5].

Fuel cells are a good option to decarbonise regional turboprop aircraft. ZeroAvia [29], Universal Hydrogen [30] and the German Aerospace Center [31] performed flights partially or fully powered by hydrogen fuel cells, demonstrating its technical feasibility. Next to that, fuel cells are considered to be a viable option as replacement for the kerosene-powered gas turbine auxiliary power unit (APU), which can contribute substantially to aircraft emissions [32]. Limitations of fuel cell powered aircraft lie in the achievable specific power and the velocity and altitude it can be operated at without additional compression. Next to that, other balance of plant components for thermal management and humidification add significantly to the weight of a fuel cell system [5]. Current state of the art turbofans have a higher specific power than fuel cells and are therefore the preferred option for mid-size, Boeing 737 and Airbus A320 type aircraft. In comparison, to power an aircraft of this type, a fuel cell propulsion system would be approximately three times heavier than a turbofan propulsion system [5]. Next to that, hydrogen combustion in a turbofan is the most efficient at the cruise speeds of these type of aircraft [4].

The feasibility of hydrogen combustion in a turbofan was shown by the experimental Tupolev-155 from the Soviet Union in the previous century, running one of its three engines on liquid hydrogen [33]. Next to that, Rolls-Royce has performed a successful test of running its Pearl 700 turbofan engine on hydrogen [34], and Airbus and CFM have been collaborating on preparations for flight testing a turbofan running on hydrogen mounted on an Airbus A380 [35]. Hydrogen combustion in gas turbines is promising, as the fan, compressor, turbine and nacelle work the same way and thus require only minimal design changes compared to kerosene operation. Only the combustion chamber requires significant changes when running on hydrogen compared to kerosene [5].

Because hydrogen contains more energy per unit mass than kerosene, if a conventional kerosene combustor were to be used with hydrogen at the same air-to-fuel ratio as kerosene, the flame temperature would be 100 K higher, resulting in higher NO_x emissions. However, hydrogen has a much wider flammability range than kerosene, which allows it to be operated at a much leaner fuel-to-air mixture [7]. This in turn lowers the combustion temperature and thereby reduces NO_x formation. Lower combustion temperature and thus lower turbine inlet temperature (TIT) improves engine life.

Upon combustion, hydrogen has a higher flame speed and reactivity than kerosene, reducing residence time. Next to that, as hydrogen is injected into the combustor as gas, the diffusion and mixing with air is more efficient compared to kerosene, with is injected as liquid. Both these aspects result in less NO_x formation [7]. The former aspect would allow shortening the combustion chamber [7]. However, in the case of (separate) combustion of both hydrogen and kerosene, this is likely not applicable. For the conceptual work in this study, component level engine modifications are beyond the scope of this research.

The high reactivity of hydrogen with air makes premixing in the combustion chamber difficult and introduces the risk of flashback of hydrogen flames [5]. Non-premixing combustor designs can solve this, like the non-premixing micro-mix combustor design by Dahl and Suttrop [36], or the non-premix direct lean injection system as studied by Marek et al. [37].

The combustion products of hydrogen have a higher specific heat compared to kerosene. This enables engine-level benefits for turbofan engines running on hydrogen [7]. Jagtap et al. [38] did a conceptual design optimisation study for a ultra-high bypass ratio geared turbofan capable of running on both hydrogen and Jet-A and concluded that the total engine weight of an engine optimised for liquid hydrogen reduced with 7.4-17.6% compared to a Jet-A engine. At the conceptual design level considered in this study, specific engine modifications for hydrogen combustion are not considered. Rather, engine sizing is limited to the scaling of existing engines.

If hydrogen is stored as a cryogenic fuel, it requires appropriate conditioning before entering the combustion chamber. It is estimated that the temperature of hydrogen gas needs to be increased to 150 K before entering the combustion chamber. Cryogenic hydrogen poses a great heat sink in this regard, which can be used to cool down engine components with a heat exchanger and improve the overall efficiency this way [7]. In the hydrogen tank, both liquid hydrogen as well as gaseous 'boil-off' is present. This boil-off occurs naturally due to heat flux into the tank. In flight, this boil-off is almost certainly not sufficient for required mass flow rate for the engine. A heat element can be used to add additional heat and create extra boil-off gas [5]. Other fuel system components are fuel pumps, (insulated) lines, valves and regulators and have been described in detail by Brewer et al. [39] and Ebrahimi et al. [25]. This study will not present a detailed design of a hydrogen fuel system, but will include a weight estimation of the hydrogen fuel system similar to Onorato et al. [23].

Over the past years, various studies looked into the application of hydrogen as a fuel in aircraft, varying from retrofits in existing aircraft to more conceptual studies [16, 21, 40, 41, 26, 7, 42, 43, 44]. In most of these studies, payload and/or range was often reduced to accommodate hydrogen storage and propulsion technology.

For example, Cipolla et al. [21] studied retrofitting a box-wing aircraft concept with liquid hydrogen with variable tank lay-outs and could achieve at best 65% range for the same passenger capacity or 40-60% passenger capacity for 10-20% range increase (depending on the number of hydrogen tanks) compared to the reference aircraft. Debney et al. [41] designed a regional, narrowbody and midsize hydrogen aircraft concept based on existing reference aircraft and compare it with a 2030 baseline aircraft on SAF. They show that achieving similar range and payload is achievable in the design point, but that there is virtually no flexibility in terms of extending the range for decreasing payload due to the heavy hydrogen system. Rietdijk and Selier [42] presented a hydrogen fuel cell retrofit study of a DeHavilland Dash 8-300 as part of the 'Aviation in Transition' (Luchtvaart in Transitie) HAPSS project [45]. The reference aircraft has a seating capacity of 50 and a range of 1520 km, but the retrofit manages to only reach 700-900 km (depending on the hold time mission requirement and cruise altitude) with around 30 passengers [46]. Finally, Dutch aircraft company Fokker Next Gen is working on a multi-fuel capable, i.e. the aircraft will be able to fly on liquid hydrogen, SAF and kerosene, that will have a passenger capacity of 120-150 and a range of approximately 2500 km [47]. An aircraft with similar passenger capacity is the Embraer 195-E2, but this aircraft has a range of around 4800 km [48]. These examples show that facilitating hydrogen storage has a big impact on the weight and volume and thereby on the available space for passengers and the achievable range. With the aviation market being very competitive with only a few aircraft OEMs, this is a challenge for the competitiveness of clean aviation solutions and delay their implementation.

Next to the aspect of operational flexibility, operating cost is an important driver in the aviation market, with fuel costs already accounting for around 30% of total operational costs for airlines [1]. Proesmans and Vos [49] estimate that for medium-range aircraft using liquid hydrogen fuel operational costs increase with 42% compared to a cost-optimal kerosene aircraft, whereas using SAF increases operational costs with 14%, thereby reducing climate impact with 98% and 82%, respectively. Therefore, having a dual-fuel capability can provide the capability to find an optimal solution between climate impact reduction and operational costs based on different scenarios.

Finally, the implementation of hydrogen powered aircraft depends not only on the technology readiness of hydrogen propulsion systems, but also on the availability of hydrogen infrastructure. Tiwari et al. [7] present three phases of hydrogen introduction in aviation and the development of infrastructure for this. These phases can be seen in Figure 2.3. It is likely that adaptations for hydrogen operation are first made at large international airports. However, narrowbody aircraft are also expected to be able to operate on smaller airports where this infrastructure development may take longer. This is another aspect that could harm the competitiveness of hydrogen powered aircraft.

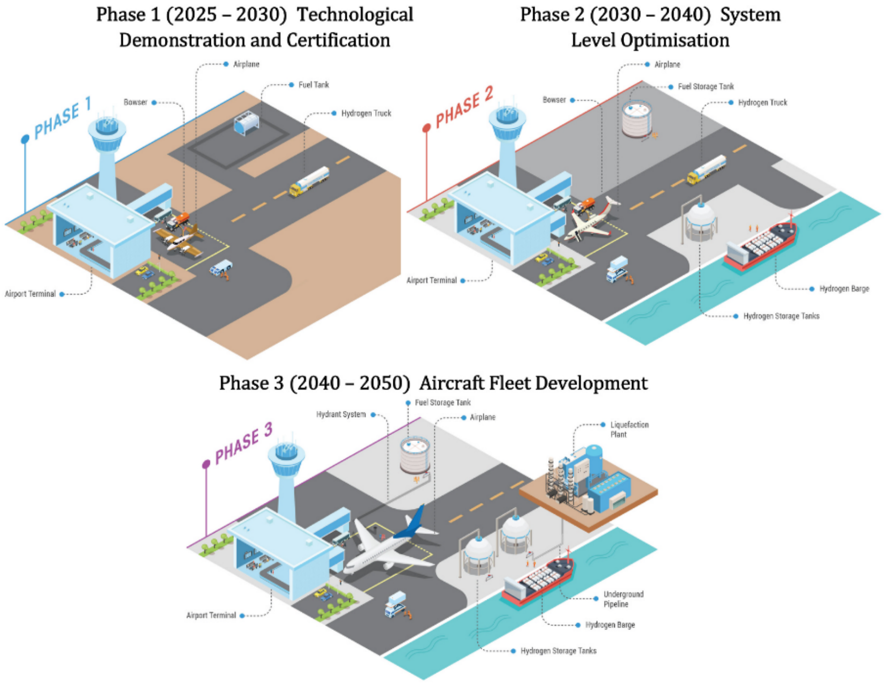

Phase 1 (2025 – 2030) Technological Demonstration and Certification

Phase 2 (2030 – 2040) System Level Optimisation

Phase 3 (2040 – 2050) Aircraft Fleet Development

Figure 2.3: Phases of hydrogen introduction in aviation. Reprinted from: [7]

2.2.3. Propulsion on Sustainable Aviation Fuels

Next to the use of hydrogen as aviation fuel, Sustainable Aviation Fuel (SAF) is also seen as a necessary pathway towards decarbonisation of the aviation industry [3]. SAF is a hydrocarbon fuel like kerosene, but reduces lifecycle carbon emissions compared to fossil derived kerosene. It can be either derived from plants or biological waste in which case it is referred to as biofuel, or synthetically produced from hydrogen and carbon in which case it is referred to as e-SAF [5, 4, 6]. SAF is currently used in small quantities of around 0.1% of kerosene use [6]. Biofuel SAF can reduce the impact of aviation since its feedstock is made up captured atmospheric carbon in its life cycle. It is estimated that biofuel SAF can reduce the impact of flying by 60% in an optimistic scenario [5]. Next to reducing the life cycle carbon emissions, studies have also shown that using SAF can lower soot, sulphur oxides and ultra-fine particles emissions, as well as reduce the climate impact from contrail formation [6]. E-SAF can be a net-zero fuel if renewable electricity is used for electrolysis and carbon capture to generate hydrogen and CO_2, respectively. Producing e-SAF is an energy-intensive process with only 26% of the initial energy arriving at the aircraft in the form of e-SAF fuel [4]. This likely results in a higher fuel cost than liquid hydrogen [4]. However, since current aircraft engines are compatible to fly (partly) on SAF, as well as the existing infrastructure around hydrocarbon-burning aircraft, SAF is a relevant candidate for reducing the climate impact of aviation in the short- and medium-term [6, 4].

In a conventional aircraft, most fuel is stored in the wings. Next to that, a part of the fuel is stored in the centre tank in the fuselage and some fuel is stored in the horizontal tail for trim purposes. For SAF, the storage can be approached the same as for kerosene, but since a dual-fuel aircraft requires less fuel, storage will be focussed on in the wings. This is a great advantage of SAF/kerosene, as the fuel in the wings results in bending relief in flight as well as a gravimetric storage efficiency of almost 100%, since the tank structure is also the lifting surface of the aircraft.

Being a hydrocarbon, combustion of SAF in a conventional turbofan is possible with little to none modifications, given that the composition of SAF is such that it meets the requirements, e.g. on the aromatic content in the fuel in order for the engine to function properly, and additives like anti-freeze [6]. In this study, the scope is limited to SAF as potential replacement of kerosene, but climate impact and cost are not considered.

2.3. Dual-fuel Aircraft Propulsion

Given the aforementioned uncertainties and challenges around hydrogen-powered aviation technology and infrastructure development, using both hydrogen and kerosene (or SAF replacement) in aircraft has potential as interim solution and is a topic of interest in aviation [7]. Smith and Mastorakos [50] performed an energy systems analysis of a large commercial aircraft on liquid hydrogen, constraining fuel capacity to available internal volume, weight and emissions targets. They also considered dual-fuel use of liquid hydrogen in combination with conventional Jet-A and showed that this combination can result in an aircraft that can fly over a greater distance while carrying more passengers than either single-fuel equivalent while staying within the emission and volume constraints, thus combining superior emission performance of liquid hydrogen with superior energy density of Jet-A. Other literature presents different ways of dual-fuel implementation. Various studies looked into the simultaneous use of the fuel types in the same engine, whereas other work researched the simultaneous use in separate engines.

Rao et al. [51] proposed a hybrid engine concept using hydrogen and kerosene in sequential combustion chambers. A model of this engine concept showed that CO_2 emissions could be reduced by around 80%. A subsequent study by Grewe et al. [52] showed that this engine concept has the potential to reduce climate impact by 20% to 25% compared to (future) conventional engine technology. Other studies looked into hydrogen-assisted combustion in a single combustion chamber, like Yelugoti and Wang [53], who experimentally investigated the combustion of premixed jet fuel and hydrogen gas and conclude that CO_2 emission can be reduced this way, but NO_x and unburnt hydrocarbon emissions increased. [54] experimentally tested the simultaneous combustion of diesel and hydrogen inside a small turbojet engine and also found an increase in NO_x and a decrease in CO_2 emissions. Another engine type for which the dual-fuel concept was investigated, was a compression-ignition (CI) reciprocating engine. This was done by Reitmayr et al. [55], who investigated the adaptation of a kerosene engine to a dual-fuel combustion process, initially using CFD simulations, after which experiments were performed. They found that in dual-fuel operation, combustion duration was shorter and exhaust gas temperatures higher than kerosene only operation. Next to that, CO_2 emissions were found to be reduced significantly. In literature, the use of hydrogen alongside kerosene in a turbofan engine was also found in a fuel-cell assisted turbofan. Seyam et al. [56] investigated a high-bypass ratio turbofan engine assisted by a solid-oxide or molten carbonate fuel cell in cruise conditions. They found that the additional weight of the fuel cell reduces the thrust-to-weight ratio, but that emissions are also reduced. In terms of dual-fuel combustion capabilities, several industry initiatives are underway to design an engine that is capable of running on 100% hydrogen and SAF, such as the WET engine by MTU Aero Engines [57] and the CAVENDISH project led by Rolls-Royce [58]. These engine concepts may eventually find their way to novel dual-fuel capable aircraft for which industry initiatives are shown. For example, Fokker Next Gen is designing an aircraft that is capable of flying on hydrogen as well as kerosene or SAF [47]. Similarly, Embraer announced the development of a dual-fuel capable aircraft concept, thereby maximizing operational flexibility [59]. For both the Fokker Next Gen and Embraer concept, it appears that dual-fuel use is not intended during the same mission, but this remains unclear.

Next to simultaneous dual-fuel use in the same engine, another option is to use different fuels simultaneously in different engines. This was employed by Rischmüller et al. [40], who investigated retrofitting a regional turboprop aircraft with a hydrogen tank and replacing one of the turboshaft engines by a fuel cell such that hydrogen and SAF were used in continuous parallel operation. The power allocation between the turboshaft and fuel cell was done through assigning a power split in the design. It was found that allocating the power partly to the fuel cell resulted in a substantial reduction of SAF usage. However, at the cost of a reduction in payload due to increased propulsion system mass and tank volume. The different fuel types can also be used for different parts of the mission. This was experimentally tested in 1957 in the B-57 aircraft, which used jet fuel for take-off and climb, but switched one engine to hydrogen for about 30 minutes during the cruise operation, using a fuel control system compatible of handling the two fuels with a fuel ratio regulator, thereby demonstrating the feasibility of in-flight fuel switching [25].

While emission reduction potential and operational flexibility of dual-fuel propulsion concepts was recognized in literature, research gaps lie in investigating a ‘from scratch’ design procedure for a dual-fuel aircraft concept, thereby exploring the sequential, i.e. different fuel during different parts of the mission, instead of the simultaneous use of hydrogen and kerosene. Next to that, the effect of varying payload and range on the design of a dual-fuel aircraft was identified as research gap from literature.

3

Methodology

In this study, the conceptual design of a dual-fuel aircraft is presented. This chapter presents the methodology followed in this design. First of all, the overall design process is presented. The separate steps and analyses are described in subsequent sections.

3.1. Design Process

To answer the research questions, an aircraft design tool was developed that can be used to generate dual-fuel aircraft concepts. This tool was developed using ParaPy[1], a commercial Python package enhancing parametric design problems like designing an aircraft. ParaPy has the advantage over general object-oriented programming approaches is that it is strong in ensuring dependency tracking of parameters in the design framework, as well as providing a visual representation of the aircraft. This enables fast generation and adaptation of different aircraft concepts. Next to that, ParaPy allows for easy integration with simulation tools, such as for aerodynamic analysis.

3.1.1. Design Flow

The first step in the design process is translating the top-level aircraft requirements (TLARs) to the preliminary sizing of the aircraft. These TLARs specify the number of passengers (PAX), additional cargo, cruise conditions, flight range, and the required reserve range and loiter time for which fuel needs to taken on board. Taking these TLARs, preliminary sizing of the aircraft entails a Class I weight estimation to determine an initial estimate of the operational empty weight (OEW) and fuel weight (FW), divided into hydrogen weight (HW) and kerosene weight (KW), of the aircraft. Next to that, a constraint analysis is done in order to determine the required wing and thrust loading, (W/S) and (T/W), respectively.

The outcomes of preliminary sizing is used to generate the aircraft geometry. This entails sizing the fuselage, wings, empennage and hydrogen tank. With the aircraft geometry, several analyses are performed.

First of all, an aerodynamic analysis is performed to determine the drag polar of the aircraft. Subsequently, this drag polar is used to perform a mission analysis, providing a higher-fidelity estimate of the required fuel weight. With this updated fuel weight and the aircraft geometry, a Class II weight estimation is performed. In this weight estimation, component weights of the aircraft are estimated using semi-empirical relations, resulting in an updated OEW. The component weight estimations can be used to determine the centre of gravity (CG) range of the aircraft, i.e. with and without payload and fuel. This can then be used to update the geometry of the aircraft concept and repeat the design loop. This design loop is visually presented in an N2-chart in Figure 3.1 below.

---

[1] `https://parapy.nl/`

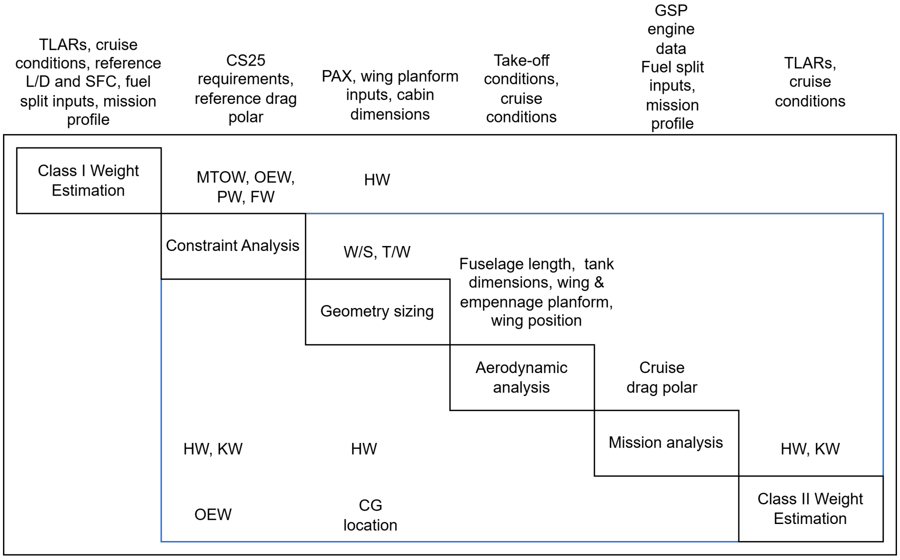

Figure 3.1: N2-chart of the design procedure in this study

The light blue box shows the iterative loop that is followed. The goal of the iterative procedure is to reach the point at which the design is consistent between iterations. This excludes the Class I weight estimation as the fuel fraction method to estimate the fuel weight is only performed during the first iteration. Convergence of the iteration loop is checked by evaluating the relative error of MTOW, OEW and FW between subsequent iterations. A relative error of 0.5% was used. Next to that, when convergence is reached, five extra iterations are performed to check convergence remains consistent.

The different blocks in above chart will be elaborated in subsequent sections.

3.2. Preliminary Sizing

This section will present the preliminary sizing of the aircraft, consisting of Class I weight estimation and constraint analysis.

3.2.1. Class I Weight Estimation

The Class I weight estimation is performed to obtain initial estimates of the operational empty weight (OEW), fuel weight (FW), divided into hydrogen weight (HW) and kerosene weight (KW), and the weight of payload (PW). As it follows from summing these components (Equation 3.1), Class I also provides an initial estimate of the maximum take-off weight (MTOW). These initial weights are needed to make an initial design of the aircraft concept. Their estimation is described below.

$$MTOW = OEW + FW + PW \tag{3.1}$$

Fuel Weight Estimation

To make an initial estimation of the fuel weight required during the mission, fuel weight fractions per flight phase (ff_{phase}) are used. These state what fraction of the aircraft weight is left at the end of a mission phase. In other words, how much fuel is consumed in that mission phase, see Equation 3.5. For short mission phases, empirical values are used, which can be seen below in Table 3.1. For the cruise, loiter and reserve phases, the fuel fraction is determined by rewriting the Breguet equation for range and endurance. For the cruise and reserve phase, Equation 3.2 is used, whereas the loiter phase relies on Equation 3.3. In these equations, V is the velocity the aircraft is flying at, $TSFC$ is the thrust specific fuel consumption, $\frac{L}{D}$ is the lift-to-drag ratio. Since burned fuel is assumed to be the only weight lost during the flight, the fuel fraction can be calculated by rewriting these equations for the fuel fraction. L/D during cruise is assumed to be 16, whereas for reserve and loiter this value is assumed to be reduced by 25% to 12 due to less optimal flying conditions.

The cruise range is computed by subtracting the distance covered during climb from the harmonic range as previously presented. This climb distance is determined with Equation 3.4, in which h_{cruise} is the cruise altitude, RoC the rate of climb and $v_{climb,avg}$ the average climb velocity. The rate of climb is taken to be 762 meter per minute from the database of Janes[2], as this is the value for the Airbus A320neo. The average climb velocity is taken to be 500 km/h, based on Roskam [60]. The thrust specific fuel consumption is approximated based on the CFM LEAP-1A reference engine to be $13.65\ mg/Ns$, a 15% improvement compared to its predecessor, the CFM56, of which $TSFC = 16.06\ mg/Ns$, also based on Janes. For the use of hydrogen, it is assumed that $TSFC$ can be scaled with the ratio of the lower-heating-value (LHV) of hydrogen versus kerosene, which are $120\ MJ/kg$ and $43\ MJ/kg$, respectively [5]. Meaning, $TSFC_{H_2} = (LHV_{kerosene}/LHV_{H_2}) \cdot TSFC_{kerosene}$, as the higher energy content of hydrogen results in a lower required mass flow for the same thrust than kerosene. This way, the fuel fractions for the cruise, reserve and loiter phase can be determined by using either $TSFC_{H_2}$ or $TSFC_{kerosene}$. Like the L/D ratio, $TSFC$ is assumed to be 25% higher (reduced efficiency) for the reserve and loiter phases.

Table 3.1: Empirical fuel fractions, from Roskam [60]

Mission phase	Fuel fraction
Start-up at the gate	0.990
Taxi to the runway	0.990
Take-off	0.995
Climb to cruise altitude	0.980
Descent	0.990
Landing, taxi to gate, shutdown	0.992

$$R = \frac{V}{TSFC}\frac{L}{D}\ln ff \tag{3.2}$$

$$E = \frac{1}{TSFC}\frac{L}{D}\ln ff \tag{3.3}$$

$$R_{climb} = \frac{h_{cruise}}{RoC}v_{climb,avg} \tag{3.4}$$

$$ff_{phase} = \left(\frac{W_{end}}{W_{start}}\right)_{phase} \tag{3.5}$$

Next to the fuel fractions following from Breguet, the empirical fuel fractions from Table 3.1 have to be corrected for the use of hydrogen as well. This is done by scaling with the ratio of LHV as well, which is best explained by an example: say the fuel fraction of a mission phase is 0.990, it means a fraction $1 - 0.990 = 0.01$ of the aircraft weight is lost by burning fuel. Since hydrogen contains more energy per unit mass, this means $0.01 \cdot \frac{43}{120} = 0.0036$ of fuel weight is lost when using hydrogen. This results in a fuel fraction of $1 - 0.0036 = 0.996$ for that mission phase when using hydrogen. Together, the empirical and Breguet fuel fractions for cruise, reserve and loiter, both for hydrogen and kerosene, can be used to determine the Class I estimation of fuel weight.

Fuel split

To incorporate the dual-fuel capability of the aircraft concept in the fuel weight estimation, a fuel split ϕ is applied per mission phase, with ϕ being a fraction between 0 and 1. $\phi = 0$ means the phase is fully flown on kerosene whereas $\phi = 1$ dictates 100% operation on hydrogen during that phase of the mission. The fuel fractions of hydrogen and kerosene that account for the fuel split are calculated using Equation 3.6 and Equation 3.7. In these equations ff_{H_2} and $ff_{kerosene}$ are the fuel fractions for full flight of that phase on hydrogen or kerosene as determined before. This way, if $\phi = 1$ for a phase, meaning that phase is fully flown on hydrogen, $ff_{kerosene,split} = 1$, such that no kerosene weight is computed for that phase in the fuel weight computation below. Similarly, $\phi = 0$ results in $ff_{H_2,split} = 1$. For ϕ between 0 and 1, the correct fuel split corrected fuel fractions will be found with these equations.

$$ff_{H_2,split} = 1 - (\phi \cdot (1 - ff_{H_2})) \tag{3.6}$$

$$ff_{kerosene,split} = 1 - ((1 - \phi) \cdot (1 - ff_{kerosene})) \tag{3.7}$$

---

[2] `https://customer.janes.com/`

For single fuel aircraft, the fuel weight can be calculated with Equation 3.8, in which $\Pi_{ff,total}$ is the product of fuel fractions of the mission.

$$FW = (1 - \Pi_{ff,total}) \cdot MTOW \tag{3.8}$$

For a dual-fuel aircraft concept, this relation still holds to compute the total fuel weight by taking $\Pi_{ff,total} = \Pi_{ff,H_2} \cdot \Pi_{ff,kerosene}$, in which Π_{ff,H_2} and $\Pi_{ff,kerosene}$ are the products of fuel split corrected fuel fractions of hydrogen and kerosene, respectively. However, to determine the separate contributions of hydrogen weight (HW) and kerosene weight (KW) it does not hold to apply the product of fuel fraction in the same way. Expressed mathematically:

$$FW = (1 - \Pi_{ff,total}) \cdot MTOW \neq (1 - \Pi_{ff,H_2}) \cdot MTOW + (1 - \Pi_{ff,kerosene}) \cdot MTOW$$

Therefore, the total hydrogen and kerosene weight is determined per phase, using Equation 3.9 and Equation 3.10, respectively. In these equations, ff_{phase,H_2} and $ff_{phase,kerosene}$ are the respective fuel split corrected fuel fractions for hydrogen and kerosene per phase that where determined previously. $W_{phase,init}$ is the weight at the start of that phase, computed by subtracting HW_{phase} and KW_{phase} from $W_{phase,init}$ from the previous phase, which will be MTOW for the first phase. The total hydrogen and kerosene weight is obtained by summing the contributions per phase.

$$HW_{phase} = (1 - ff_{phase,H_2}) \cdot W_{phase,init} \tag{3.9}$$

$$KW_{phase} = (1 - ff_{phase,kerosene}) \cdot W_{phase,init} \tag{3.10}$$

3.2.2. Payload Weight Estimation

The payload taken on board the aircraft is computed from the relevant TLARs as presented before with Equation 3.11, in which the number of passengers (PAX) is multiplied by the sum of average passenger weight and baggage per passenger, taken to be 80 kg and 15 kg, respectively [60]. W_{cargo} is additional cargo weight, taken as 750 kg. For 150 passengers, this results in a payload weight of 15000 kg.

$$PW = PAX \cdot (W_{passenger} + W_{baggage}) + W_{cargo} \tag{3.11}$$

3.2.3. Operational Empty Weight Estimation

The operational empty weight of the aircraft is the combination of the empty weight (EW) of the aircraft and the crew weight. The latter of which is computed by treating crew members, in this case 5 (2 pilots and 3 flight attendants) as passengers with baggage. EW is estimated using an empirical relation between MTOW and EW from Roskam [60]. As the dual-fuel aircraft concept has the addition of a hydrogen fuel system and tank on board, weight estimates of these components are added to the empty weight. The weight of the hydrogen tank is computed by rewriting the relation for tank gravimetric efficiency (Equation 2.1) for tank weight, and using the obtained hydrogen fuel weight as described above. The tank gravimetric efficiency of the hydrogen tank is taken to be 0.4, a conservative value compared to the average gravimetric efficiency of studies on foam insulated tanks by Huete et al. [61], as compiled by Jagtap et al. [17].

The weight of the hydrogen fuel system is estimated using the method from Onorato et al. [23], in which the semi-empirical relation for fuel system weight from Torenbeek [62], Equation 3.12 below, is corrected for the use of hydrogen by dividing with a factor k_{fs}. In this equation, N_{eng} is the number of engines, N_{ft} is the number of fuel tanks and V_{ft} is the fuel volume in litres. The correction factor is obtained by applying Equation 3.12 to the fuel system for a tube and wing aircraft powered by liquid hydrogen turbofans as described by Brewer [63] and comparing to the value reported by him. This results in $k_{fs} = 0.5$, in other words the hydrogen fuel system as found by Brewer is twice as heavy than a kerosene fuel system to what is found when applying the Torenbeek relation for fuel system.

$$W_{fs} = \frac{1}{k_{fs}} \cdot 36.3 \cdot (N_{eng} + N_{ft} - 1) + 4.366 \cdot N_{ft}^{0.5} \cdot V_{ft}^{0.333} \tag{3.12}$$

The relation between EW and MTOW (in pounds) from Roskam [60] can be seen in Equation 3.13. Converting EW back from pounds to kilograms and adding the crew weight gives OEW.

$$EW = 10^{(\log_{10} MTOW - 0.0833)/1.0383} \tag{3.13}$$

An initial guess for MTOW is used to compute the fuel weight and OEW. Adding the payload gives an updated value for MTOW. An iterative procedure is used to convergence to consistent values of OEW, FW and MTOW.

3.2.4. Constraint Analysis

With the Class I weight estimation, the constraint analysis can be performed. This analysis is done to determine the required wing and thrust loading, W/S and T/W respectively, for the aircraft concept. The constraints that the aircraft needs to comply to are Certification Specification 25 requirements from the European Union Aviation Safety Agency (EASA) [64] and from these the following constraints are taken into account:

- Take-off field length
- Landing field length
- Climb gradient in multiple scenarios
- Cruise velocity
- Maximum wing span

3.2.5. Take-off field length

Instead of specifying a certain runway length the aircraft needs to be able to take off from, the required T/W at take-off is determined by using the Take-Off Parameter (TOP) method as presented by Roskam [60]. This parameter is computed by Equation 3.14 and evaluated for existing reference aircraft with similar payload and range specifications (A320-200, A321-200, B737-300, B737-400). Data is taken from Jenkinson et al. [65] for The average of these TOP-values is then used in Equation 3.14 together with the design wing loading to determine T/W at take-off. The take-off lift coefficient $C_{L_{TO}}$ is computed by dividing the maximum take-off lift by 1.21 [60]. The average TOP that will be used is $9421\ N/m^2$, corresponding to a take-off field length of approximately 2250 meter according to the relation in Roskam [60].

$$TOP = \frac{1}{C_{L_{TO}}} \frac{W}{S} \frac{W}{T} \tag{3.14}$$

3.2.6. Landing field length

The requirement on the landing field length is used to determine the approach velocity of the aircraft using Equation 3.15. A landing field length of 1440 meter, equal to the A320-200, is assumed. From the approach velocity V_A, the stall speed can be estimated at CS25 regulations stipulate that the approach speed is 23% higher than the stall speed. The wing loading to meet the stall speed requirement can be calculated based on the assumed maximum lift coefficient in landing configuration of 2.8 [60].

$$s_{LF} = 0.3 \cdot V_A^2 \tag{3.15}$$

3.2.7. Climb Gradients

Several climb gradient requirements are adhered to in sizing the thrust loading of the aircraft. These are presented below:

- CS25.111c: OEI Take-off at 1.2% climb gradient, take-off flaps, gear up, $V = 1.2 \cdot V_{stall}$, take-off thrust
- CS25.121a: OEI Lift-off at 0% climb gradient, take-off flaps, gear down, $V = 1.1 \cdot V_{stall}$, $V = 1.2 \cdot V_{stall}$, take-ff thrust
- CS25.121b: OEI Take-off at 2.4% climb gradient, take-off flaps, gear up, $V = 1.2 \cdot V_{stall}$, take-off thrust

- CS25.121c: OEI Take-off at 1.2% climb gradient, take-off flaps up (clean), gear up, $V = 1.25 \cdot V_{stall}$, maximum continuous thrust
- CS25.119: AEO landing at 3.2% climb gradient, landing flaps down, gear down, $V = 1.3 \cdot V_{stall}$, take-off thrust
- CS25.121d: OEI balked landing at 2.1% climb gradient, approach flaps down, gear down, $V = 1.5 \cdot V_{stall,approach}$, take-off thrust

The required thrust loading for each condition is calculated with Equation 3.16, in which CGR is the climb gradient factor. This equation requires an approximate lift-to-drag ratio. This is calculated using Equation 3.17 and Equation 3.18, following the drag estimation method described in Roskam [60] to apply drag contributions of flaps and landing gear. The lift coefficient is found by correcting the maximum lift coefficient (obtained from Roskam [60]) for the velocity requirement at every climb condition.

$$\frac{T}{W} = \frac{1}{L/D} + CGR \tag{3.16}$$

$$C_D = C_{D_0} + \frac{C_L^2}{\pi A e} \tag{3.17}$$

$$C_{D_0} = \frac{f}{S} \tag{3.18}$$

3.2.8. Cruise Velocity

The required thrust and wing loading at cruise conditions is estimated with Equation 3.19, which relates these two parameters. The zero lift drag coefficient from the climb gradient analysis is used again, but $\Delta C_{D_0} = 0.00035$ is added to account for compressibility effects at cruise conditions [60]. Also, the thrust and wing loading are corrected for the aircraft weight at start of cruise, for which the fuel fractions from Section 3.2.1 are used. The thrust at cruise altitude needs to be converted to the thrust at take-off assuming that cruise thrust is 23% of take-off thrust [60].

$$\frac{T}{W} = C_{D_0} q \frac{S}{W} + \frac{W}{S} \frac{1}{\pi q A e} \tag{3.19}$$

In the above equation, the aspect ratio A of the A320-200 is used. The Oswald factor in clean conditions is assumed to be 0.8.

3.2.9. Maximum Wing Span

The maximum wing span condition limits the feasible design space of the wing loading on the low side. This limit is determined by calculating the maximum wing area using Equation 3.20 at the maximum wing span and aspect ratio of a reference aircraft. The maximum wing span is based on the span limit of the ICAO aircraft category of the reference aircraft of this study, the Airbus A320. This span limit is 36 meters[3].

$$S_{max} = \frac{b_{max}^2}{A} \tag{3.20}$$

Combining all wing and thrust loading constraints, the design point is found at the maximum possible wing loading and minimum required thrust loading. Figure 3.2 shows an example constraint diagram of a dual-fuel aircraft, for which the mission is flown on hydrogen except the reserve, loiter and landing phases.

---

[3] `https://skybrary.aero/articles/icao-aerodrome-reference-code`

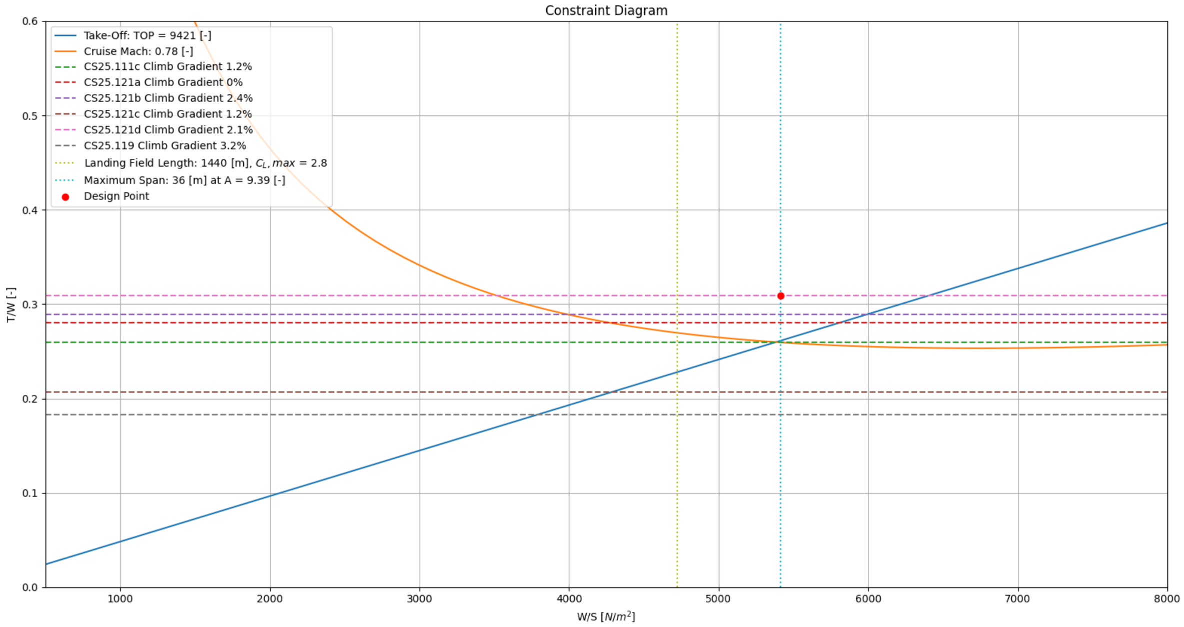

Figure 3.2: Example constraint diagram of a dual-fuel aircraft

3.3. Aircraft Geometric Sizing

When the preliminary sizing is done, the geometric sizing of the aircraft can be initiated. This section describes sizing of the fuselage, main wing, empennage, hydrogen tank and engine sizing in subsequent sections.

3.3.1. Fuselage Sizing

The fuselage sizing comprises the determination of the fuselage length and width. The fuselage length is divided into three sections for: the nose cone, the centre section and the tailcone. The nose cone (l_{nc}) is assumed to have a constant length of 4 meters, based on an estimated flight deck length of 3.3 meters for three cockpit seats [66], including some margins.. The centre section length of the fuselage contains the passenger accommodation as well as the hydrogen tank behind passenger compartment. The fuselage width is sized based on the space needed by passenger accommodation. Therefore, the hydrogen tank is sized based on this width, which will be elaborated upon in Section 3.4. In this study, a circular fuselage shape is assumed.

This passenger accommodation is sized based on the amount of passengers, galleys, lavatories and aisles. As this study focusses on a narrowbody short-to-medium range aircraft, a 3-3 seat arrangement with one aisle is used. In terms of seating arrangement, a single-class economy seating configuration is assumed. For 150 passengers, 2 type I exits (regular doors) and 2 type III exits (over the wing emergency exits) are required [67]. Next to that, 2 lavatories and 2 galleys are included length-wise (forward and aft). Compiling the components, the length of the passenger accommodation (l_{pax}) is determined by multiplying the number of seat rows by the seat pitch and adding twice the width, length-wise with respect to the fuselage, of a lavatory, galley, type I and type III exit. Table 3.2 shows the dimensions the components that determine the length of the passenger accommodation. The number of seat rows determined from the number of seats abreast and required passengers. For 150 passengers and 6 seats abreast that results in 25 rows.

The cabin width of the fuselage is determined using Equation 3.21, in which n_{SA} and n_{aisle} are the respective number of seats breast and the number of aisle. w_s and w_{aisle} are the respective seat and aisle widths, and $s_{clearance}$ is the clearance between the armrest of the outer seat and the cabin wall. The outer fuselage diameter, so including the structural depth of the fuselage, is subsequently determined with Equation 3.22. Both equations are based on Vos et al. [68]. Table 3.2 shows the dimensions of the fuselage components used to size the cabin.

$$w_{cabin} = n_{SA} \cdot w_s + (n_{SA} + n_{aisle} + 1) \cdot w_{armrest} + n_{aisle} \cdot w_{aisle} + 2 \cdot s_{clearance} \quad (3.21)$$

$$w_f = 1.045 \cdot w_{cabin} + 0.084 \quad (3.22)$$

The length of the hydrogen tank section (l_{H2tank}) of the centre section of the fuselage is based on the required length of the tank. This is based on the available diameter and required hydrogen fuel to be stored in the tank. This will be further elaborated upon in Section 3.4. In between the hydrogen passenger accommodation and the start of the tank, an arbitrary margin of 5% of the hydrogen tank length is included. The tank section is not comprised of the whole tank length. Rather, it is assumed that the aft cap of the hydrogen tank runs into the tail cone of the fuselage, like done by Onorato et al. [23]. This was decided such that the fuselage length is not increased more than necessary, but still keep the remaining space in the tail cone to accommodate the auxiliary power unit (APU) and empennage structure like in a kerosene-powered aircraft. Also, other systems necessary for hydrogen-powered flight might be positioned there, but looking into this was beyond the scope of this study.
Finally, the length of the fuselage tail cone (l_{tc}) is determined from the fuselage width through Equation 3.23, in which k_{tc} is a factor relating the length of the fuselage tailcone to the fuselage diameter. k_{tc} is taken to be 2.6, the lower bound of existing jet transport ratios as presented by Roskam [69]. Figure 3.3 shows the entire fuselage with lengthwise section division.

$$l_{tc} = d_f \cdot k_{tc} \quad (3.23)$$

Table 3.2: Fuselage component dimensions

Fuselage component	Value	Based on
Seat pitch [m]	0.81	De Jonge [66]
Seat width [m]	0.48	De Jonge [66]
Armrest width [m]	0.057	Roskam [67]
Seat clearance [m]	0.05	De Jonge [66]
Aisle width [m]	0.48	A320 aisle width, from Roskam [67]
Type I exit width [m]	0.61	Minimum exit width required by CS-25, from De Jonge [66]
Type III exit width [m]	0.51	Minimum exit width required by CS-25, from De Jonge [66]
Galley width [m]	0.76	De Jonge [66]
Lavatory width [m]	0.76	De Jonge [66]

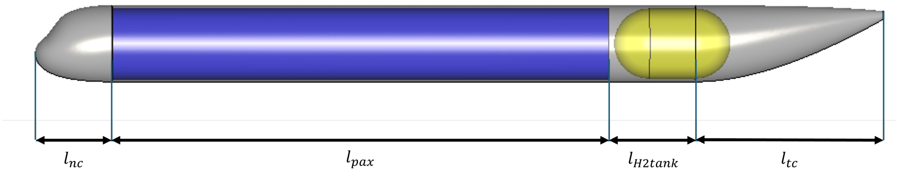

Figure 3.3: Fuselage length sections

3.3.2. Main Wing Sizing

The main wing of the aircraft concept is assumed to be a simple trapezoidal wing without winglets. The determination of the main parameters is presented below.

The quarter-chord sweep angle is determined with Equation 3.24 [70], in which $M^\dagger$ is a Mach number including a technology factor for supercritical airfoils and is taken to be 0.935, and M_{DD} is the drag divergence Mach number, which is determined with Equation 3.25. This results in $\Lambda_{c/4} \approx 30°$.

$$cos(\Lambda_{c/4}) = 0.75 \frac{M^\dagger}{M_{DD}} \quad (3.24) \qquad M_{DD} = M_{cruise} + 0.03 \quad (3.25)$$

Subsequently, the taper ratio λ is determined with Equation 3.26 [70].

$$\lambda = 0.2 \cdot (2 - \Lambda_{c/4}) \tag{3.26}$$

The wing area is a result from the wing loading and MTOW that was determined in the constraint analysis described in Section 3.2.4. The wing span b is set at 36 meters to stay within the ICAO category C limit of the reference aircraft, as was also mentioned in the constraint analysis. From the wing area, the aspect ratio of the wing can be determined using Equation 3.27. The root and tip chord of the wing are determined with Equation 3.28 and Equation 3.29, respectively [70]. Finally, a constant dihedral angle Γ of 5 degrees was chosen [71].

$$A = \frac{b^2}{S} \tag{3.27}$$

$$c_r = \frac{2S}{(1+\lambda)b} \tag{3.28}$$

$$c_t = \lambda\, c_r \tag{3.29}$$

From the wing geometry, the length $\bar{c}$ and spanwise position $\bar{Y}$ of the mean aerodynamic chord (MAC) can be determined with respectively Equations 3.30 and 3.31 [71].

$$\bar{c} = \frac{2}{3}\frac{c_r(1+\lambda+\lambda^2)}{(1+\lambda)} \tag{3.30}$$

$$\bar{Y} = \frac{b}{6}\frac{(1+2\lambda)}{(1+\lambda)} \tag{3.31}$$

The wing is initially positioned halfway along the fuselage. However, this value is updated in the design loop after subsequent Class II component weight estimation and determination of the aircraft centre of gravity, which are described later on.

Airfoils

For the aircraft concept, different root and tip airfoils were chosen. It was found by Obert [72] that the A320-200 has a thickness-to-chord t/c ratio of 0.15 at the root, and 0.11 at the top. Therefore, the root airfoil was chosen to be the NACA63-415 airfoil, which has a 15% t/c at the root. For the tip airfoil, the supercritical Whitcomb airfoil was chosen, with a t/c of 11%.

Regarding the overall wing design, it has to be noted that wing incidence, as well as wing twist from root to tip were not investigated in this study.

3.3.3. Empennage Sizing

The empennage comprises of the horizontal and vertical tailplanes. Their sizing is done based on wing and fuselage dimensions on one hand, but also assumed values on the other hand. The sizing process will be outlined below.

The area of the horizontal and vertical tail is calculated with Equation 3.32 and Equation 3.33, respectively [71]. In these equations, V_h and V_v are the respective tail volume coefficients for the horizontal and vertical tailplane. This is a non-dimensional property of a tailplane surface. They are assumed to be 1.00 for the horizontal tailplane and 0.09 for the vertical tailplane, based on estimates by Raymer [71]. Furthermore, $\bar{c}$ is the mean aerodynamic chord of the wing, determined with Equation 3.30, and l_h and l_v are the respective tail arms for the horizontal and vertical tailplanes. The tail arm is the distance between the aerodynamic centre (assumed at $\bar{c}/4$) of the wing and horizontal/vertical tailplane. For initial sizing, it is assumed to be 40% of the fuselage length for both the horizontal and vertical tailplane, but the tail arms are updated in the design loop when the wing position, and with that the aerodynamic centre, is updated.

$$S_h = \frac{V_h\, \bar{c}\, S}{l_h} \tag{3.32}$$

$$S_v = \frac{V_v\, \bar{c}\, S}{l_v} \tag{3.33}$$

To determine the other planform parameters of the horizontal and vertical tailplane, the following assumptions are made, based on Raymer [71]:

- $A_{HT} = 4$
- $A_{VT} = 2$
- $\lambda_{HT} = 0.4$
- $\lambda_{VT} = 0.3$

Using this, the span of the horizontal and vertical tailplanes are computed with Equation 3.34, whereas the root and tip chord are obtained with Equation 3.28 and Equation 3.29, respectively. Finally, the quarter-chord sweep angles of the horizontal and vertical tailplanes are both set as $35°$, as they are usually $5°$ higher than the quarter-chord sweep angle of the main wing [71]. This is done such that the empennage surfaces are affected by drag rise in the high transonic regime later than the main wing, and thereby ensuring controllability.

$$b = \sqrt{A \cdot S} \tag{3.34}$$

Empennage airfoils
Similar to Tran [73], the following root and tip airfoils are chosen for the empennage:

- Horizontal tailplane root airfoil: NACA 0012
- Horizontal tailplane root airfoil: NACA 0009
- Vertical tailplane root airfoil: NACA 0012
- Vertical tailplane root airfoil: NACA 0010

Empennage positioning
The empennage is positioned such that there is an offset of quarter-chord of the root chord of the vertical tailplane between the trailing edge of the root chord of the vertical tailplane and the end of the fuselage.

3.4. Hydrogen Tank Sizing

An important part of the dual-fuel aircraft conceptual design is the hydrogen tank, as it largely affects the length increase of the fuselage and the weight of the aircraft. In Class I weight estimation (Section 3.2.1, the tank mass was taken into account through an assumed value for gravimetric efficiency. However, more detail is required to be included in the design sequence of the aircraft concept in order to catch the impact of this tank. This will be presented in this section.

The tank sizing will be done with an outside-in approach, meaning that the fuselage diameter as determined in Section 3.3.1 will be used to fit the hydrogen tank in. This means that the length of the tank will be the main parameter to alter to make sure the required amount of hydrogen fuel fits. The tank in this study is modelled as a cylindrical tank with hemispherical caps and will be non-integral tank, such that mounting points need to be accommodated for as well. Next to that, the tank wall will be modelled as an inner structural shell from Al2219-T851 aluminium with a polystyrene foam insulation layer around the shell. Therefore, the sizing process of this tank is separated into structural sizing of the tank wall and thermal sizing of the insulation layer around the tank. This approach is similar to the work by Di Summa [74], following the methods by Onorato et al. [23] for the structural sizing and the work by Tarbah [75] for the thermal sizing. A schematic of the longitudinal section of the tank model can be seen in Figure 3.4 below.

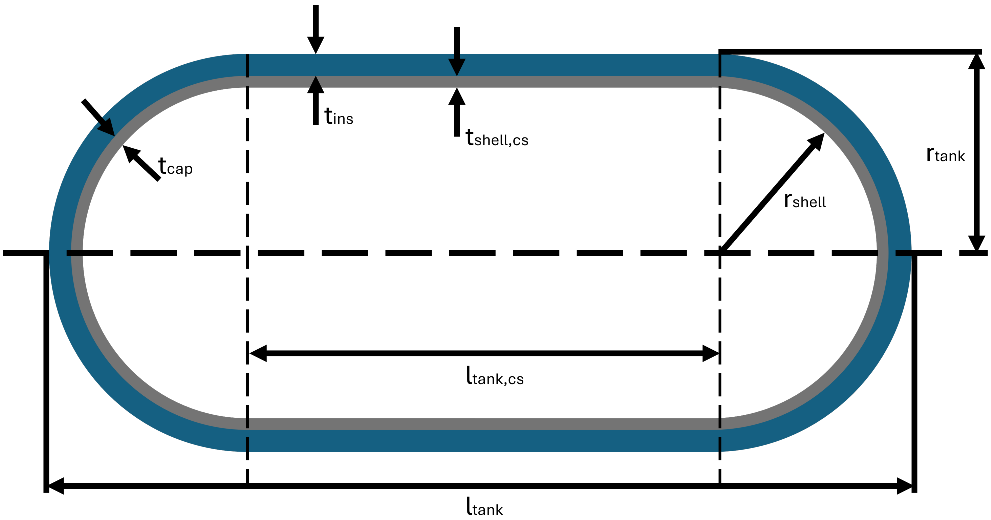

Figure 3.4: Schematic of the longitudinal section of the hydrogen tank

3.4.1. Structural sizing

The structural shell will be sized to resist the pressure loads on the shell. The material properties used in this subsection are taken from Brewer [63] and also used by Onorato et al. [23]. The thickness of the centre section of the shell will be determined with Barlow's formula, Equation 3.35. In this equation, P_{vent} is the vent pressure, the maximum allowable pressure inside the tank due to boil-off of hydrogen after which boil-off gas needs to be vented out. Similar to Di Summa [74], a vent pressure of 4.0 bar is chosen, which is higher than the 2.5 bar as used by Onorato et al. [23], such that a more conservative estimate of the shell thickness is made. P_{out} is the pressure outside the tank, for which the ambient pressure at cruise altitude is used, following from the assumption that the tank will be placed outside the pressurized area of the cabin. e_w is the weld efficiency, taken to be 0.8 [63]. r_{shell} is the internal radius of the structural shell. As the total tank radius is a combination of the shell radius and insulation thickness, but the latter depends on the former, a few iterations are required to ensure the tank to fit in the fuselage. An initial guess for r_{shell} is taken to be half of an initial guess of the internal diameter of the tank. This latter initial guess is taken as 90% of the cabin diameter as determined in Section 3.3.1. σ is the design stress of the shell material. To account for fatigue limits from repeated use of the tank, the Goodman relation is applied twice. First, it is applied to obtain the fatigue limit for reverse loading $\sigma_{a,-1}$ in Equation 3.36, in which $\sigma_{a,R_1} = 172\ MPa$ and $\sigma_b = 234\ MPa$ are the design and ultimate stress of the material, respectively, and $R_1 = 0.43\ [-]$ is the ratio of minimum to maximum stress occurring at cryogenic temperature after 40,000 loading cycles. To obtain the design stress of the shell the Goodman relation is applied again in Equation 3.4.1 using the fatigue limit $\sigma_{a,-1}$ and a stress ratio R_2 that is determined from the minimum (at sea level) and maximum (at cruise altitude) relative to the vent pressure.

For the hemispherical caps the thickness, t_{cap}, is half of the centre section thickness as the circumferential stresses are halved [23].

The length of the centre section of the tank is determined from the required hydrogen volume in the tank, which is determined by dividing the hydrogen mass, initially from Class I, but afterwards from the mission analysis, by the density of liquid hydrogen ($70.85\ m^3$ from Brewer [63]). To this volume, allowances are added: 2% for ullage, i.e. the non-fillable part of the tank, 0.9% for tank contraction-expansion and 0.6% for internal equipment [63]. The length of the centre section $l_{tank,cs}$ is determined with Equation 3.38, in which $V_{tank,allowance}$ is the hydrogen volume including the volume allowances mentioned above. V_{caps} is the volume that fits inside the two hemispherical caps, determined from the volume of a sphere (Equation 3.4.1). In these equations, r_{shell} is again the radius of the internal shell. In case the required hydrogen volume including allowance is lower than what fits in the hemispherical caps, the tank will be spherical ($l_{tank,cs} = 0$).

$$t_{shell_{cs}} = \frac{(P_{vent} - P_{out}) \cdot r_{shell}}{\sigma \cdot e_w} \tag{3.35}$$

$$\sigma_{a,-1} = \frac{\sigma_{a,R_1}}{1 - \frac{\sigma_{a,R_1} \cdot 0.5 \cdot (1+R_1)}{\sigma_b}} \tag{3.36}$$

$$\sigma = \frac{\sigma_{a,-1}}{1 + \frac{\sigma_{a,-1} \cdot 0.5 \cdot (1+R_2)}{\sigma_b}} \tag{3.37}$$

$$l_{tank,cs} = \frac{V_{tank,allowance} - V_{caps}}{\pi \ r_{shell}^2} \tag{3.38}$$

$$V_{caps} = \frac{4}{3} \ \pi \ r_{shell}^3 \tag{3.39}$$

3.4.2. Thermal sizing

The thermal sizing of the polystyrene foam insulation layer will be done based on a boil-off rate requirement. This boil-off rate is based on the work of Huete & Pilidis [24] and corresponds to a dormancy time of 12 hours (overnight parking). The dormancy time is the time it takes for the pressure in the tank to reach the vent pressure when not in use. In other words, it is required that a filled tank can be left overnight without the need to vent hydrogen gas, which could be potentially dangerous. Based on the boil-off rate, the allowable heat influx into the tank can be determined, which has to be resisted by the insulation layer. This thermal resistance is modelled as multiple layers, each with its own thermal resistant. These layers are schematically shown in Figure 3.5. The ambient temperature T_{amb} and the hydrogen temperature T_{H_2} are known: $288.15\ K$ and $20\ K$, respectively.

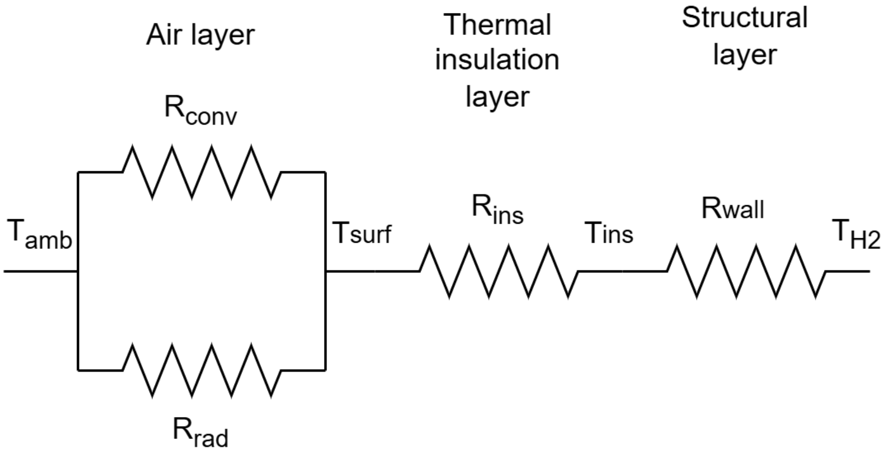

Figure 3.5: Thermal resistance layers, adapted from [75].

The boil-off mass flow rate in kg/s can be determined with Equation 3.40. In this equation $k_{boiloff}$ is a scaling factor that is used to match the ratio of boil-off to tank volume as used by Tarbah [75]. Additionally, the scaling factor is tuned such that the gravimetric efficiency of the tank model aligns sufficiently with what is found by Huete & Pilidis [24] for a dormancy time of 12 hours, which will be further elaborated on in Section 4.2.1. Considering this, $k_{boiloff} = 1.12 \cdot 10^{-4}$ is used. Furthermore, V_{tank} is the required tank volume. With the boil-off mass flow rate, the heat flux limit in the tank can be determined with Equation 3.41, in which ΔH_e is the heat of evaporation of liquid hydrogen at storage conditions and equals $4.47 \cdot 10^5\ J/kg$.

$$\dot{m}_{boiloff} = k_{boiloff} \cdot V_{H2} \tag{3.40}$$

$$\dot{Q} = \dot{m}_{boiloff} \cdot \Delta H_e \tag{3.41}$$

With the heat flow determined, the sizing of the insulation layer can be done by determining the heat resistance of the layers shown in Figure 3.5. The first layer is the air around the tank, through which heat is both radiated and conducted. The radiation heat is computed with Equation 3.42, in which σ_{bolt} is the Stefan-Boltzmann constant and equals $5.67 \cdot 10^{-8}\ W/(m^2 \cdot K^4)$, e_0 is the emissivity of the insulation layer and equals 0.9 [74], and T_{surf} and T_{amb} are the temperatures of the outer surface and ambient air at sea-level.

$$h_{rad} = \sigma_{bolt}\ e_0\ \left(T_{surf}^2 + T_{amb}^2\right)\left(T_{surf} + T_{amb}\right) \tag{3.42}$$

The heat transfer through the air layer from convection is calculated with Equation 3.43, in which k_a is the thermal conductivity or air at ambient temperature ($0.0255\ W/m/K$), D_{tank} is the tank diameter, and Nu is the Nusselt number of the tank. This latter parameter is calculated as a weighted average of the Nusselt number of a sphere (Equation 3.45) and a cylinder (Equation 3.4.2), as can be seen in Equation 3.4.2.

$$h_{conv} = \frac{k_a \cdot Nu}{D_{tank}} \quad (3.43) \qquad Nu = \frac{L_{cyl} \cdot Nu_{cyl} + D_{tank} \cdot Nu_{sph}}{L_{cyl} + D_{tank}} \quad (3.44)$$

$$Nu_{sphere} = 2 + \frac{0.589 Ra^{1/4}}{\left(1 + \left(\frac{0.469}{Pr}\right)^{9/16}\right)^{4/9}} \quad (3.45) \qquad Nu_{cylinder} = \left(0.6 + \frac{0.387 Ra^{1/6}}{\left(1 + \left(\frac{0.559}{Pr}\right)^{9/16}\right)^{8/26}}\right)^2 \quad (3.46)$$

The Rayleigh number (Ra) and the Prandtl number (Pr) that are used in these equations are calculated with Equation 3.47 and Equation 3.4.2, respectively. In these equation, g is the gravitational acceleration, β is the volumetric thermal expansion coefficient (Equation 3.49), α_a is the diffusivity of air (Equation 3.50), and ν_a is the kinematic viscosity of ambient air (Equation 3.51).

$$Ra = \frac{g \cdot \beta\ \cdot (T_{amb} - T_{surf})\, D_{tank}^3}{\nu_a \cdot \alpha_a} \quad (3.47) \qquad Pr = \frac{\nu_a}{\alpha_a} \quad (3.48)$$

$$\beta = \frac{1}{T_{amb}} \quad (3.49)$$

$$\alpha_a = -3.119 \cdot 10^{-6} + 3.541 \cdot 10^{-8}\, T_{amb} + 1.679 \cdot 10^{-10}\, T_{amb}^2 \quad (3.50)$$

$$\nu_a = -2.079 \cdot 10^{-6} + 2.777 \cdot 10^{-8}\, T_{amb} + 1.077 \cdot 10^{-10}\, T_{amb}^2 \quad (3.51)$$

With the determined heat transfer coefficients for conduction and radiation, the thermal resistance of the air layer around the tank can be computed with Equation 3.52, with which the heat transfer for that thermal resistance R can be determined with Equation 3.4.2, in which ΔT is the temperature difference across the layer. As the thermal resistance depends on the temperature difference and vice-versa, an iteration loop is required to determine T_{surf} such that the heat flux to satisfy the boil-off rate.

$$R_{\text{air}} = \frac{1}{2\pi r_{\text{tank}} L_{\text{cyl}} + 4\pi r_{\text{tank}}^2} \cdot \frac{1}{h_{\text{rad}} + h_{\text{conv}}} \quad (3.52) \qquad \dot{Q} = \frac{\Delta T}{R} \quad (3.53)$$

With the surface temperature of the tank determined, the heat transfer through the polystyrene insulation layer and aluminium shell can be calculated. This heat transfer happens only through conduction. More specifically, the total conduction of a layer is a combination of conduction of the cylindrical and spherical part of the tank in parallel, and can therefore be computed, similar to electrical resistance, with Equation 3.54. For this, the resistance for the spherical and cylindrical parts of the tank can be computed with Equation 3.55 and Equation 3.56, respectively. In these equations, k is the thermal conductivity of layer material. This is $0.022\ W/m/K$ for the polystyrene insulation layer and $120\ W/m/K$ for the Al2219-T851 shell. Next to that, r_0 is the outer radius of the layer, t is the thickness of the layer and L_{cyl} is the length of the cylindrical centre section of the tank.

$$R_{cond} = \left(R_{cond,sphere}^{-1} + R_{cond,cylinder}^{-1}\right)^{-1} \quad (3.54)$$

$$R_{cond,sphere} = \frac{1}{4\pi k}\left(\frac{1}{r_0 - t} - \frac{1}{r_0}\right) \quad (3.55) \qquad R_{cond,cyl} = \frac{\ln \frac{r_0}{r_0 - t}}{2\pi L_{cyl} k} \quad (3.56)$$

Ahead of sizing the insulation layer, the shell thickness is known from structural sizing (Section 3.4.1), and the allowed heat rate (Equation 3.41) is known based on the mass flow rate to satisfy the dormancy time requirement (Equation 3.40). The temperatures across the insulation and shell layers must be consistent to satisfy the surface temperature of the tank and the hydrogen temperature in the tank, which depend on the insulation thickness, requiring an iterative procedure for correct determination.

As mentioned before, the overall tank sizing procedure is an iterative process as well, as consistent shell and insulation thickness, which depend on the tank diameter, need to be found such that the overall tank still fits within the cabin diameter taking into account a 2% margin.

3.4.3. Tank mass

When the insulation and shell thickness are determined, the tank mass can be determined with the volume that each layer occupies with its thickness and the density of the material. The density of the polystyrene insulation is $32\ kg/m^3$ and the density of the aluminium shell is $2840\ kg/m^3$. To this, mass allowances are added: 4.3% for hydrogen needed to pressurise tank and 0.3% to account for trapped fuel [23]. Next to that, the support structure of the tank is accounted for with a mass allowance of 1.8% [23]. Finally, regulations stipulate that during take-off, every engine is supplied from a separate fuel tank. To ensure this, a tank divider is placed inside the hydrogen tank. As per Onorato et al. [23], the mass of the shell of one tank cap is added to account for this.

3.5. Engine Sizing

With the thrust loading and corresponding take-off thrust that was obtained in the constraint analysis, the size of the engine can be determined. This is done by collecting data from existing turbofan engines and use trendlines to predict the length, diameter and weight of the engine for the conceptual designs in this study. This method was opted for instead of choosing one existing engine to allow for more flexibility in the conceptual design procedure.

The engine data that was obtained and used in the sizing process can be seen in Table 3.3. All data was obtained from the database of Janes[4], except for the IAE V2500-A5 engine, for which the data was obtained from the manufacturer's product card [76] and the EASA type-certificate data sheet [77]. Using this data, linear trendlines are constructed. Figures 3.6a, 3.6b and 3.6c show the data from reference engines and the trendline for the take-off thrust versus dry weight, fan diameter and engine length, respectively. N.B.: the CFM56 appeared to be an outlier regarding engine length and was therefore not included in the trendline for take-off thrust versus engine length. Thereby, the R^2 was increased from 0.3984 to 0.6281 and thereby the accuracy in estimating the length of the engine.

Table 3.3: Engine data used in engine sizing

Engine type	Dry mass [kg]	Take-off thrust [kN]	Diameter [m]	Length [m]
LEAP-1A	3153.00	146.35	1.981	3.328
PW1100G	2857.63	147.28	2.0574	3.40106
PW1900G	2177.24	105.93	1.8542	3.18516
V2500-A5	2404.00	111.20	1.613	3.201
CFM56-5A1	2337.00	111.30	1.735	2.422
PW6000	2289.00	100.00	1.435	2.748

---

[4] `https://customer.janes.com/`

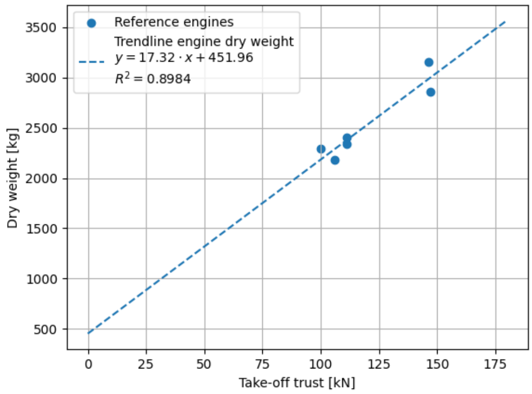

(a) T-O thrust vs. dry weight

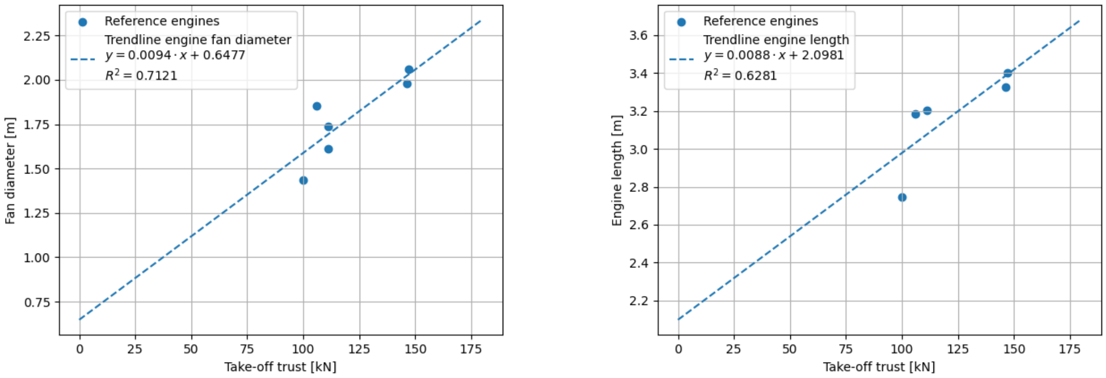

(b) T-O thrust vs. fan diameter

(c) T-O thrust vs. engine length. N.B.: excluding CFM56 engine

Figure 3.6: Reference engine data and trendlines for take-off thrust versus key engine parameters.

To obtain the maximum diameter of the engine, 0.6 meter was added to the fan diameter obtained with the trendline in Figure 3.6b.

Engine positioning

The positioning of the engine in the aircraft concept was done relative to the wing and is based on a study by Lockheed as presented by Torenbeek [62]. The following design rules are adhered to and are schematically shown in Figure 3.7:

- The front of the nacelle is placed at a longitudinal distance of $x = 1.85D$ ahead of the leading edge of the wing (see Figure 3.7b).
- The engine is placed at an outboard lateral position of $y = 0.35\ b/2$ (see Figure 3.7a).
- The centre of the engine is placed at a vertical distance of $z = 0.95D$ below the leading edge of the wing (see Figure 3.7a).

In these rules, D is the maximum engine diameter that was determined above in Section 3.5, and $b/2$ is the semi-span.

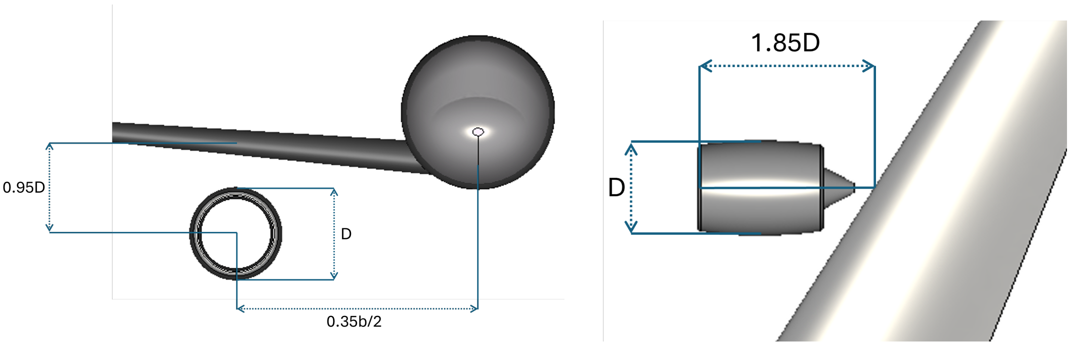

(a) Engine positioning front view **(b)** Engine positioning top view

Figure 3.7: Engine positioning schematic

3.6. Engine Performance Model

To better estimate the fuel use of the dual-fuel aircraft model throughout the mission, information needs to be obtained on the fuel consumption of the turbofan engine at different thrust levels. For this purpose, the Gas turbine Simulation Program (GSP) was used. This is a component-based modelling environment for gas turbines [78]. This tool was used in this study to obtain information on the use of both hydrogen and kerosene in the same engine model. More specifically, the engine model of a CFM LEAP-1A turbofan engine was used. This model was available at NLR to be used and similar to the model used by Ang et al. [79]. A screenshot of this model in GSP is shown in Figure 3.8.

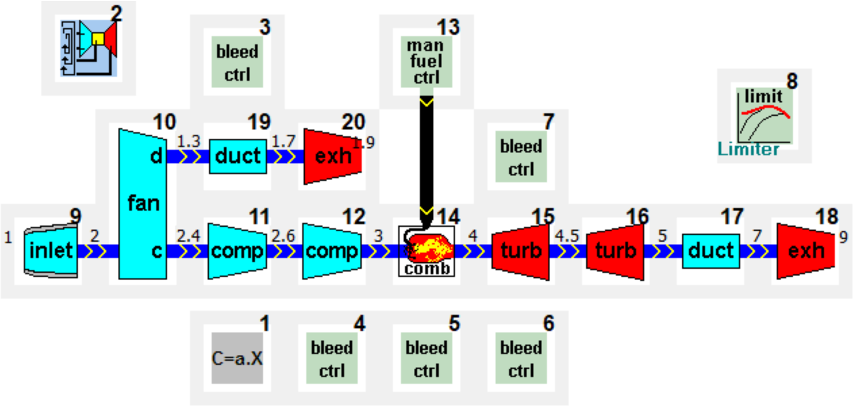

Figure 3.8: LEAP-1A model in the Gas turbine Simulation Program

The goal of using the LEAP-1A model in GSP was to get insight into the performance of the engine at different operating conditions and when using either hydrogen (H_2 gas) or kerosene (Jet-A1). Therefore, a parameter sweep (block 2 in Figure 3.8) was performed for both fuels over the variables altitude, Mach number and fuel flow into the combustion chamber. More specifically, the parameter sweep works as follows: at every altitude step, from 0 to 11000 meter with steps of 1000 meter, the model was run at Mach numbers ranging from 0 to 0.8 with steps of 0.1. At every Mach number, the model was run for a range of fuel flows. For hydrogen, the fuel flow ranges from 0.05 to 0.5 kg/s at steps of 0.05 kg/s. For Jet-A1, the fuel flow ranges from 0.1 to 1.0 kg/s at steps of 0.1 kg/s. These fuel flows were used as they were found to span the operational use of the engine model within the temperature limit of the exit temperature of the combustion chamber, T_{t4}. This temperature limit was implemented with the component limiter (block 8 in Figure 3.8) and set at $T_{t4} = 1765\ K$. This ensured that at every combination of altitude, Mach number and fuel flow, T_{t4} would not go over the limit.

Running the model over the specified parameter sweep provided data on the amount of thrust the engine produces at varying operating conditions and fuel flow, for both fuel types. This data is used in the mission analysis step in the design loop, which is described in Section 3.8.

3.7. Aerodynamic Analysis

The previous section presented the engine performance estimation to be used in the mission analysis. The aerodynamics of the aircraft concept need to be evaluated as well, such that it can be used in the mission analysis. The total drag is a build-up of lift induced drag and parasite drag [80]. The latter consisting of friction drag, interference drag and wave drag. The determination of these drag components will be elaborated upon in this section.

3.7.1. Induced Drag

The lift-induced drag was obtained using the Athena Vortex Lattice program[5]. This program computes the induced drag in the Trefftz plane. Since ParaPy provides a direct link between the aircraft geometry, the induced drag calculation is computed in the design loop taking into account design changes.

The geometry that is used in the AVL analysis consists of the main wing and the horizontal and vertical tailplane surfaces following from the geometry sizing preceding the aerodynamic analysis. These surfaces are discretised with 20 nodes in chordwise direction and 10 nodes in spanwise direction, spaced equally in both directions.

To obtain $C_L - C_{D_i}$ data, the AVL analysis was run at angle of attack α values from 0 to 10 degrees with steps of 2 degrees. This range was chosen as it approximately spans the linear part of the $C_L - \alpha$ curve of the chosen airfoils at the operating Reynolds number at cruise conditions[6].

3.7.2. Skin Friction Drag

Since AVL computes the induced drag of the lifting surfaces using Trefftz plane analysis, it cannot be used to obtain viscous drag components. Therefore, these zero-lift drag (C_{D_0}) components are computed using the drag build-up method presented by Gur et al. [80] and Raymer [71].

The zero-lift drag is computed with Equation 3.57 by summing the C_{D_0}-values of individual components. For each component (subscript c), the flat plate skin friction coefficient C_{f_c}, form factor FF_c, interference factor Q_c and wetted area S_{wet_c} is estimated using semi-empirical relations. This will be elaborated on below.

$$C_{D_0} = \frac{\sum(C_{f_c}\, FF_c\, Q_c\, S_{wet_c})}{S_{ref}} + C_{D_{misc}} \tag{3.57}$$

Lifting surfaces

For the wing and horizontal and vertical tailplanes, the friction drag is computed using the spanwise discretisation from AVL as described before. The flat plate skin friction coefficient is dependent on the amount of laminar versus turbulent flow. For laminar flow $C_{f_{lam}}$ is computed with Equation 3.58 and for turbulent flow $C_{f_{turb}}$ is computed with Equation 3.59, in which Re is the Reynolds number of the strip and M is the Mach number. The combined C_f for the section of the surface strip is a weighted average between $C_{f_{lam}}$ and $C_{f_{turb}}$, as can be seen in Equation 3.60, in which δ_{lam} is the fraction of laminar flow over the strip. This is computed with Equation 3.61. The Reynolds numbers in this equation will be elaborated on below.

$$C_{f_{lam}} = \frac{1.328}{\sqrt{Re}} \tag{3.58}$$

$$C_{f_{turb}} = \frac{0.455}{(\log_{10} Re)^{2.58} \cdot (1 + 0.144M^2)^{0.65}} \tag{3.59}$$

$$C_f = \delta_{lam} \cdot C_{f_{lam}} + (1 - \delta_{lam}) \cdot C_{f_{turb}} \tag{3.60}$$

$$\delta_{lam} = \frac{Re_{trans}}{Re_{chord}} \tag{3.61}$$

In Equation 3.61, Re_{trans} is the Reynolds number at which the flow is estimated to transition naturally from laminar to turbulent. Based on Gur et al. [80], Re_{trans} is estimated to be $5 \cdot 10^6$ for a technology factor of 0 for (natural laminar flow on standard wings) for leading-edge sweep angle below $35°$. This is a conservative estimate as the aircraft concepts in this study will have a leading-edge sweep angle

---

[5] `https://web.mit.edu/drela/Public/web/avl/`

[6] `http://airfoiltools.com/airfoil/details?airfoil=n63415-il`
`http://airfoiltools.com/airfoil/details?airfoil=whitcomb-il`

around $30°$, for which the transition Reynolds number would be higher, and therefore the amount of skin friction drag lower due to increased laminar flow.

Re_{chord} in Equation 3.61 is calculated with Equation 3.62, in which l is the characteristic length, which is the chord length of the wing strip, and ν is the kinematic viscosity at cruise velocity. This Reynolds number is used to calculate $C_{f_{lam}}$ in Equation 3.58. Per Raymer [71], the Reynolds number used to calculate $C_{f_{turb}}$ in Equation 3.59 depends on the cut-off Reynolds number Re_{cutoff}. This value takes into account surface roughness and is calculated with Equation 3.63 for transonic conditions. In this equation, l is the characteristic length of the component evaluated, the chord length of the strip in case of a lifting surface, k is a skin roughness estimate and M is the Mach number. k is taken to be $0.634 \cdot 10^{-5}\ m$ for smooth paint [71]. If the cut-off Reynolds number is lower than the actual Reynolds number, it means the roughness of the skin will increase the drag. In that case, Re_{cutoff} is used in Equation 3.59 to estimate $C_{f_{turb}}$. If the actual Reynolds number is already higher than the cut-off Reynolds number, then this value is used in Equation 3.59.

$$Re = \frac{V \cdot l}{\nu} \quad (3.62) \qquad R_{cutoff} = 44.62 \left(\frac{l}{k}\right)^{1.053} M^{1.16} \quad (3.63)$$

The form factor FF_c of the wing and tail surface elements are calculated using Equation 3.64, in which $(x/c)_m$ is the chordwise position of the maximum thickness point of the airfoil and Λ_m refers to the sweep of this maximum-thickness line. For the high-speed airfoils of the wing these are assumed to lie at 0.5 of the chord, whereas for the low-speed airfoils of the tail surfaces these are assumed to lie at 0.3 of the chord [71]. Next to that, Raymer [71] states that 10% needs to be added to the form factor the the tail surfaces to account for additional drag due to hinged elevators and rudder.

$$FF = \left[1 + \frac{0.6}{(x/c)_m}\left(\frac{t}{c}\right) + 100\left(\frac{t}{c}\right)^4\right]\left[1.34 M^{0.18} (\cos\Lambda_m)^{0.28}\right] \quad (3.64)$$

Regarding the interference factor Q of wing and tail surfaces, Raymer [71] stipulates $Q_{wing} = 1.0$, $Q_{HT} = 1.05$ and $Q_{VT} = 1.05$ for the wing, horizontal and vertical tailplane, respectively.

Fuselage

To estimate the skin friction drag of the fuselage, the form factor is computed with Equation 3.65, in which f is the fineness ratio of the fuselage that can be obtained based on the length l and diameter d of the fuselage using Equation 3.66.

$$FF = 1 + \frac{60}{f^3} + \frac{f}{400} \quad (3.65) \qquad f = \frac{l}{d} \quad (3.66)$$

Similar to the wing and tail, the flat plate friction coefficient of the fuselage is a combination of the laminar and turbulent flat plate friction coefficients from equations 3.58 and 3.59, weighted by δ_{lam} in Equation 3.61. For the fuselage, Re_{chord} (Equation 3.62) and Re_{cutoff} (Equation 3.63) is computed for a characteristic length l equal to the fuselage length. Per Raymer [71], $Q_{fus} = 1.0$ is taken as the interference factor for the fuselage.

Engines

To estimate the friction drag of the engines the method by Moens [81] is adhered to. This method estimates the drag contributions of the engine nacelle and engine core separately, and combines them to obtain the total engine drag using Equation 3.67. For the form factor to compute the nacelle and core drag Equation 3.68 is used. The flow around around the nacelle and engine core is assumed to be fully turbulent, so the flat plate skin friction coefficient from Equation 3.59 is used, for which the Reynolds number is calculated with Equation 3.62 using the length of the nacelle and engine core. The interference factor Q_N is taken to be 1.3, as the engine is placed under the wing less within one diameter of the wing [71].

$$C_{D_{eng}} = N_{eng}\left(Q_N\, C_{D_{nac1}} + C_{D_{nac2}}\right) \quad (3.67)$$

$$FF_{nac} = 1 + 0.35\frac{D_{nac}}{L_{nac}} \quad (3.68)$$

The total skin friction drag is obtained by summing the friction drag components for the lifting surfaces, fuselage and engines. The miscellaneous drag contribution $C_{D_{misc}}$ in Equation 3.57 accounts for protuberances like antennas and probes 2.5% is added to the total friction drag [81].

3.7.3. Wave Drag

The aerodynamics of the aircraft concept will be evaluated at cruise conditions. As this is in the transonic regime, wave drag needs to be determined to account for the occurrence of shock waves. This will be calculated with Lock's fourth power law, which can be seen in Equation 3.69 [80]. Just like the friction drag, the wave drag will be evaluated per wing strip and summed to find the total wave drag. The contribution of each wing strip will be scaled by the area of the wing strip S_c relative to the wing area S_{ref}. The wave drag contribution is only valid if the Mach number M is larger than M_{cr}. Otherwise, C_{D_w} will be 0 for that strip.

$$C_{D_w} = 20(M - M_{cr})^4 \, \frac{S_c}{S_{ref}} \tag{3.69}$$

The critical Mach number M_{cr} is computed with Equation 3.70, in which M_{DD} is the drag divergence Mach number. This can be computed with Equation 3.71. In this equation, $\Lambda_{c/2}$ is the half-chord sweep angle, t/c is the thickness-to-chord ratio of the strip, C_l is the lift coefficient of the strip, and κ_A is the Korn factor. This Korn factor depends on the airfoil. In this drag estimation, a Korn factor of 0.95 for supercritical airfoils is chosen for estimating the wing wave drag, whereas for the horizontal and vertical tailplane with a conventional airfoil a Korn factor of 0.87 is chosen [80].

$$M_{cr} = M_{DD} - \sqrt[3]{\frac{0.1}{80}} \tag{3.70}$$

$$M_{DD} \cos \Lambda_{c/2} + \frac{C_l}{10 \cos^2 \Lambda_{c/2}} + \frac{t/c}{\cos \Lambda_{c/2}} = \kappa_A \tag{3.71}$$

The wave drag estimation procedure described above is applied to the wing, horizontal tailplane and the vertical tailplane. As no sideslip angle is included in the analysis, the part in second fraction in Equation 3.71 will be zero for the vertical tailplane, as C_l will be zero.

3.8. Mission Analysis

The previously described engine performance and aerodynamic model are used to perform a mission analysis of the dual-fuel aircraft concept. This mission analysis was performed using the Mission, Aircraft and Systems Simulation (MASS) tool developed by NLR[7]. This tool enables the integration of a specified mission model with data on the aircraft aerodynamic performance and powertrain system to estimate the fuel burn throughout the mission.

Mission profile

The mission profile that is analysed in the mission analysis consists of a regular cruise mission and a reserve mission. This reserve part of the total mission follows from a missed approach, after which the aircraft climbs to the altitude at which the reserve distance as specified by the TLARs is flown. The second part of the reserve mission is the loiter phase. This follows after a descend phase of the aircraft from reserve altitude to the altitude at which the loiter part is flown for the duration as specified in the TLARs. After the loiter phase, the aircraft descends further and lands. A climb rate of 2000 feet per minute and a descend rate of 3500 feet per minute are adhered to for the climb and descend phases in the mission and obtained from mission profile data from the Airbus A320neo[8].

Fuel priority

In the Class I weight estimation, Section 3.2.1, the fuel split parameter was introduced. This specifies what part of the mission will be flown on either hydrogen or kerosene (Jet-A1). The fuel priority parameter is used to specify which fuel will be used first when a mission phase uses both fuels, so if the fuel split is between 0 and 1. The fuel priority can be specified per mission phase in the design tool to be 1 (hydrogen used first) or 0 (Jet-A1 used first). Figure 3.9 shows an example of a mission profile used as the mission analysis with MASS. The mission is flown on hydrogen until 75% of the cruise phase.

---

[7] `https://www.nlr.org/flyers/en/f543-analyse-the-energy-performance-of-aircraft.pdf`

[8] `https://skybrary.aero/aircraft/a20n`

Then, the remainder of the cruise phase, descend and first part of the reserve phase is flown on Jet-A1. The second half of the reserve phase is flown on hydrogen, and the loiter and landing phase are flown on Jet-A1.

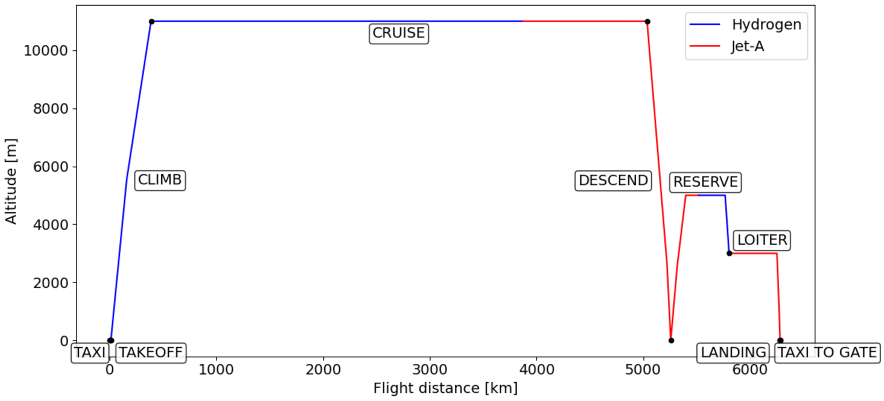

Figure 3.9: Example mission profile demonstrating fuel split

Calculation steps in MASS

With the specified mission profile taking into account the fuel split and priority, the fuel mass is calculated in MASS through a few subsequent steps.

First of all, the mission profile is discretised into a timeseries where each point contains the state of the aircraft at that point (time, altitude, distance, velocity). This state is used to compute the weight, lift, drag and thrust forces on the aircraft considering the aircraft as a point mass. The $C_L - C_D$ data from the aerodynamic analysis is used in this step. N.B.: lift and drag contributions of flaps and landing gear are not considered. Also, the force estimation is done with the drag polar evaluated at cruise conditions throughout the mission.

Secondly, the specified fuel split and fuel priority inputs are used to assign the fuel switch in the discretised mission profile. The point where this fuel switch between hydrogen and Jet-A1 happens is assigned based on the length of the mission phase and the specified fuel split percentage of that phase. The assumption is therefore made that switching fuels happens instantly.

Thirdly, with the required thrust estimated, the fuel mass flow is determined at every time step. For this, the LinearNDInterpolation function in SciPy is used to obtain linear relationships between flight conditions, mass flow and the required thrust. This is done by using the altitude, Mach number and fuel mass flow inputs, and the resulting thrust data outputs from the parameter sweep in GSP that was described in Section 3.6. Then these linear relationships can be used to estimate the fuel mass flow of hydrogen Jet-A1 at every time step in the mission based on the flight conditions and thrust requirement specified at these steps. The fuel split and fuel priority are used to assign either the mass flow of hydrogen or Jet-A1 to that time step. The fuel weight is then found by cumulatively summing the mass flow values of the whole mission. The hydrogen and Jet-A1 fuel weight are obtained separately by cumulatively summing the fuel mass flows of the points where either hydrogen or Jet-A1 is used.

As a last step, MASS checks the consistence between the MTOW, OEW and payload provided as inputs, and the updated MTOW, i.e. the sum of the fuel weight, OEW and payload. The error between the initial and updated MTOW has to fall within a tolerance of 0.1% of the fuel weight. If this criterion is not met, the calculation steps described above are performed again with the updated MTOW as starting weight until consistence between the inputs and outputs are reached within the tolerance. Therefore, the outcomes of the mission analysis are the separate hydrogen and Jet-A1 fuel use, and the updated MTOW.

3.9. Class II Weight Estimation

With the sized aircraft geometry, tank sizing, engine sizing, and fuel weight estimate from the mission analysis, a Class II weight estimation is performed. This means that the operational empty weight of the aircraft is obtained by estimating the weight at component level using semi-empirical methods or previously determined component weights. The latter is the case for the hydrogen tank, of which the weight was determined after structural and thermal sizing (Section 3.4), and the engines, of which the weight was determined using the relation between take-off thrust and engine weight based data from reference engines (Section 3.5).

The OEW estimate from Class II is a combination of the aircraft structure, fuel system, propulsion system and fixed equipment. For most of the components in these categories, the empirical relations from Torenbeek as presented by Roskam [82] are used, whereas the nacelle weight is estimated based on the empirical relation from Raymer [71]. However, the use of both hydrogen and kerosene in this aircraft concept, requires special attention to the weight estimation of some components. These will be presented below. Subsequently, the estimation of the centre of gravity is shown.

3.9.1. Wing weight

In a conventional aircraft flying on kerosene, (most of the) fuel is stored in the wings. This provides bending relief to the wing structure. For the dual-fuel aircraft in this study, it can occur that only little to none kerosene is used throughout the mission, and therefore that this bending relief will not be present. A correction is added to the empirical wing weight estimation from Torenbeek as presented by Roskam [82] to account for this. This relation is shown in Equation 3.72. In this equation, W_{ZF} is the zero fuel weight, b is the wing span, S is the wing area, t_r is the thickness of the wing root, $\Lambda_{c/2}$ is the sweep angle at half-chord, and n_{ult} is the ultimate load factor. In this equation, all weights are in pounds and the dimensions in feet, but the wing weight is converted to kilograms. The minimum load factor from CS25-regulations is 2.5, to which a safety factor of 50% is applied such that the ultimate load factor is 3.75. To this wing weight, corrections are applied as specified by Roskam [82]: 2% is added for spoilers and speed brakes, 2% is added for Fowler flaps, and 5% is subtracted as the engines are wing mounted.

$$W_w = 0.0017 W_{ZF} \left(\frac{b}{\cos\Lambda_{c/2}}\right)^{0.75} \left[1 + \left(\frac{6.3\cos\Lambda_{c/2}}{b}\right)^{0.5}\right] n_{ult}^{0.55} \left(\frac{b \cdot S}{t_r W_{ZF} \cos\Lambda_{c/2}}\right)^{0.3} \tag{3.72}$$

Another correction factor $k_{semidry}$ is applied to correct for the reduced fuel weight in the wing. This correction factor is based on the work by Healy et al. [26]. They investigated the wing increase in wing weight due to dry wings compared to an A320 reference aircraft. They found that for the 36 wing span limit considered in this study, wing weight increases with 3.5% for a dry wing compared to a wet wing. Also, a study by Taflan et al. [83] showed that the weight of a Boeing 737 wing increased with 3.42% compared to the baseline wing, thus supporting the findings by Healy et al. Therefore, it was decided tot take a 3.5% weight penalty as a baseline correction factor for a dry wing k_{dry}. To go from k_{dry} to $k_{semidry}$, the kerosene weight on board is compared to the fuel capacity of the wing. The total tank volume was estimated with the empirical relation Equation 3.73 [62]. In this equation, λ is the taper ratio of the wing and τ is the ratio between the thickness-to-chord ratio of the tip and the root.

$$V_{cap,tank} = 0.54 \frac{S^2}{b} (t/c)_r \frac{1 + \lambda\sqrt{\tau} + \lambda^2\tau}{(1+\lambda)^2} \tag{3.73}$$

Converting V_{tank} from ft^3 to m^3 and multiplying with a fuel density for Jet-A1 of $\rho = 800\ kg/m^3$, the fuel capacity $m_{cap,tank}$ in kg is found. $k_{semidry}$ is then found using Equation 3.74, in which m_{JetA} is the weight of Jet-A1 on board from the mission analysis. Torenbeek [62] states that the accuracy of Equation 3.73 is not very high. Therefore, $k_{semidry}$ is set to be always 1 or higher.

$$k_{semidry} = 1 + k_{dry} \frac{(m_{cap,tank} - m_{JetA})}{m_{cap,tank}} \tag{3.74}$$

3.9.2. Fuel system weight

The dual-fuel aircraft concept contains both a hydrogen and a kerosene fuel system. As previously mentioned during the Class I weight estimation in Section 3.2.1, the hydrogen fuel system weight is computed with Equation 3.12, in which a correction factor $k_{fs} = 0.5$ based on Onorato et al. [23] was applied. This equation is again applied in Class II, using the hydrogen weight from the mission analysis converted to litres with $\rho = 71\ kg/m^3$. For the kerosene fuel system, Equation 3.12 was also used, but then without the k_{fs} correction factor, the number of fuel tanks $N_{ft} = 2$ for both wings, and also the kerosene weight from the mission analysis converted to litres with $\rho = 800\ kg/m^3$ is used.

3.9.3. Propulsion system weight

The relation for propulsion system weight W_{apsi} (accessory drives, powerplant controls, starting and ignition systems) from Torenbeek as presented by Roskam [82] is shown by Equation 3.75, in which N_{eng} is the number of engines and $\dot{m}_{f,TO}$ is the fuel mass flow rate at take-off. To take into account the possibility of using hydrogen or kerosene to propel the aircraft, this mass flow rate is computed by summing the maximum mass flow rate of hydrogen and kerosene that could occur throughout the mission profile in the mission analysis, irrespective of what fuel is assigned to be used at that point in the mission. This way, a conservative weight estimate of the propulsion system is made.

$$W_{apsi} = 36 N_{eng}\ \dot{m}_{f,TO} \tag{3.75}$$

3.9.4. Centre of gravity estimation

The centre of gravity (CG) of the aircraft can be estimated with the component weights and their respective positions along the aircraft. The calculation is split into the centre of gravity of the fuselage group, containing the fuselage, hydrogen tank, empennage and fixed equipment, and the wing group, containing the wing, engines and nacelles. Although the landing gear was included in the Class II weight estimation, it was not included in the CG estimation, as the CG of the landing gear is assumed to lie at the CG location of the aircraft. The CG locations of components is obtained either by built-in CG attributes in the ParaPy geometry, or estimated based on Torenbeek [62] are used. Additionally, the CG of the engines is assumed to lie at the same position at the CG of the nacelles from Torenbeek, i.e. at 40% of the nacelle length. The CG of the fixed equipment is assumed to lie at the same position of the fuselage CG. The CG of the hydrogen fuel system is located at the same position as the hydrogen tank. The CG of the kerosene fuel system is located at the In determining the CG of the empty aircraft, the wing is positioned such that the CG of OEW lies at 30% of the MAC of the wing.

Taking into account fuel and payload, the most forward and aft CG positions can be determined. This is done by evaluating Equation 3.76 for the following combinations of OEW, payload and fuel:

- OEW + payload + hydrogen + kerosene
- OEW + payload
- OEW + payload + hydrogen
- OEW + payload + kerosene
- OEW + hydrogen
- OEW + kerosene
- OEW + hydrogen + kerosene

For these CG options, it is assumed that the CG of payload lies halfway the passenger section, l_{pax}, as shown in Figure 3.3, CG of hydrogen aligns with the CG of the hydrogen tank and kerosene aligns with the CG of the wing.

$$X_{CG} = \frac{\sum(X_{CG,i} \cdot W_i)}{\sum W_i} \tag{3.76}$$

A margin of 2% of the MAC length is applied to the most forward and aft CG to account for slight changes in CG location due to e.g. moving passengers.

3.10. Longitudinal Static Stability

As the dual-fuel aircraft contains a heavy hydrogen tank in the back of the fuselage, it is important that the longitudinal static stability is ensured. This is done by making sure the static margin is large enough. The static margin is computed with Equation 3.77, in which X_{np} is the neutral point of the aircraft, $X_{CG,aft}$ is the most aft CG from the CG range as described in Section 3.9.4, and $\bar{c}$ is the MAC length.

$$SM = \frac{(X_{np} - X_{CG,aft})}{\bar{c}} \tag{3.77}$$

The neutral point of the aircraft at cruise conditions is obtained from AVL. However, some corrections need to be applied to this neutral point to account for (de)stabilizing effects of the fuselage and nacelles, $\Delta\left(\frac{x_{np}}{\bar{c}}\right)_{fus}$ and $\Delta\left(\frac{x_{np}}{\bar{c}}\right)_{nac}$, respectively, causing a shift in neutral point. $\bar{x}$ means x is non-dimensionalised by the MAC length $\bar{c}$. The neutral point corrections are taken from Torenbeek [62].

$$\Delta\left(\frac{x_{np}}{\bar{c}}\right)_{fus} = -\frac{1.8}{C_{L_{\alpha_{A-h}}}}\frac{b_f h_f l_{fn}}{S\bar{c}} + \frac{0.273}{1+\lambda}\frac{b_f c_g (b-b_f)}{\bar{c}^2(b+2.15b_f)}\tan\Lambda_{c/4} \tag{3.78}$$

Equation 3.78 above shows the calculation of the neutral point shift due to fuselage contribution. The first (negative) part of the equation is related to the fuselage nose contribution to lift generation, which has a destabilizing effect. The second (positive) part of the equation accounts for the loss of lift at the wing-fuselage intersection, which has a stabilizing effect. In the equation, $C_{L_{\alpha_{A-h}}}$ is the lift-curve slope of the aircraft less horizontal tail. This is estimated using the DATCOM method for swept wings in compressible flow as presented by Torenbeek [62]. b_f and h_f are respective width and height of the fuselage (equal in this study), whereas l_{fn} is the distance of the nose of the fuselage to the wing intersection with the fuselage. c_g is the geometric chord and equals $\frac{S}{b}$ and $\Lambda_{c/4}$ is quarter chord sweep angle of the main wing.

The neutral point shift due to the nacelles is computed with Equation 3.79 below. In this equation, k_n is a factor accounting for the engine type. For nacelles mounted in front of the leading edge of the wing it equals -4. b_n is the width of the nacelle and l_n is the distance between the quarter-chord MAC and the front of the nacelle.

$$\Delta\left(\frac{x_{np}}{\bar{c}}\right)_{nac} = \sum_{i=1}^{N_{eng}} k_n \frac{b_n^2 l_n}{S\bar{c}} \tag{3.79}$$

The corrected neutral point is obtained by adding the neutral point shifts due to the fuselage and nacelles to the chord non-dimensionalised neutral point from AVL $\frac{x_{np}}{\bar{c}}$. This corrected neutral point can be used to check the static margin of the aircraft. A minimum static margin of $0.05\bar{c}$ is used in this study. When this value is not reached, it means that the area of the horizontal tailplane S_h is not large enough. Equation 3.80 below is used to compute the ratio of horizontal tailplane to the wing area to satisfy a static margin of $0.05\bar{c}$. In this equation, the lift-curve slopes of the horizontal tailplane and aircraft less tail, $C_{L_{\alpha_h}}$ and $C_{L_{\alpha_{A-h}}}$, are again estimated using the DATCOM method as described by Torenbeek [62]. Furthermore, $\bar{x}_{ac}$ is the aerodynamic centre of the wing. This value is obtained as the neutral point from AVL when running the AVL analysis only for the wing surface without the empennage surfaces. To this wing aerodynamic centre the same fuselage and nacelle corrections from Equation 3.78 and Equation 3.79 are applied as for the neutral correction of the whole aircraft. Next to that, l_h is the tail arm of the horizontal tail, and $\left(\frac{V_h}{V}\right)^2$ is the tail to wing velocity ratio, which equals 0.85 for a fuselage mounted horizontal tailplane [84]. Finally, $\frac{d\varepsilon}{d\alpha}$ is the downwash gradient, which is estimated based on the method by Slingerland as presented by Oliviero [84]

$$\frac{S_h}{S} = \frac{1}{\left[\frac{C_{L_{\alpha_h}}}{C_{L_{\alpha_{A-h}}}}\left(1-\frac{d\varepsilon}{d\alpha}\right)\frac{l_h}{\bar{c}}\left(\frac{V_h}{V}\right)^2\right]}\bar{x}_{cg} - \frac{\bar{x}_{ac} - 0.05}{\left[\frac{C_{L_{\alpha_h}}}{C_{L_{\alpha_{A-h}}}}\left(1-\frac{d\varepsilon}{d\alpha}\right)\frac{l_h}{\bar{c}}\left(\frac{V_h}{V}\right)^2\right]} \tag{3.80}$$

This tail-to-wing area ratio is applied in the design loop to increase the area of the horizontal tailplane if the static margin is too small.

3.11. Emissions & Energy

Next to aircraft design parameters and weight of the aircraft structure, hydrogen and kerosene, the performance of the dual-fuel aircraft concept is evaluated from an emissions and energy consumption point of view. This section will describe how these performance indicators will be obtained.

From the fuel use of the aircraft concept, the CO_2 emissions will be determined. Following the approach presented by Smith & Mastorakos [50], the CO_2 emissions are obtained using the Carbon Intensity (CI) parameter. This parameter, with unit kg_{CO_2}/MJ, takes into account CO_2 emissions associated with the production and utilisation of one unit energy of fuel. This way, the in-flight emissions from using kerosene can be compared to the emissions from production of hydrogen. The total amount of CO_2 emissions of both fuels is computed from the total energy consumption with Equation 3.81. The total energy consumption is a combination of the well-to-tank and tank-to-wake energy consumption, E_{w-t} and E_{t-w}, respectively.

$$m_{CO_2} = CI \cdot (E_{w-t} + E_{t-w}) \tag{3.81}$$

The tank-to-wake energy consumption is computed with Equation 3.83, in which the mass of the fuel component is multiplied with its lower-heating-value (LHV). The well-to-tank energy consumption takes into account the amount of energy needed to produce the fuel. Similar to Smith & Mastorakos [50], this energy contribution is neglected for kerosene (Jet-A1) utilisation, as Howe et al. [85] estimated that 99.9% of the life-cycle emissions of commercial aircraft is associated with the operation of the aircraft, such that the well-to-tank energy consumption of kerosene use is negligible compared to the tank-to-wake energy consumption. For liquid hydrogen fuel, the well-to-tank energy consumption is computed with Equation 3.82, in which η_e is the efficiency of hydrogen electrolysis and e_l is the energy required to liquefy one kilogram of hydrogen. Currently, the most common way to produce hydrogen is from fossil fuels through steam reforming of natural gas [86]. However, this method has a very high CI. In most cases even higher than using fossil fuels directly in an aircraft [50]. Therefore, hydrogen production through electrolysis will be considered in this study.

$$E_{w-t} = M_{fuel} \cdot \left(LHV_{fuel} \left(\frac{1}{\eta_e} - 1 \right) + e_l \right) \tag{3.82}$$

$$E_{t-w} = M_{fuel} \cdot LHV_{fuel} \tag{3.83}$$

Next to electrolysis to produce the hydrogen, also energy for the liquefaction of hydrogen is assumed to be grid electricity. This electricity is assumed to be derived from a mix of renewable sources and fossil fuels. Smith and Mastorakos [50] present an estimation of the CI of the decarbonising world average electricity grid from 2021 to 2050. Next to that, they present estimates of the increase in efficiency of electrolysis, as well as the reduction of energy required for hydrogen liquefaction in the future based on literature. These projections will be used to determine the emissions and energy of the aircraft concept if it would be flying now in 2025, if it would entre service in 2035, and in the distant future (2050), for which values in Table 3.4 will be used.

Table 3.4: Emissions and technology projections of electricity and hydrogen production, from [50]

Year	Carbon intensity of world-average electricity grid, CI $[kg_{CO_2}/MJ]$	Efficiency of electrolysis, η_e $[-]$	Energy required for liquefaction, e_l $[kWh/kg]$
2025	0.115	0.696	6.26
2035	0.091	0.715	6.02
2050	0.0561	0.718	6.00

Next to these values, Smith & Mastorakos [50] estimate the CI of Jet-A1 fuel at a constant value of 0.106 $[kg_{CO_2}/MJ]$. Using these values in the aforementioned equations, the total CO_2 emissions and energy consumption can be computed for 2025, 2035 and 2050. e_l is converted to MJ/kg by multiplying the values in Table 3.4 with 3.6. Finally, the equivalent CO_2 emissions, CO_2eq $[g/PAX/km]$, and specific energy consumption, SEC $[MJ/PAX/km]$, are computed by dividing the total amount of CO_2 emissions and total energy consumption by the number of passengers and the distance covered over the total mission.

3.12. Overview of Assumptions

Below, an overview of the assumptions that were made in the methodology is presented.

- Fuselage shape is circular.
- Fuselage diameter is sized for passenger accommodation, limited additional cargo is assumed to fit within the fuselage.
- The passenger accommodation is based on a single-class layout, so with constant seat width and pitch throughout the cabin.
- The end cap of the hydrogen tank aligns with fuselage tailcone. It is assumed that enough space is left for the auxiliary power unit, other systems and empennage structure.
- The insulation layer of the hydrogen tank is sized for a dormancy time of 12 hours at sea level conditions.
- The thickness-to-chord ratio and circumference along the wingspan is obtained through linear interpolation from root to tip.
- The lift-drag polar is obtained at cruise conditions and used throughout the whole mission analysis.
- Lift and drag contributions of flaps and landing gear are not considered in the mission analysis.
- Fuel switch between hydrogen and Jet-A1 happens instantly. The location along the mission profile is assigned based on the length of the mission phase and the specified fuel split percentage.
- CG of the operational empty weight of the aircraft is assumed to lie at 30% of the MAC
- The CG of the landing gear is assumed to align with the overall aircraft CG.
- Fixed equipment CG aligns with the fuselage CG.
- Engine performance data is obtained for only one engine geometry model and does not scale with engine sizing.
- Combustion modelling of hydrogen and Jet-A1 in GSP is limited to 0-dimensional chemical equilibrium and does not take into account component level engine effects from combusting either hydrogen or Jet-A1.
- Engine model TIT limit applies to both take-off and cruise conditions
- Vertical tail sizing is only done based on the tail arm between wing and vertical tailplane aerodynamic centres. Directional stability and OEI conditions are not taken into account.
- Aerodynamic centre of horizontal and vertical tail used to obtain the tail arm to the wing lies at c/4 of their respective MAC
- Electricity for hydrogen electrolysis and liquefaction is obtained from the world-average electricity grid.
- Aircraft model always includes hydrogen tank, also if no hydrogen is specified for the mission.
- Fuel enters the combustion chamber of the engine model at room temperature.
- Landing gear sizing and positioning not taken into account, whereas weight estimation includes landing gear weight weight.
- Aeroelastic effects of semi-dry wings with reduced bending relief were not taken into account.
- Fuselage structure around hydrogen tank is similar to fuselage structure at passenger accommodation.
- Well-to-tank energy consumption of kerosene is negligible compared to the tank-to-wake energy consumption. Therefore, only the tank-to-wake energy consumption and accompanying equivalent emissions from kerosene are considered.
- The carbon intensity of kerosene is constant from 2025 to 2050.

4

Verification & Validation

The methods that were previously described were verified and validated for their correct and reliable functioning on several aspects. This chapter will describe the verification and validation of the model in Section 4.1 and Section 4.2, respectively.

4.1. Verification

4.1.1. Aerodynamic model

The drag polar from obtained from the aerodynamic model will be used in the mission analysis. Therefore, it is important to verify its functioning. Below, the induced drag from AVL will be discussed. Subsequently, the build-up of the drag polar for the separate drag components will be shown.

Induced drag scaling

As described in Section 3.7, the induced drag is obtained from the Trefftz plane in AVL. Upon verification of this induced drag, it was discovered that AVL estimates this too low compared to the theoretical estimate of the induced drag. Figure 4.1 shows a comparison between the induced drag from AVL and the theoretical induced drag, computed with Equation 4.1, for an Oswald span efficiency factor e of 0.8, 0.85 and 0.9. It was found that AVL overestimates this span efficiency factor. A possible reason for this is the fact that uniform spacing was used for the vortex and panel distribution in spanwise and chordwise direction [87]. In order to estimate the induced drag more realistically, a scaling factor of 0.8 was applied. Figure 4.1 shows the resulting induced drag estimation. With the scaling applied, it falls in between the theoretical induced drag for Oswald span efficiency factors of 0.8 and 0.85, which are typical figures for high-subsonic jet transport aircraft [62].

$$C_{D_i} = \frac{C_L^2}{\pi A e} \tag{4.1}$$

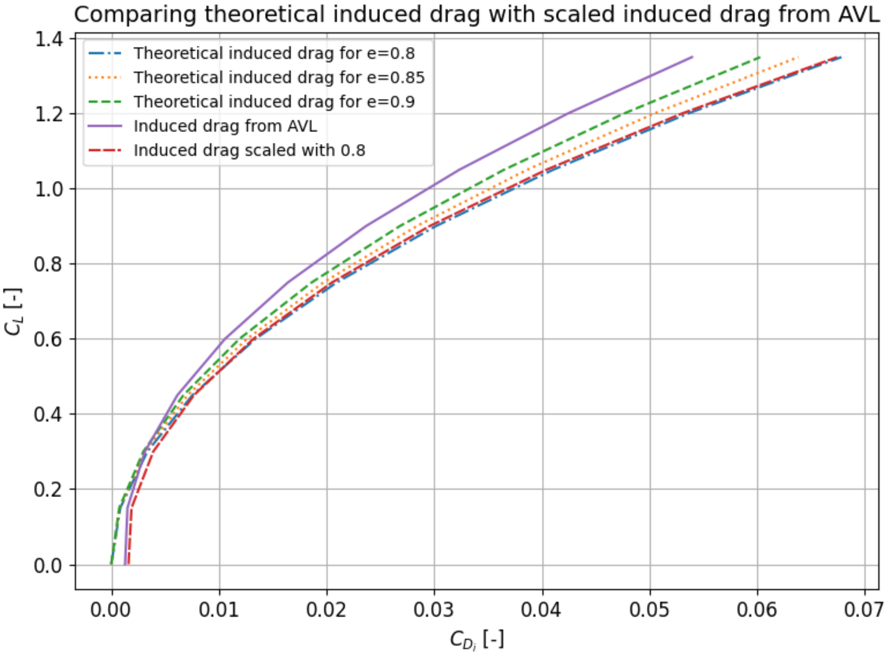

Figure 4.1: Induced drag from AVL compared to theoretical induced drag

Drag polar build up
Figure 4.2 shows the build-up of the drag polar from the aerodynamic analysis for the induced drag, skin friction and wave drag components. It can be seen that the skin friction drag is predominant in the zero-lift drag build-up, which was expected for this type of aircraft with thickness-to-chord ratios below 20% and long, slender fuselage [62].

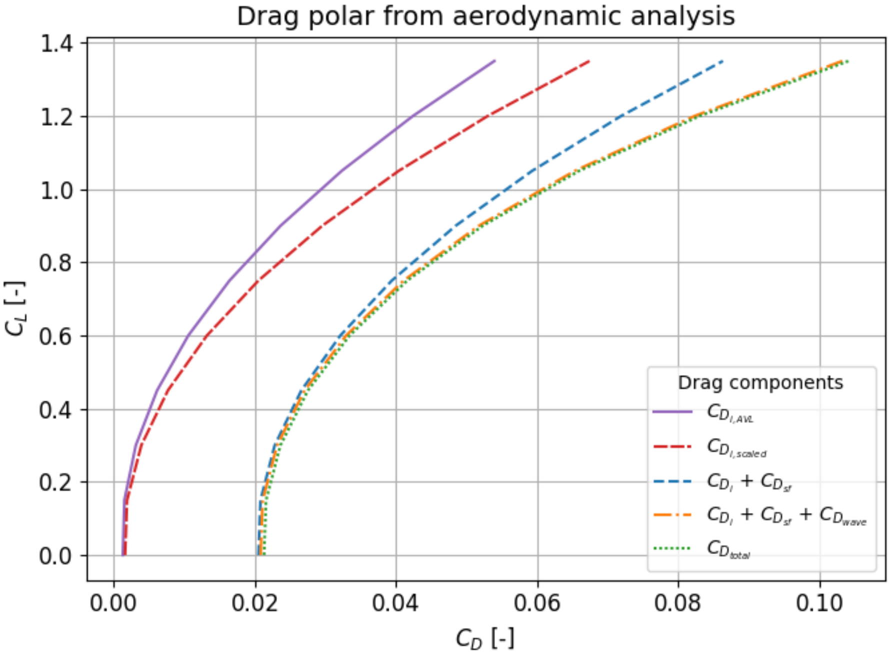

Figure 4.2: Drag polar build-up

4.1.2. Engine model

The working of the engine model is verified by investigating the relation between thrust and fuel mass flow. Figure 4.3 shows the relation between thrust and fuel mass flow from the engine model at a range of Mach number and altitude conditions for both hydrogen and Jet-A1. The conditions at M=0 and h=0, and M=0.8 and h=11000 are the outer limits of the available engine data. At increasing altitude and Mach number, the data for the highest mass flow is reduced for both fuel types. This is due to the fact that data points are removed at certain Mach number and altitude combinations for mass flows at which the limit on the turbine inlet temperature (TIT) is reached for the first time.

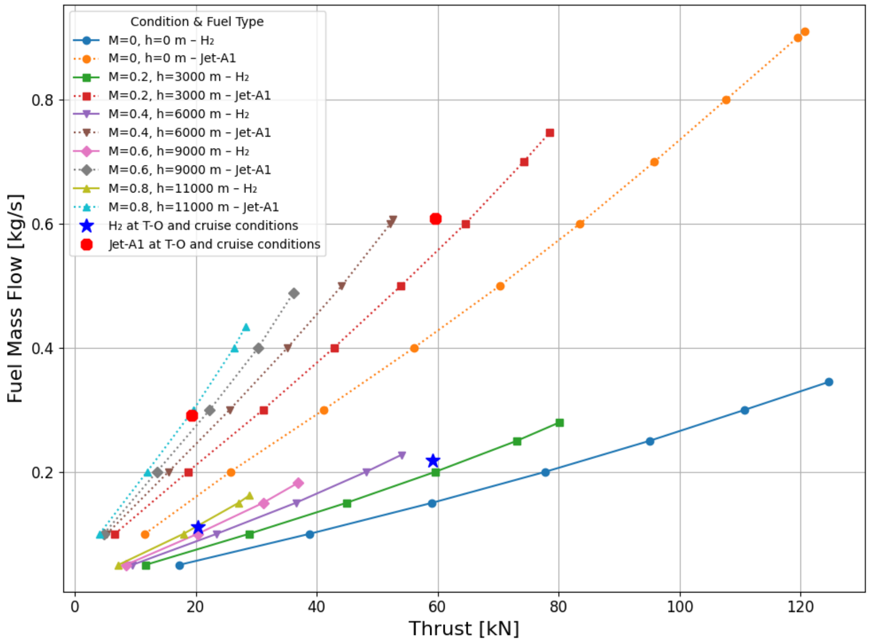

Figure 4.3: Thrust versus fuel mass flow at take-off and cruise conditions

To further check the correct use of the engine data, the maximum required thrust and fuel massflow during the take-off and cruise phases are checked. This is done for both a full hydrogen and a full kerosene aircraft concept, as will be used in the model validation in Section 4.2.4 as well. Table 4.1 below shows the maximum fuel flow and thrust per engine occurring for the evaluation of a full hydrogen and full kerosene aircraft concept generated with the design tool. Figure 4.3 also includes markers for these values.

Table 4.1: Maximum fuel flow and thrust per engine

Parameter	Full hydrogen concept	Full kerosene concept
Max. $\dot{m}_{f,TO}$ $[kg/s]$	0.2186	0.6086
Max. $\dot{m}_{f,cruise}$ $[kg/s]$	0.1110	0.2912
Max. T_{TO} $[kN]$	59.1	59.6
Max. T_{cruise} $[kN]$	20.3	19.3

Comparing the values in Table 4.1 to the relation between thrust and fuel massflow at various conditions in Figure 4.3, it can be verified that the maximum fuel massflow and thrust per engine during the take-off and cruise phases fall in the range that is spanned by the available engine data.

4.1.3. Verification of model convergence

Similar to the work by Onorato et al. [23], who use the *Initiator* aircraft design tool by Elmendorp et al. [88], “feasilisation” of the aircraft concept is sought after. This means that the convergence of the design loop does not include optimisation, but iterations are performed where the outcomes of one iteration are used in the subsequent iteration until the outcomes of subsequent iterations fall below a certain threshold. The threshold for the design loop in this study is set at 0.5% and needs to be met by the relative error of the MTOW, OEW and FW of subsequent iterations. Next to that, to increase the likelihood of a feasible design outcome, the design loop is evaluated for five more iterations when the relative error of the weight components falls below the threshold.

Figure 4.4 shows the progression of the relative error, whereas Figure 4.5 and Figure 4.6 show the convergence of MTOW and OEW, and the fuel weight components, respectively. These and the other figures in this verification section result from an analysis of a 5000 km mission that is flown on hydrogen, but uses kerosene during the reserve and loiter phases of the mission, similar to scenario 2 that will be introduced in Section 5.1.

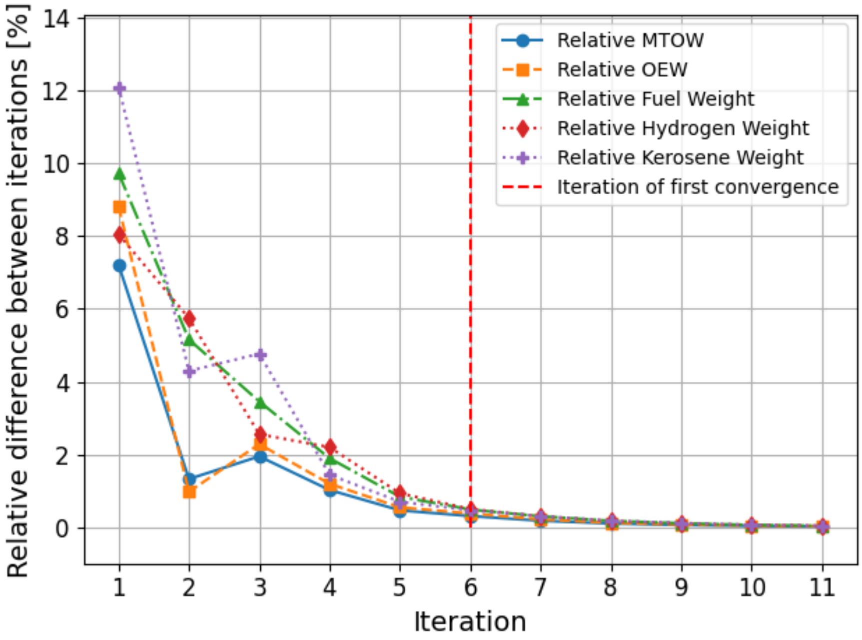

Figure 4.4: Convergence of relative error of MTOW, OEW and FW

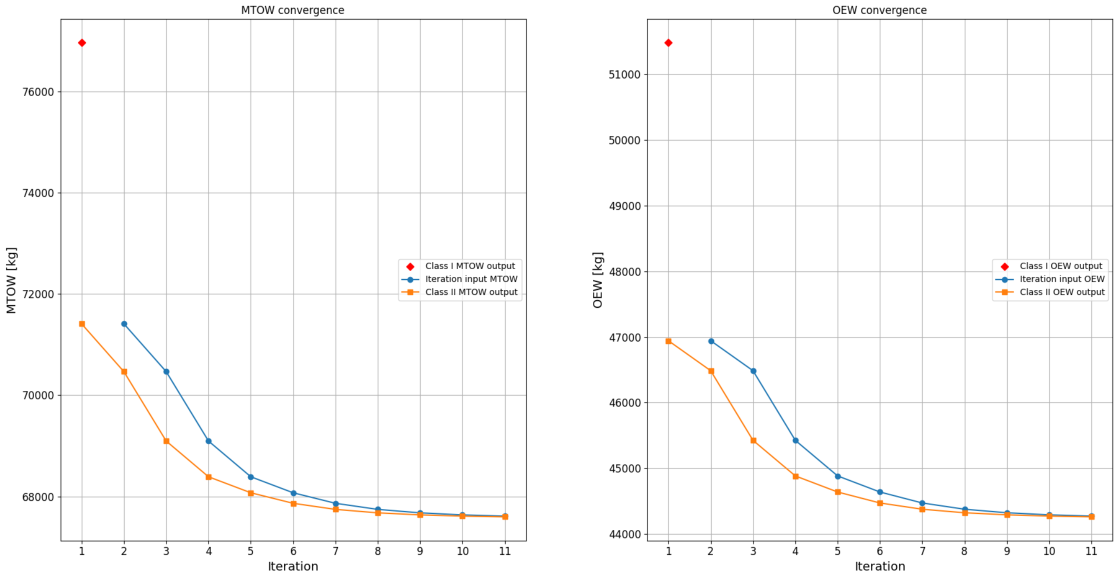

Figure 4.5: Convergence of MTOW and OEW

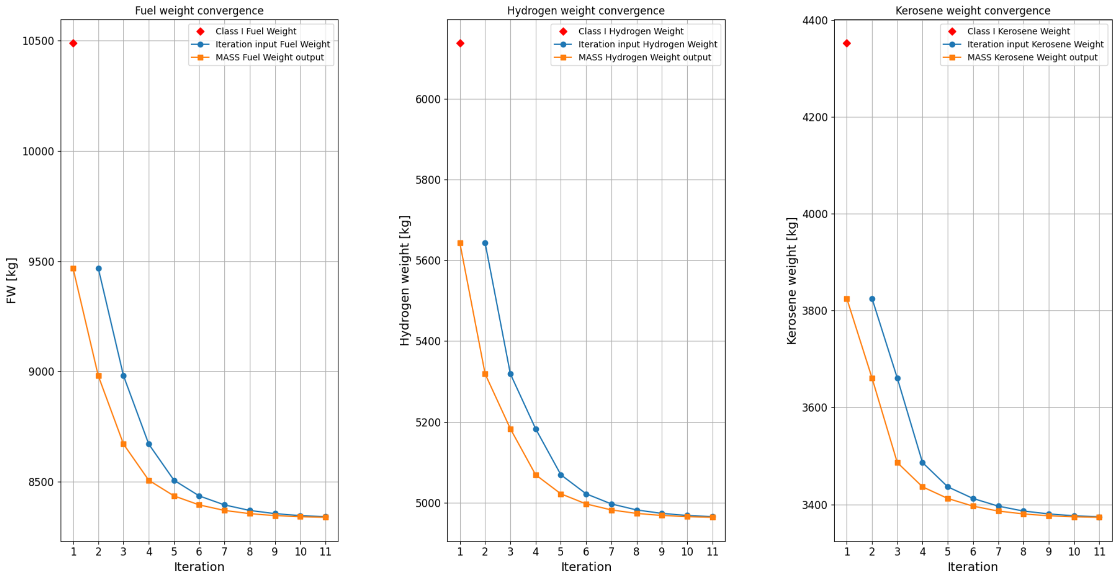

Figure 4.6: Convergence of fuel weight components

As described in Section 3.10, static longitudinal stability of the aircraft is ensured by enlarging the horizontal tail area in case the static margin is too small. Figure 4.7 shows the convergence of the longitudinal positions of the forward and aft C.G., leading edge of the mean aerodynamic chord, and the (corrected) neutral point. It can be observed that the static margin is initially too small, after which the neutral point shifts more aft. Also, the forward and aft C.G. shift more aft. This is caused by the increase in empennage weight caused by the increasing horizontal tail area. The empennage weight increase is reflected in Figure 4.8, which shows the convergence of the weight of components from the Class II weight estimation. Finally, the neutral point and C.G.-range converge to a stable position.

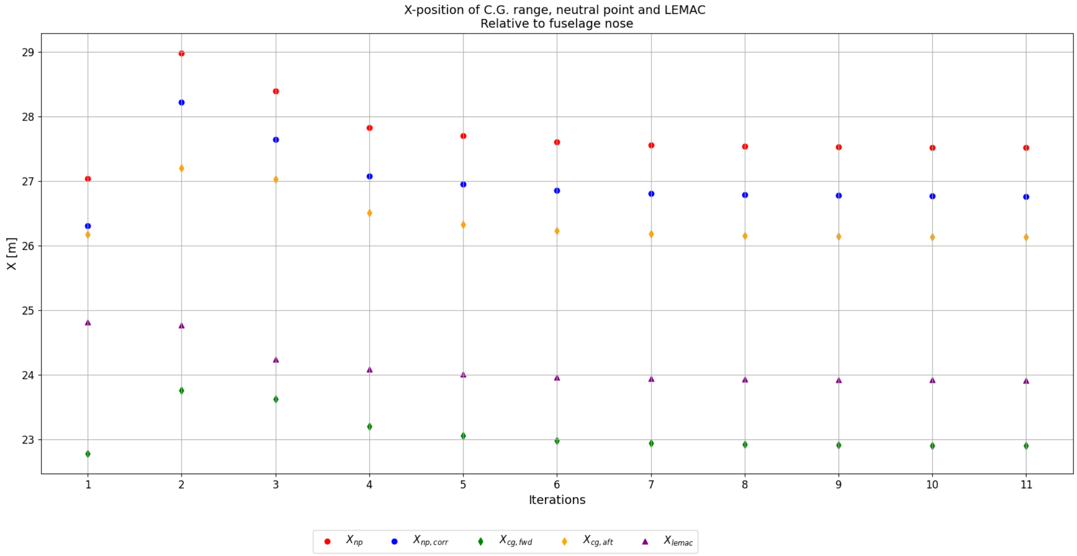

Figure 4.7: Convergence of longitudinal positions

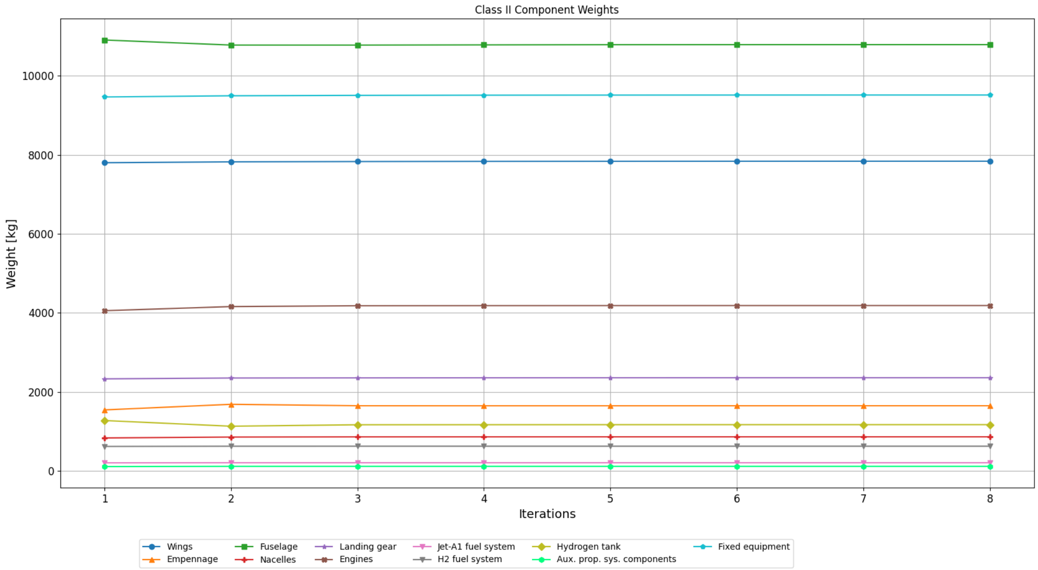

Figure 4.8: Convergence of Class II component weights

4.2. Validation

Validation of the model is done to check if realistic results are obtained from several of the analysis blocks in the design procedure, as well as from the aircraft design model as a whole. First of all, this section will describe the validation of the hydrogen tank model, the aerodynamic model and the engine model in Section 4.2.1, Section 4.2.2 and Section 4.2.3, respectively. Subsequently, Section 4.2.4 will present validation of the outcomes of the entire aircraft design model.

4.2.1. Hydrogen tank model

As the hydrogen tank plays an important role in the dual-fuel aircraft concept. Therefore, it is crucial to validate the sizing of the hydrogen tank. As was described in Section 3.4.2, the insulation layer of the tank is sized for a certain boil-off rate using the method of Tarbah [75]. The boil-off rate is based on a dormancy time of 12 hours. However, when using the same boil-off rate per unit of tank volume as used by Tarbah [75], the thickness of the insulation layer and the the gravimetric efficiency of the tank does not correspond well with values found in literature. Therefore, the boil-off rate used to size the insulation layer is tuned such that it matches data presented by Huete & Pilidis [24]. In their study, they present different tank designs, sized for a certain dormancy time, and present the relation between the tank radius and gravimetric efficiency. Figure 4.9 shows this relation for a $100\ m^3$ cylindrical foam insulation tank with aluminium structural shell, sized for dormancy time of 12 hours. In order to match the relation with the model in this study as accurately as possible, it was found that the boil-off rate from Tarbah [75], normalised by tank volume, had to be scaled down with a factor of 6. Comparing the relations in Figure 4.9, it can be seen that the gravimetric efficiency as estimated by the model in this study overestimates the gravimetric efficiency found by Huete & Pilidis [24] for a tank radius between 1.0 and 1.5 m. At radii above that, the gravimetric efficiency is well estimated. Therefore, the tank model is deemed to have sufficient accuracy for the use in this model, as the tanks generated in this study will have radii between 1.5 and 2.0 m.

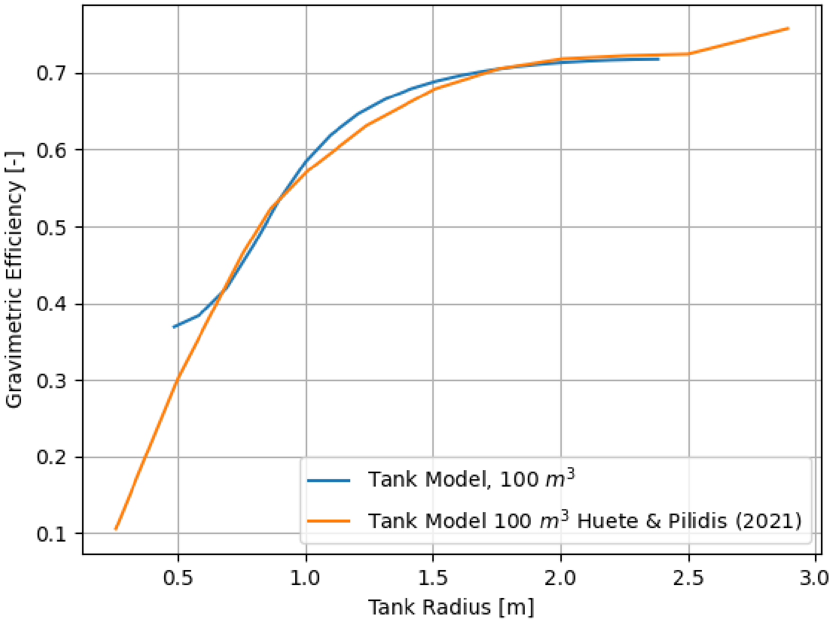

Figure 4.9: Gravimetric efficiency versus tank radius

To further validate the tank model, it was compared to values found in literature. For this, the study by Onorato et al. [23] was used. Results of the comparison can be seen in Table 4.2. For the same tank radius, hydrogen mass and vent pressure, the tank length and shell thickness were found equal. However, a larger insulation thickness was found with the model in this study. This can be attributed to the difference in approach regarding thermal sizing of the insulation layer. Onorato et al. [23] determined the required thickness of the insulation layer by modelling the pressure evolution in the tank in a time-step mission analysis, whereas, in this study, the boil-off rate is assumed constant. The lower tank mass with the insulation layer being thicker can be explained by the difference in tank end cap between the reference case and this model. Onorato et al [23] model the start cap of the tank as a an ellipsoid, for which the shell thickness is equal to the shell thickness of the centre section. In this study, both caps are modelled as hemispheres, for which the thickness of the shell is half of that of the centre section due to reduced stresses. This causes the tank weight the be lower, as the thicker insulation layer barely adds weight.

As mentioned in Section 3.4, tank model in this study uses a vent pressure of 4 bar to estimate the thickness of the structural shell to make a conservative estimate. This leads to a thicker shell thickness and therefore a larger tank mass and lower gravimetric efficiency. However, the gravimetric efficiency is still within 10% difference. In combination with validation of the relation between tank radius and gravimetric efficiency that was previously shown, the tank model in this study is deemed accurate enough for the conceptual design that is done in this study.

Parameter	SMR-LH2a non-integral tank	Tank model output for 2.5 bar vent pressure	Δ (%)	Tank model output for 4 bar vent pressure	Δ (%)
r_{tank} $[m]$	1.86	1.86	-	1.86	-
l_{tank} $[m]$	10.8	10.8	-	10.8	-
$t_{shell,cs}$ $[mm]$	2.5	2.5	-	5.3	+112
t_{ins} $[mm]$	128	146	+14.8	147	+14.8
m_{H2} $[t]$	5.88	5.88	-	5.88	-
m_{tank} $[t]$	1.73	1.58	-8.67	2.44	+41.0
η_{tank} $[-]$	0.773	0.788	+1.94	0.707	-8.54

Table 4.2: Comparison of tank model to tank model data from Onorato et al. [23]

4.2.2. Aerodynamic model

Validation of the aerodynamic model in the design tool is done by comparing existing data from the CSR-01 reference aircraft to the outcomes of the aerodynamic model for that geometry [89]. The CSR-01 is a reference aircraft similar to the A320ceo (current engine option). The CSR-01 data is obtained for 10668 meter altitude (35000 ft), whereas the aerodynamic model was run at 11000 meter. The Mach number was 0.78 in both cases. The results of this comparison can be seen in Table 4.3. In this table, the viscous drag component is similar to the skin friction drag including interference factor that was explained in Section 3.7.2.

Table 4.3: Comparison table of drag components for CSR aircraft geometry. Reference data from [89]

Parameter	CSR-01	Aerodynamic model	Δ (%)
C_L	0.54	0.54	-
C_D	0.03092	0.0315	+1.88
C_{D_i}	0.01106	0.01165	+5.3
C_{D_0}	0.01986	0.01983	-0.15
$C_{D_{visc}}$	0.01884	0.01805	-4.2
C_{D_w}	0.00102	0.001299	+27.4

The induced and viscous drag show correspondence with around 5% difference. The wave drag shows a larger difference. The overestimation may be caused by an incorrect computation of the drag-divergence Mach number in Equation 3.71, as only one Korn-factor for supercritical airfoils is applied to the entire wing. Summing the viscous and wave drag components to the zero-lift drag coefficient C_{D_0}, the aerodynamic model shows good correspondence to the reference data. The total drag coefficient C_D also shows good accuracy compared to the reference data.

Next to the comparison of drag components, the shape of the drag polar was compared to reference data as well. For this, the untrimmed drag polar for the A320neo that was found by Tran [73] was used. To make the comparison, the geometry of the A320neo was mimicked as best as possible, relying on the reference values specified by Tran [73] and Janes[1]. Figure 4.10 shows the drag polar of the aerodynamic model for the A320neo geometry replica compared to the untrimmed drag polar of the A320neo from Tran [73].

---

[1] `https://customer.janes.com/`

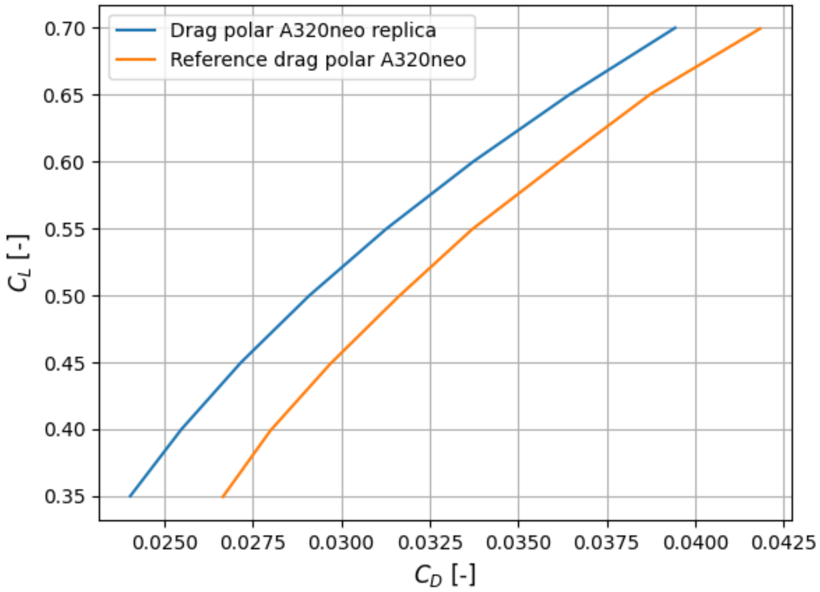

Figure 4.10: Comparison of drag polar from for A320neo geometry from aerodynamic model and reference data from [73]

The comparison shows that the shape of the drag polar aligns well. However, an offset can be noted as well. The drag polar from the aerodynamic model underestimates the reference drag polar with a relative difference of 9.8% at $C_L = 0.35$ and this difference reduces to 5.7% at $C_L = 0.70$. The cause of the underestimation may lie in the fact that the aircraft geometry in this study does not include a kinked section nor a winglet, whereas the aircraft geometry of Tran [73] does include this, leading to larger skin friction drag even for similar wing area.

Considering the comparative analysis of drag components for the CSR aircraft geometry, and the comparison of the drag polar for the A320neo geometry, it is concluded that the aerodynamic model is sufficiently accurate for the conceptual level of this study.

4.2.3. Engine model

Validation of the engine model is done by comparing the thrust specific fuel consumption (TSFC) for both hydrogen and kerosene to values found in literature. For this, the work by Huete et al. [90] will be used. They evaluated the performance of a high-bypass ratio turbofan engine for a wide-body aircraft, similar to the Rolls-Royce Trent XWB, using TURBOMATCH, the gas turbine performance simulation code from Cranfield University. Table 4.4 shows the obtained TSFC of this evaluation at take-off and cruise conditions, compared to the results of the GSP engine model described in Section 3.6 by dividing the fuel flow (g/s) by the thrust (kN). Huete et al. [90] state the conventional fuel in their analysis has a lower fuel calorific value of 43.1 MJ/kg and is therefore considered similar to Jet-A1 fuel in GSP. Additionally, for hydrogen, they differentiate between a value for either the same turbine inlet temperature (TIT) or the same thrust as the Jet-A1 baseline value. As the engine model in this study limits performance by TIT as well, the reference data at this condition is taken from Huete et al. [90]. The TIT limits for take-off and cruise are 1865 K and 1760 K, respectively. As mentioned in Section 3.6, the TIT limit of the engine model in this study is 1765 K. This limit applies to both take-off and cruise conditions. For the own model data, take-off conditions are at a Mach number of 0 and altitude of 0 meter, whereas cruise conditions are at a Mach number of 0.8 and 11000 meter altitude. It is not entirely clear what Mach number and altitude the reference data is obtained at for take-off and cruise conditions.

Table 4.4: TSFC from engine model data compared to data from Huete et al. [90]

Fuel type	**Take-off**			**Cruise**		
	Huete et al.	Own model		Huete et al.	Own model	
	$TSFC\ (g/kN/s)$		Δ (%)	$TSFC\ (g/kN/s)$		Δ (%)
Jet-A1	8.5157	7.5437	-11.4	16.162	15.385	-4.8
H_2	3.2076	2.7675	-13.7	5.8160	5.6134	-3.48

For take-off conditions the TSFC of the model in this study is significantly lower than the reference data. A reason for this could be the fact that the temperature limit of the model by Huete et al. [90] is much higher than the model in this study, as a higher temperature limit allows for a higher fuel flow. For cruise conditions, the TSFC values from the model in this study align with the reference data within a 5% difference. The fact that the TSFC from Huete et al. [90] is higher, can be explained by the fact that the bypass ratio of the engine that their engine model is based on, the Rolls-Royce Trent XWB, is lower than the engine the model in this study is based on, the CFM LEAP-1A. The bypass ratio of the Rolls-Royce Trent XWB is 9.6 [91], whereas the CFM LEAP-1A has a bypass ratio of 11 [92]. Other factors causing differences can lie in the analysis methods in the engine models, the conditions at which data is obtained, or operating principles of engine types as they are both high-bypass ratio turbofans, but for different aircraft categories. However, considering the differences in TSFC at take-off, which is only a small part of the entire mission, and cruise conditions, the engine model in this study was deemed accurate enough for the use in the mission analysis.

4.2.4. Model Validation

As there is currently no existing dual-fuel aircraft operational with which a comparison could be made, validation of the dual-fuel aircraft design tool is done by comparing the results from the design tool to single-fuel equivalents. For this, the work by Onorato et al. [23] is taken as reference. In this work, the integration of hydrogen tanks in tube-and-wing airliners was investigated using (an extended) design framework of the *Initiator* [88]. The SMR-LH2a is a short-to-medium range hydrogen aircraft, similar to an A320neo, with one non-integral tank in the back of the fuselage, whereas the SMR-JA1 is the kerosene equivalent that the SMR-LH2a is compared to by Onorato et al. [23]. The outcomes of the dual-fuel design framework applied to full hydrogen and full kerosene mission specifications are compared to the SMR-LH2a and SMR-JA1 aircraft for similar inputs: 150 passengers, additional cargo of 5050 kg to reach 19.3 tons payload, design range of 4560 km, diversion (reserve) range of 370 km, loiter time of 30 minutes. The results from this comparison can be seen in Table 4.5 and Table 4.6.

Some remarks have to be made regarding this comparison. First of all, Onorato et al. [23] separate the mass of horizontal and vertical tail, whereas the model in this study calculates the empennage weight from geometric aspects of both the horizontal and vertical tailplane. Therefore, for m_{emp} from Onorato, the horizontal and vertical tailplane mass is summed. Next to that, the drag coefficient is displayed in counts, where 1 count equals 0.0001. For the wing, horizontal and vertical tail drag coefficient, the contributions of skin friction drag, including interference factors, and wave drag for these components as described in Section 3.7, are summed. The fuselage drag coefficient reflects the skin friction drag from the fuselage. Finally, the model in this study is set up in such a way that a hydrogen tank is always present in the aircraft concept. As mentioned in Section 3.4.1, the tank will be spherical if the required hydrogen volume is lower as what fits in the hemispherical caps. This makes the comparison with the SMR-JA1 less straightforward.

Table 4.5: Comparison table of full kerosene aircraft to SMR-JA1 by Onorato et al. [23]

Outputs	**SMR-JA1**	**Own model full kerosene**	Δ (%)
l_{fus} $[m]$	36.1	42.2	+16.9
$r_{fus}[m]$	1.99	2.00	+0.50
l_{tank} $[m]$	-	3.58	-
r_{tank} $[m]$	-	1.79	-
S $[m^2]$	122	117	-4.10
b $[m]$	35.8	36	+0.56
S_h/S $[-]$	0.260	0.201	-22.7
m_{H_2} $[t]$	-	0	-
m_{tank} $[t]$	-	0.527	-
η_{tank}	-	-	-
$m_{fuelsys,JetA1}$ $[kg]$	280	275	-1.79
m_{fus} $[t]$	10.6	9.97	-5.94
m_{emp} $[t]$	1.72	1.48	-14.0
m_w $[t]$	9.99	8.17	-18.2
$k_{semidry}$	-	1.006	-
$m_{engines}$ $[t]$	7.66	4.79	-37.5
m_{gear} $[t]$	2.67	2.95	+10.5
W/S $[kN/m^2]$	6.35	6.30	-0.79
T/W $[-]$	0.310	0.304	-1.94
L/D $midcruise$ $[-]$	17.4	18.4	+5.75
$C_{D_{0,vt}}$ $[counts]$	12	16	+33.3
$C_{D_{0,ht}}$ $[counts]$	20	13	-35
$C_{D_{0,fus}}$ $[counts]$	60	77	+28.3
$C_{D_{0,wing}}$ $[counts]$	67	60	-10.4
C_{D_0} $[counts]$	212	189	-10.8
$MTOW$ $[t]$	79.1	75.3	-4.80
OEW $[t]$	44.8	40.2	-10.3
FW $[t]$	15.1	15.8	+4.64

Compared to the SMR-JA1, the fuselage length of the full kerosene aircraft concept is found to be considerably larger. This is mainly caused by the spherical hydrogen tank present in the aircraft. Next to that, the ratio between the horizontal tail and wing area was found to be considerable lower, for which a possible cause is the increase in fuselage length and thereby the lower tail moment arm. Next to that, Onorato et al. [23] use an X-plot to size the horizontal tailplane area, whereas this study estimates the required horizontal tail area for a static margin, relying on semi-empirical neutral point corrections and lift-curve slopes. This (partially) different approach can also explain the discrepancy in the S_h/S-ratio estimation.

Regarding the weight components, it can be seen that lower estimates are found for all components except the the landing gear. The weight of the fuel system is accurately estimated. The difference in fuselage weight is also not large, however the combination of a longer fuselage but a lower weight is not in line with each other. A reason for the underestimation of the fuselage weight could lie in the difference in the estimation method. In this study, the fuselage weight is estimated with semi-empirical relations from Torenbeek [62], as described in Section 3.9, whereas Onorato et al. [23] employ a combination of finite-element methods and semi-empirical relations to obtain more accurate masses. This is also the case for the wing weight, which is estimated to be much lower for the full kerosene concept compared to the SMR-JA1, for which Onorato et al. [23] also (partially) use of finite-element methods. The lower wing area estimated for the full kerosene concept also contributes to a lower wing weight. The $k_{semidry}$ factor for wing weight, as introduced in Section 3.9.1 to correct for (partially) empty wings, is close to 1, which was expected as the full kerosene aircraft still favours the bending relief due to fuel in the wings.

The empennage weight was also found to be considerable lower for the full kerosene concept compared to the SMR-JA1. This can be related to the lower S_h/S-ratio that was found. Also the engine weight was found to be much lower. This can be partially related to the combination of a lower thrust-to-weight ratio and a lower MTOW for the kerosene baseline compared to the SMR-JA1. Furthermore, it is not clear what engine sizing and/or weight estimation method was employed by Onorato et al. [23], and if it perhaps already contains the weight of the nacelle. The difference in landing gear weight can be explained by the fact that Onorato et al. [23] used the method by Raymer [71] for it, whereas the method from Roskam as presented by Torenbeek [62] was used in this study.

Regarding the drag components, large discrepancies can be noted for the C_{D_0} components for the horizontal and vertical tailplanes and fuselage. The lower horizontal tailplane drag can be related to the lower horizontal tailplane area, and the higher fuselage drag can be related to the higher horizontal tailplane area. It is unknown what vertical tailplane area was found for the SMR-JA1, so that cannot be used to explain the discrepancy in drag for the vertical tailplane. Next to that, it is not known in great detail what drag build-up methods were used by Onorato et al. [23], as well as the conditions at which the drag components are evaluated. Therefore, it is difficult to point out other causes for the large discrepancies in these drag components The wing drag is also estimated lower for the the full kerosene concept, but not with such a large difference as the other components, and it can be related to the lower wing area. Finally, the total C_{D_0} drag coefficient is estimated little over 10% lower for the full kerosene concept, which can be partially explained by the combination of the individual drag components and is therefore deemed reasonably accurate.

Regarding the total weights, it can be noted that both the MTOW and FW are estimated within 5% accuracy. The lower estimate for the OEW can be explained by the lower weight component estimates previously mentioned. Table 4.6 below shows the comparison of the full hydrogen concept from this study with the SMR-LH2a concept from Onorato et al. [23].

Table 4.6: Comparison table of full hydrogen aircraft to SMR-LH2a by Onorato et al. [23]

Outputs	**SMR-LH2a**	**Own model full hydrogen**	Δ (%)
l_{fus} $[m]$	47.5	50.8	+6.95
$r_{fus}[m]$	1.99	2.00	+0.50
l_{tank} $[m]$	10.8	11.8	+9.26
r_{tank} $[m]$	1.86	1.82	-2.15
S $[m^2]$	130	115	-11.5
b $[m]$	36.9	36	-2.44
S_h/S $[-]$	0.385	0.266	-30.9
m_{H_2} $[t]$	5.88	6.16	+4.76
m_{tank} $[t]$	1.73	2.57	+48.6
η_{tank}	0.773	0.706	-8.67
$m_{fuelsys,H2}$ $[kg]$	753	763	+1.33
m_{fus} $[t]$	13.7	14.1	+2.92
m_{emp} $[t]$	2.48	1.67	-32.7
m_w $[t]$	10.4	9.26	-11.0
$k_{semidry}$	-	1.035	-
$m_{engines}$ $[t]$	7.00	5.01	-28.4

Continued on next page

Table 4.6 – *continued from previous page*

Outputs	**SMR-LH2a**	**Own model full hydrogen**	Δ (%)
m_{gear} $[t]$	3.20	2.91	-9.06
W/S $[kN/m^2]$	5.79	6.33	+9.33
T/W $[-]$	0.293	0.325	+10.9
L/D $midcruise$ $[-]$	16.4	17.9	+9.15
$C_{D_{0,vt}}$ $[counts]$	10	13	+30.0
$C_{D_{0,ht}}$ $[counts]$	29	18	-37.9
$C_{D_{0,fus}}$ $[counts]$	73	92	+26.0
$C_{D_{0,wing}}$ $[counts]$	68	60	-11.8
C_{D_0} $[counts]$	234	209	-10.7
$MTOW$ $[t]$	76.6	74.4	-2.87
OEW $[t]$	51.4	48.9	-4.86
FW $[t]$	5.88	6.16	+4.76

Comparing the full hydrogen concept to the SMR-LH2a, it can be seen that the estimated fuselage length is larger, but within reasonable accuracy of 10%. This is caused by a longer hydrogen tank, which can be related to the larger hydrogen mass required. The required wing area is found to be lower, which can be related to the combination of a lower MTOW and a higher wing loading W/S. Similar to the previous comparison of the full kerosene concept to the SMR-JA1, the ratio between horizontal tailplane and wing area was found to be considerably lower for the full hydrogen concept compared to the SMR-LH2a.

As was previously mentioned in Section 4.2.1, the tank model in this study overestimates the tank mass compared to the model used by Onorato et al. [23] and therefore the gravimetric efficiency is lower. Looking further at the estimated weights of components, it can be seen that the weight of the hydrogen fuel system and the fuselage are well estimated. The empennage weight is again found to be much lower, and can be related to the lower horizontal tailplane area. Next to that, the wing weight is found to be lower for the full hydrogen concept compared the SMR-LH2a, which can be related to the lower wing area. The correction factor for semi-dry wings, $k_{semidry}$, now is 1.035, which is expected for a full hydrogen concept. The engine weight is again found to be considerable lower, even though the thrust loading T/W was estimated to be around 10% larger.

Regarding the drag components, similar discrepancies can be found as for the full kerosene comparison. Again the total C_{D_0} component is estimated reasonably accurate at around 10%.

Finally, looking at the total weight components, it can be seen that the hydrogen fuel weight is estimated within 5% accuracy. This is also the case for the OEW, for which the lower estimate can again be related to some lower component weight estimates. Combined, the MTOW is estimated within 3% accuracy.

Conclusions from model validation

From the comparison of the full kerosene and full hydrogen concepts to the SMR-JA1 and SMR-LH2a from the work by Onorato et al. [23], respectively, several things can be concluded.

First of all, the estimation of the aircraft geometry was reasonably accurate for the fuselage length and wing area. However, a large discrepancies are found in the estimation of the horizontal tailplane area. Also, the individual drag components for the horizontal and vertical tailplanes, and the fuselage showed large discrepancies. However, the total drag coefficient was estimated with reasonable accuracy.

Next to that, the accuracy of the estimation of component weights varied from high for the fuel systems, to reasonable for the fuselage, wing and landing gear, to low for the empennage and engine weights.

Finally, the fuel weight of both hydrogen and kerosene was estimated with good accuracy (within 5%). This is also the case for the MTOW and OEW. Therefore, the aircraft design model in this study is deemed accurate enough for the conceptual level that this study is performed at.

5

Results & Discussion

The objective of this study was to investigate the effect of implementing a dual-fuel propulsion system on the design of an narrowbody turbofan-powered tube and wing aircraft. The design procedure previously outlined can be used to evaluate these effects by comparing aircraft concepts with varying fuel splits between hydrogen and kerosene. Next to that, aircraft concepts with varying TLARs in terms of range and payload are compared to see if applying the dual-fuel propulsion concept affects the aircraft design differently in those cases. Finally, sensitivity analyses are performed to obtain more insight in the effect of small deviations in fuel splits and TLARs.

5.1. Comparative Analysis

In this section, the comparison between aircraft concepts based on different scenarios is presented. The scenarios are meant to distinguish between different potential use cases of a dual-fuel aircraft. They are described below. Furthermore, the comparison will be done for two different range requirements. The other TLARs are kept the same, and can be seen in Table 5.1. First of all, the range of the Airbus A320 is used, as this aircraft is currently one of the most widely operated narrowbody turbofan-powered aircraft. This range is 5000 km (2700 nm)[1]. Secondly, it was mentioned in Chapter 2 that 50% of cumulative CO_2 emissions is caused by flights up to 2500 km, for a large part operated by narrowbody aircraft like the A320. Therefore, a range of 2500 km is used to compare the scenarios as well.

Table 5.1: Top-Level Aircraft Requirements for the Dual-Fuel Aircraft

Parameter	Value	Unit
Number of passengers (PAX)	150	-
Additional cargo	750	kg
Cruise altitude	11000	m
Cruise Mach number	0.78	-
Loiter time	0.5	hour
Reserve range	370	km

Baseline kerosene version

To perform a comparative analysis, the design tool is used to make a baseline version that is operating solely on kerosene. As mentioned before in Section 4.2.4, the aircraft design tool developed in this study is set up in such a way that a hydrogen tank is always present. Therefore, the kerosene baseline aircraft contains a spherical hydrogen tank. This means that for the kerosene baseline aircraft, OEW will be overestimated due to the tank weight and longer fuselage resulting in higher fuselage weight. Next to that, a longer fuselage causes more friction drag, resulting in an overestimation of fuel weight. Although difficult to exactly quantify, it is expected that the total error that the empty hydrogen tank causes will be limited. It will be shown later that the empty hydrogen tank contributes to the OEW of

---

[1] `https://skybrary.aero/aircraft-family/a320-family`

the kerosene baseline version only to limited extent. A side view of the kerosene baseline from the ParaPy model is shown below in Figure 5.1.

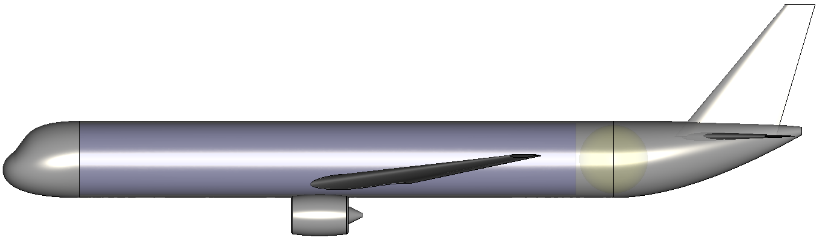

Figure 5.1: Side view of kerosene baseline version from ParaPy model

Scenario 1: Maximise hydrogen use
The first scenario that is used in the comparative analysis is for when hydrogen is used throughout the whole mission. This scenario is evaluated to investigate the impact of shifting from the kerosene baseline to full hydrogen.

Scenario 2: Reserve on kerosene
The second scenario is similar to the first scenario, but in this case, kerosene is used for the reserve phase of the mission. As most flights are uneventful, the fuel that needs to be taken on board for reserve, often remains unused. This scenario is evaluated to investigate how the aircraft design concept differs when the hydrogen tank does not need to be sized for reserve fuel as well. In this study, the 'reserve phase' consists of flying both the reserve range, as well as the loiter time as specified in Table 5.1. This can also be seen in Figure 5.2, which shows the mission profile for this scenario.

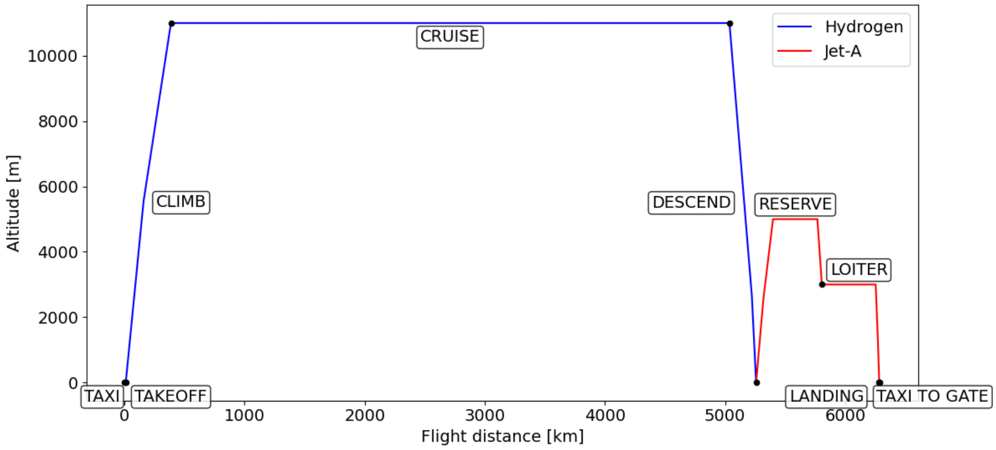

Figure 5.2: Mission profile for scenario 2: reserve on kerosene

Scenario 3 & 4: 50/50 fuel use, varying priority
In scenario 3 and 4, only one fuel split is applied during the mission. This happens at 50% of the cruise phase. For scenario 3, hydrogen will be used for the first part of the mission until the fuel split at 50% of the cruise phase and kerosene will be used for the remainder of the mission. For scenario 4, the fuel use is the other way around. These scenarios are evaluated to investigate if an effect can be noted from using either one of the fuels first. As the energy density of the fuels are very different, a different fuel weight progression could occur. Next to that, evaluating these scenarios at 5000 km reflects to some extent the use of the aircraft concept for a 2000-2500 km return flight for which fuel is already taken on board for both legs. Figure 5.3 and Figure 5.4 show the mission profiles that are evaluated for scenario 3 and 4, respectively.

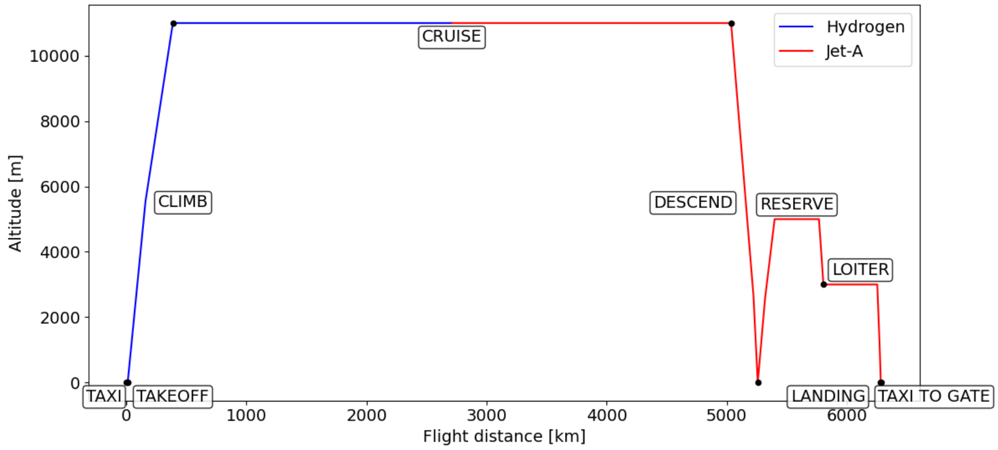

Figure 5.3: Mission profile for scenario 3: 50/50, hydrogen first

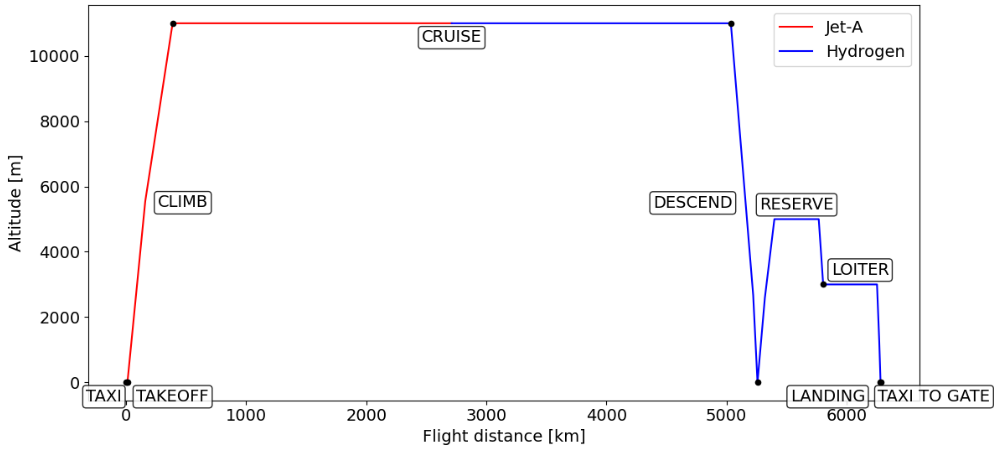

Figure 5.4: Mission profile for scenario 4: 50/50, kerosene first

For all scenarios, no fuel switch is applied during the take-off, climb and approach phases, due to potential safety implications. However, for scenario 2, where the fuel switch is applied after the missed approach at the start of the reserve phase, an exemption is made in order to simplify the analysis. Finally, the number of fuel switches is preferably minimised to limit the risk related to switching fuels in-flight.

5.1.1. Scenario comparison at 5000 km range

Table 5.2 shows the results from evaluating the different scenarios for a range of 5000 km. In this table, aircraft geometric parameters are shown, as well as performance parameters, fuel and tank weight components and total weights. Finally, also the specific energy consumption and equivalent CO_2 emissions are shown. As described in Section 3.11, these are separated into well-to-tank (WTT) and tank-to-wake (TTW) contributions, together forming the well-to-wake (WTW) SEC and CO_2eq. The table shows the separate contributions of hydrogen and kerosene as well as the combinations for the mission including the reserve phase. For the tank-to-wake specific energy consumption, the specific energy consumption is also hydrogen and kerosene combined is also shown for the mission phase without the reserve phase. These values were obtained by subtracting the energy contained in the amount of kerosene needed for the scenario were kerosene is used for the reserve phase from the total energy of the whole mission, and scaling down using the ratio between the flight distance ex- and including the reserve phase. Although this is not entirely accurate for the scenarios where the reserve phase is flown on hydrogen, it is expected that the energy consumed from either hydrogen kerosene during the reserve phase is of similar order of magnitude. Next to that, the weight of this reserve fuel is only a small part of the weight carried during the reserve phase (OEW, payload and reserve fuel) and therefore this approximation of reserve energy is deemed accurate enough. For the equivalent CO_2 emissions, only the entire mission including the reserve phase is considered.

Below the results table, Table 5.3 shows the relative differences of the parameters for each scenario compared to the baseline kerosene version. For the parameters related to hydrogen use, there is no relative difference compared to the kerosene baseline. Therefore, in order to get more insight into the change of parameters across the scenarios where hydrogen is involved, the relative differences of scenarios 2, 3 and 4 are also shown with respect to the full hydrogen case in Table 5.4.

Following the tables with results, the results from the comparative analysis will be elaborated upon per scenario, for which also the breakdown of MTOW and OEW for each scenario at 5000 km range is presented using pie-charts.

Table 5.2: Results from evaluating scenarios at 5000 km range

Outputs	**Baseline kerosene**	**Full Hydrogen**	**Reserve on kerosene**	**50/50, hydrogen first**	**50/50, kerosene first**
		Configuration Outputs			
l_{fus} $[m]$	42.2	51.0	48.6	44.8	45.4
l_{tank} $[m]$	3.58	11.97	9.76	6.07	6.70
S $[m^2]$	127.2	123.8	121.3	118.9	122.7
A $[-]$	10.2	10.5	10.7	10.9	10.6
S_h $[m^2]$	28.6	33.5	30.9	24.8	27.2
S_v $[m^2]$	23.4	18.9	19.4	20.7	21.2
S_h/S $[-]$	0.225	0.270	0.255	0.209	0.222
W/S $[N/m^2]$	5307	5376	5468	5482	5320
T/W $[-]$	0.289	0.324	0.311	0.292	0.297
T_{TO} $[kN]$	195	251	206	190	194
$L/D_{midcruise}$ $[-]$	17.2	16.8	17.2	17.8	17.0
C_{D_0} $[counts]$	182	201	198	189	189
m_{JetA} $[t]$	16.3	0	3.37	8.77	7.65
m_{H_2} $[t]$	–	6.28	4.96	2.70	3.13
m_{tank} $[t]$	0.527	2.61	2.10	1.22	1.39
η_{tank}	–	0.708	0.706	0.688	0.693
$MTOW$ $[t]$	68.9	67.8	67.6	66.4	66.6
OEW $[t]$	37.6	46.6	44.3	40.0	40.8
FW $[t]$[2]	16.3	6.28	8.34	11.5	10.8
		Performance output: SEC $[MJ/PAX/km]$ of mission including reserve phase			
TTW_{H_2+JetA}[3] of mission only, without reserve phase	0.741	0.807	0.790	0.739	0.745
TTW_{H_2+JetA}	0.773	0.828	0.814	0.771	0.776
TTW_{H_2}	–	0.828	0.654	0.355	0.413

Continued on next page

---

[2] FW is the sum of m_{JetA} and m_{H_2}. Results may slightly differ due to rounding.

[3] Reserve energy is approximated for all scenarios using m_{JetA} from the ‘Reserve on kerosene’-scenario at 5000 km range

Table 5.2 – *continued from previous page*

Outputs	**Baseline kerosene**	**Full Hydrogen**	**Reserve on kerosene**	**50/50, hydrogen first**	**50/50, kerosene first**
TTW_{JetA}	0.773	–	0.160	0.416	0.363
$WTT_{H_2,2025}$	–	0.517	0.409	0.222	0.258
$WTT_{H_2,2035}$	–	0.480	0.379	0.206	0.239
$WTT_{H_2,2050}$	–	0.474	0.375	0.204	0.237
$WTW_{H_2+JetA,2025}$	0.773	1.35	1.22	0.993	1.034
$WTW_{H_2+JetA,2035}$	0.773	1.31	1.19	0.977	1.015
$WTW_{H_2+JetA,2050}$	0.773	1.30	1.19	0.975	1.012
Performance output: CO_2eq $[g/PAX/km]$ of mission including reserve phase					
$TTW_{H_2+JetA,2025}$	81.9	95.2	92.2	85.0	86.0
$TTW_{H_2+JetA,2035}$	81.9	75.4	76.5	76.4	76.1
$TTW_{H_2+JetA,2050}$	81.9	46.5	53.7	64.0	61.7
$TTW_{H_2,2025}$	–	95.2	75.2	40.9	47.5
$TTW_{H_2,2035}$	–	75.4	59.5	32.3	37.6
$TTW_{H_2,2050}$	–	46.5	36.7	19.9	23.2
TTW_{JetA}	81.9	–	17.0	44.1	38.5
$WTT_{H_2,2025}$	–	59.5	47.0	25.5	29.7
$WTT_{H_2,2035}$	–	43.6	34.5	18.7	21.8
$WTT_{H_2,2050}$	–	26.6	21.0	11.4	13.3
$WTW_{H_2+JetA,2025}$	81.9	155	139	111	116
$WTW_{H_2+JetA,2035}$	81.9	119	111	95.2	97.8
$WTW_{H_2+JetA,2050}$	81.9	73.1	74.7	75.5	74.9

Table 5.3: Relative difference of parameters from different scenarios compared to full kerosene baseline for 5000 km

Outputs	**Full Hydrogen** Δ (%)	**Reserve on kerosene** Δ (%)	**50/50, hydrogen first** Δ (%)	**50/50, kerosene first** Δ (%)
Configuration Outputs				
l_{fus} (%)	+21	+15	+6	+8
l_{tank} (%)	+235	+173	+70	+87
S (%)	-3	-5	-7	-4
A (%)	+3	+5	+7	+4
S_h (%)	+17	+8	-13	-5
S_v (%)	-19	-17	-12	-10
S_h/S (%)	+20	+13	-7	-2
W/S (%)	+1	+3	+3	0
T/W (%)	+12	+7	+1	+3
T_{TO} (%)	+10	+5	-3	-1
$L/D_{midcruise}$ (%)	-2	0	+4	-1
C_{D_0} (%)	+10	+8	+4	+4
m_{JetA} (%)	–	-79	-46	-53

Continued on next page

Table 5.3 – *continued from previous page*

Outputs	**Full Hydrogen** Δ %	**Reserve on kerosene** Δ %	**50/50, hydrogen first** Δ %	**50/50, kerosene first** Δ %
m_{H_2} (%)	–	–	–	–
m_{tank} (%)	+396	+299	+132	+163
η_{tank} (%)	–	–	–	–
$MTOW$ (%)	-1	-2	-4	-3
OEW (%)	+24	+18	+6	+9
FW (%)	-61	-49	-30	-34
Performance output: SEC (%) of mission including reserve phase				
TTW_{H_2+JetA} (%) of mission only, without reserve phase	+9	+7	0	+1
TTW_{H_2+JetA} (%)	+7	+5	0	0
TTW_{H_2} (%)	–	–	–	–
TTW_{JetA} (%)	–	-79	-46	-53
$WTT_{H_2,2025}$ (%)	–	–	–	–
$WTT_{H_2,2035}$ (%)	–	–	–	–
$WTT_{H_2,2050}$ (%)	–	–	–	–
$WTW_{H_2+JetA,2025}$ (%)	+74	+58	+29	+34
$WTW_{H_2+JetA,2035}$ (%)	+69	+54	+26	+31
$WTW_{H_2+JetA,2050}$ (%)	+69	+54	+26	+31
Performance output: CO_2eq (%) of mission including reserve phase				
$TTW_{H_2+JetA,2025}$ (%)	+16	+13	+4	+5
$TTW_{H_2+JetA,2035}$ (%)	-8	-7	-7	-7
$TTW_{H_2+JetA,2050}$ (%)	-43	-34	-22	-25
$TTW_{H_2,2025}$ (%)	–	–	–	–
$TTW_{H_2,2035}$ (%)	–	–	–	–
$TTW_{H_2,2050}$ (%)	–	–	–	–
TTW_{JetA} (%)	–	-79	-46	-53
$WTT_{H_2,2025}$ (%)	–	–	–	–
$WTT_{H_2,2035}$ (%)	–	–	–	–
$WTT_{H_2,2050}$ (%)	–	–	–	–
$WTW_{H_2+JetA,2025}$ (%)	+89	+70	+35	+41
$WTW_{H_2+JetA,2035}$ (%)	+45	+36	+16	+19
$WTW_{H_2+JetA,2050}$ (%)	-11	-9	-8	-9

Comparing the different scenarios to the kerosene baseline, several observations can be made. First of all, a large increase in fuselage length is noted for the first two scenarios in which all or most of the mission is flown on hydrogen. This is caused by a large increase in hydrogen weight and therefore of tank length. For the 50/50 scenarios, the fuselage length increase is limited.

Next to that, the total fuel weight shows a large decrease, as the increase in hydrogen weight is accompanied by a large reduction in kerosene weight. When flying the reserve part of the mission on kerosene, the kerosene weight is decreased by almost 80%, whereas for the 50/50 scenarios, around half of the kerosene weight is reduced. However, the increase in hydrogen weight causes the OEW to increase significantly due to the increasing weight of the hydrogen tank and the fuselage. As a result, MTOW shows a slight decrease with increasing hydrogen use, but stays almost the same.

As mentioned before, the two 50/50 scenarios were evaluated to investigate if a fuel weight advantage would be gained if the heavier kerosene would be used first. Comparing the combined fuel weight, a decrease is indeed observed for the kerosene first case. However, the increase in OEW caused by the increase in hydrogen tank weight results in the MTOW to be slightly larger when kerosene is used first than when hydrogen is used first.

Regarding the specific energy consumption, it can be noted that the TTW combined contribution of hydrogen and kerosene of the 50/50 scenarios stays almost the same compared to the kerosene baseline. For the full hydrogen and reserve on kerosene scenarios the TTW specific energy consumption increases compared to full kerosene, but by a smaller amount than the 50/50 scenarios.

It can also be observed that increasing hydrogen causes the WTW specific energy consumption to increase significantly. Next to the increase in TTW energy consumption, this can be mainly attributed to the fact that the WTT energy consumption of hydrogen is large.

Following the WTW SEC increase, it can also be observed that the equivalent WTW CO_2 emissions increase significantly with increasing hydrogen use for the years 2025 and 2035 compared to the kerosene baseline version. As was described in Section 3.11, the equivalent CO_2 emissions of hydrogen is related to the carbon intensity of the grid electricity the hydrogen is produced with. For 2025 and 2035, this carbon intensity is such that the combination of the WTT and TTW equivalent CO_2 emissions exceed the WTW emissions for the kerosene baseline. Only for the year 2050, this carbon intensity has reduced enough such that the WTW emissions of the aircraft concepts (partially) on hydrogen are lower than the kerosene baseline. Table 5.4 below shows the relative difference of the second, third and fourth scenarios compared to the full hydrogen concept.

Table 5.4: Relative difference of parameters from different scenarios compared to full hydrogen for 5000 km

Outputs	**Reserve on kerosene** Δ (%)	**50/50, hydrogen first** Δ (%)	**50/50, kerosene first** Δ (%)
	Configuration Outputs		
l_{fus} (%)	-5	-12	-11
l_{tank} (%)	-18	-49	-44
S (%)	-2	-4	-1
A (%)	+2	+4	+1
S_h (%)	-8	-26	-19
S_v (%)	+3	+9	+12
S_h/S (%)	-6	-23	-18
W/S (%)	+2	+2	-1
T/W (%)	-4	-10	-8
T_{TO} (%)	-4	-12	-10
$L/D_{midcruise}$ (%)	+2	+6	+1
C_{D_0} (%)	-2	-6	-6
m_{JetA} (%)	–	–	–
m_{H_2} (%)	-21	-57	-50
m_{tank} (%)	-20	-53	-47
η_{tank} (%)	0	-3	-2
$MTOW$ (%)	0	-2	-2
OEW (%)	-5	-14	-12

Continued on next page

Table 5.4 – *continued from previous page*

Outputs	**Reserve on kerosene** Δ %	**50/50, hydrogen first** Δ %	**50/50, kerosene first** Δ %
FW (%)	+33	+82	+72
Performance output: SEC (%) of mission including reserve phase			
TTW_{H_2+JetA} (%) of mission only, without reserve phase	-2	-8	-8
TTW_{H_2+JetA} (%)	-2	-7	-6
TTW_{H_2} (%)	-21	-57	-50
TTW_{JetA} (%)	–	–	–
$WTT_{H_2,2025}$ (%)	-21	-57	-50
$WTT_{H_2,2035}$ (%)	-21	-57	-50
$WTT_{H_2,2050}$ (%)	-21	-57	-50
$WTW_{H_2+JetA,2025}$ (%)	-9	-26	-23
$WTW_{H_2+JetA,2035}$ (%)	-9	-25	-22
$WTW_{H_2+JetA,2050}$ (%)	-9	-25	-22
Performance output: CO_2eq (%) of mission including reserve phase			
$TTW_{H_2+JetA,2025}$ (%)	-3	-11	-10
$TTW_{H_2+JetA,2035}$ (%)	+2	+1	+1
$TTW_{H_2+JetA,2050}$ (%)	+15	+38	+33
$TTW_{H_2,2025}$ (%)	-21	-57	-50
$TTW_{H_2,2035}$ (%)	-21	-57	-50
$TTW_{H_2,2050}$ (%)	-21	-57	-50
TTW_{JetA} (%)	–	–	–
$WTT_{H_2,2025}$ (%)	-21	-57	-50
$WTT_{H_2,2035}$ (%)	-21	-57	-50
$WTT_{H_2,2050}$ (%)	-21	-57	-50
$WTW_{H_2+JetA,2025}$ (%)	-10	-29	-25
$WTW_{H_2+JetA,2035}$ (%)	-7	-20	-18
$WTW_{H_2+JetA,2050}$ (%)	+2	+3	+3

Comparing the scenarios partially flown on hydrogen to the full hydrogen case, it can be observed that the hydrogen weight is reduced significantly, thereby also reducing the tank length and the length of the fuselage.

It can also be observed that the reduced use of hydrogen causes reductions in specific energy consumption for all three years, and equivalent CO_2 emissions for 2025 and 2035. The similarities among the reductions in SEC and WTT and TTW CO_2eq is caused by only small improvements in the efficiency of hydrogen electrolysis and energy required for hydrogen liquefaction from 2025 to 2035 and 2050, as was shown in Table 3.4. In Section 5.1.2 below, weight breakdowns of the kerosene baseline and the aircraft concepts for each scenario at 5000 km range are presented.

5.1.2. Scenarios weight breakdown: 5000 km

In the pie-charts below, the breakdown of MTOW and OEW is shown for the kerosene baseline and each scenario.

Weight breakdown kerosene baseline

For the kerosene baseline, the MTOW breakdown in Figure 5.5 shows that little over half of MTOW is dedicated to OEW, whereas payload and Jet-A1 split the remainder fairly equally, with Jet-A1 taking up a bit more of the weight. Regarding the OEW breakdown in Figure 5.6, it can be seen that the fuselage takes up little over a quarter of the OEW and the wings account for 20% of the OEW. The empty hydrogen tank only accounts for 1.4% of the OEW, so the presence of this empty tank in the kerosene baseline is not affecting the weight much.

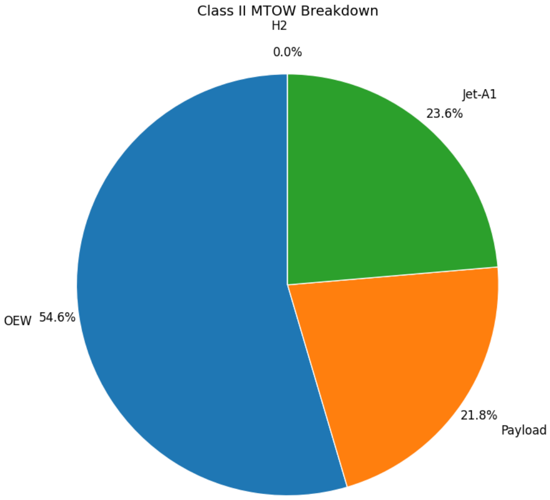

Figure 5.5: MTOW breakdown kerosene baseline at 5000 km range

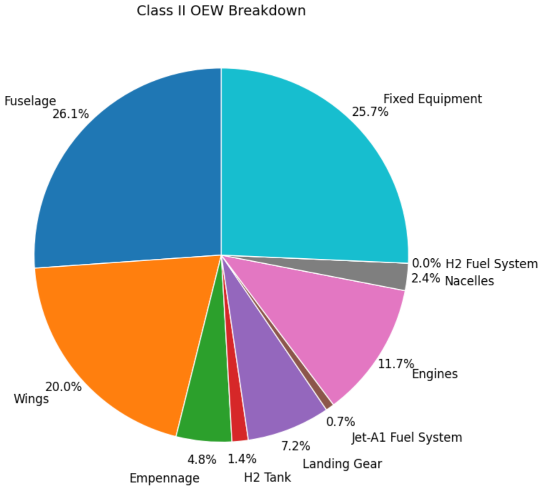

Figure 5.6: OEW breakdown kerosene baseline at 5000 km range

Scenario 1: Full hydrogen

As was mentioned before, the OEW increases significantly for increasing hydrogen use, whereas the fuel weight decreases drastically. This is reflected by the MTOW breakdown of full hydrogen in Figure 5.7 below. The OEW now takes up almost 70% of the MTOW, whereas the fuel weight (hydrogen) takes up only little less than 10%. The increase in OEW can be largely attributed to the increase in fuselage weight and hydrogen tank weight, as can be seen in Figure 5.8.

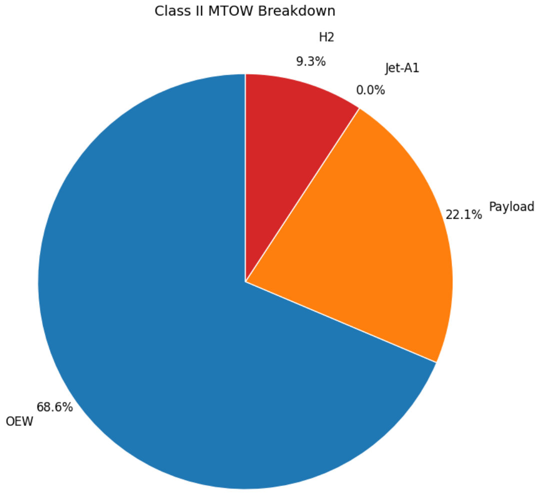

Figure 5.7: MTOW breakdown full hydrogen at 5000 km range

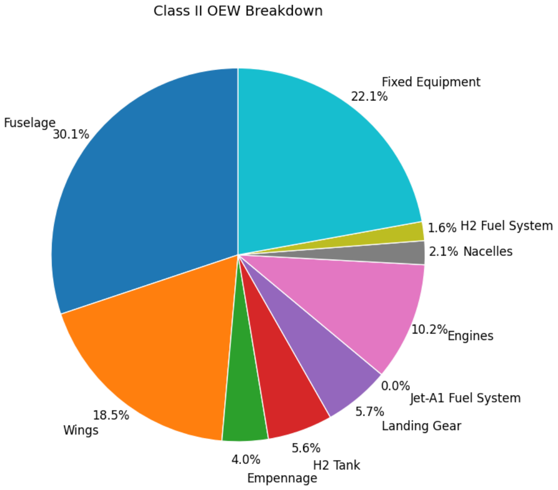

Figure 5.8: OEW breakdown full hydrogen at 5000 km range

Scenario 2: Reserve on kerosene

For the aircraft concept where the reserve is flown on kerosene, Figure 5.9 shows the OEW still takes up a large part of the MTOW. However, compared to full hydrogen, it is decreased slightly due to the increase in total fuel weight. As shown in Figure 5.10, the contribution of the fuselage and hydrogen tank weight is also reduced slightly compared to the full hydrogen scenario.

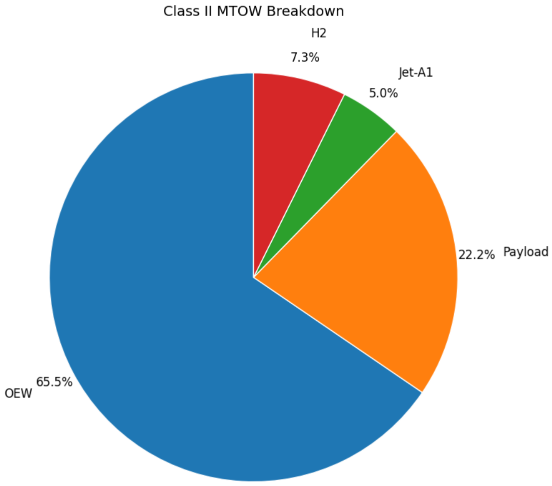

Figure 5.9: MTOW breakdown reserve on kerosene at 5000 km range

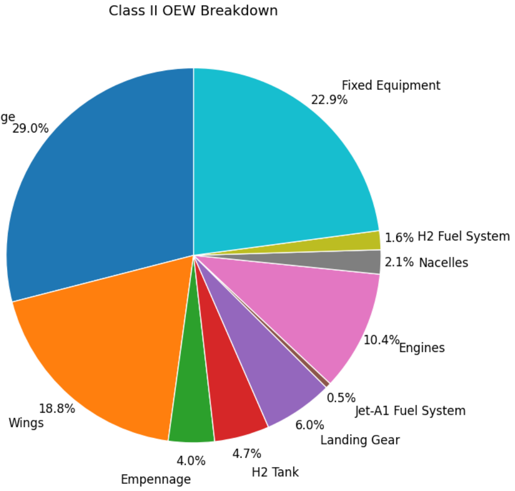

Figure 5.10: OEW breakdown reserve on kerosene at 5000 km range

Scenario 3: 50/50 cruise hydrogen first

For the 50/50 scenario where hydrogen is used first, the kerosene weight is larger than for scenario 2, causing a further decrease in the contribution of the OEW to the MTOW, as can be observed in Figure 5.11. Also, the contribution of the hydrogen weight is lower compared to scenario 2. This results in a lower hydrogen tank weight, and with that a lower fuselage weight contribution to the OEW, as can be seen in Figure 5.22.

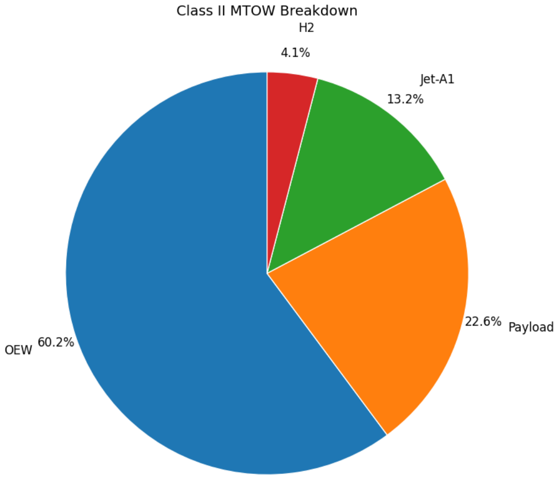

Figure 5.11: MTOW breakdown 50/50 fuel split cruise, hydrogen first at 5000 km range

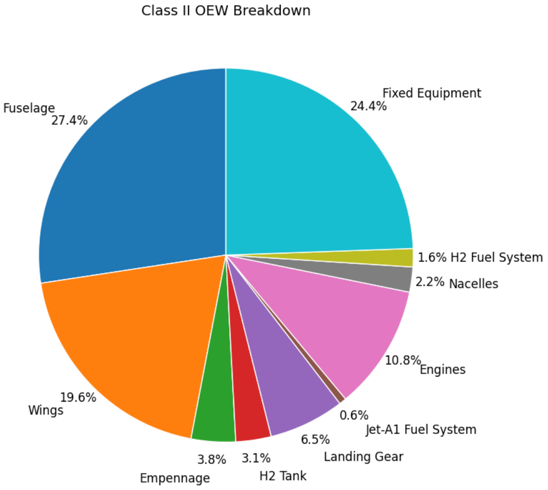

Figure 5.12: OEW breakdown 50/50 fuel split cruise, hydrogen first at 5000 km range

Scenario 4: 50/50 cruise kerosene first

For the 50/50 scenario where kerosene is used first, Figure 5.13 shows a very similar MTOW breakdown compared to scenario 3. The hydrogen weight contribution is increased slightly, causing an increase in OEW due to a slightly larger hydrogen tank and fuselage weight contribution to the OEW, as seen in Figure 5.14.

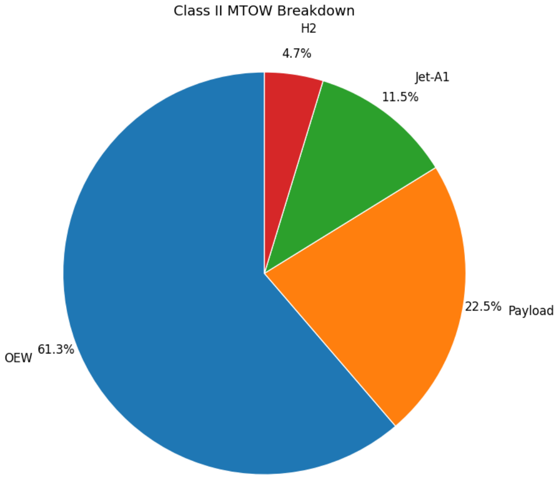

Figure 5.13: MTOW breakdown 50/50 fuel split cruise, kerosene first at 5000 km range

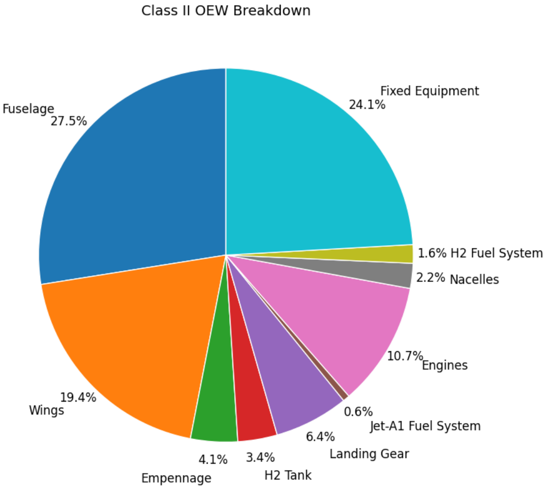

Figure 5.14: OEW breakdown 50/50 fuel split cruise, kerosene first at 5000 km range

5.1.3. Scenario comparison at 2500 km range

Similar to the comparative analysis at 5000 km range, Table 5.5 presents the outcomes of the scenarios at a range of 2500 km, Table 5.6 shows the relative differences of the parameters compared to the kerosene baseline at this reduced range, and Table 5.7 shows the relative differences of scenarios 2, 3 and 4 with respect to full hydrogen. Subsequently, observations for each scenario at this reduces range will be made, including the the breakdown of MTOW and OEW for each scenario.

Table 5.5: Results from evaluating scenarios at 2500 km range

Outputs	**Baseline kerosene**	**Full Hydrogen**	**Reserve on kerosene**	**50/50, hydrogen first**	**50/50, kerosene first**
			Configuration Outputs		
l_{fus} $[m]$	42.2	46.4	44.5	42.8	43.6
l_{tank} $[m]$	3.58	7.67	5.85	4.19	4.99
S $[m^2]$	128.0	124.2	124.6	124.4	124.2
A $[-]$	10.1	10.4	10.4	10.4	10.4
S_h $[m^2]$	29.2	29.4	26.4	27.6	26.9
S_v $[m^2]$	23.8	21.0	22.0	23.0	22.5
S_h/S $[-]$	0.228	0.237	0.212	0.222	0.216
W/S $[N/m^2]$	4725	4725	4725	4725	4725
T/W $[-]$	0.294	0.335	0.322	0.311	0.317
T_{TO} $[kN]$	178	197	189	183	186
$L/D_{midcruise}$ $[-]$	16.9	16.7	17.0	17.1	16.8
C_{D_0} $[counts]$	181	191	185	184	185
m_{JetA} $[t]$	10.1	–	3.17	5.70	4.34
m_{H_2} $[t]$	–	3.72	2.57	1.55	2.06
m_{tank} $[t]$	0.527	1.61	1.17	0.779	0.975
η_{tank}	–	0.697	0.687	0.666	0.679
$MTOW$ $[t]$	61.7	59.8	60.0	59.9	59.8
OEW $[t]$	36.6	41.1	39.3	37.7	38.4
FW $[t]$[4]	10.1	3.72	5.74	7.25	6.40
		Performance output: SEC $[MJ/PAX/km]$ of mission including reserve phase			
TTW_{H_2+JetA}[5] of mission only, without reserve phase	0.793	0.816	0.815	0.782	0.787
TTW_{H_2+JetA}	0.816	0.833	0.832	0.808	0.812
TTW_{H_2}	–	0.833	0.576	0.348	0.462
TTW_{JetA}	0.816	–	0.256	0.460	0.350
$WTT_{H_2,2025}$	–	0.520	0.360	0.218	0.289
$WTT_{H_2,2035}$	–	0.483	0.334	0.202	0.268
$WTT_{H_2,2050}$	–	0.477	0.330	1.99	0.265
$WTW_{H_2+JetA,2025}$	0.816	1.35	1.19	1.03	1.10
$WTW_{H_2+JetA,2035}$	0.816	1.32	1.16	1.01	1.08
$WTW_{H_2+JetA,2050}$	0.816	1.31	1.16	1.01	1.08
		Performance output: CO_2eq $[g/PAX/km]$ of mission including reserve phase			
$TTW_{H_2+JetA,2025}$	86.5	95.8	93.3	88.9	90.3

Continued on next page

---

[4] FW is the sum of m_{JetA} and m_{H_2}. Results may slightly differ due to rounding.

[5] Reserve energy is approximated for all scenarios using m_{JetA} from the ‘Reserve on kerosene’-scenario at 2500 km range

Table 5.5 – *continued from previous page*

Outputs	**Baseline kerosene**	**Full Hydrogen**	**Reserve on kerosene**	**50/50, hydrogen first**	**50/50, kerosene first**
$TTW_{H_2+JetA,2035}$	86.5	75.8	79.5	80.5	79.2
$TTW_{H_2+JetA,2050}$	86.5	46.7	59.4	68.3	63.0
$TTW_{H_2,2025}$	–	95.8	66.2	40.1	53.2
$TTW_{H_2,2035}$	–	75.8	52.4	31.7	42.1
$TTW_{H_2,2050}$	–	46.7	32.3	19.5	25.9
TTW_{JetA}	86.5	–	27.1	48.8	37.1
$WTT_{H_2,2025}$	–	59.8	41.4	25.0	33.2
$WTT_{H_2,2035}$	–	43.9	30.4	18.4	24.4
$WTT_{H_2,2050}$	–	26.8	18.5	11.2	14.9
$WTW_{H_2+JetA,2025}$	86.5	156	135	114	124
$WTW_{H_2+JetA,2035}$	86.5	120	110	98.8	104
$WTW_{H_2+JetA,2050}$	86.5	73.5	77.9	79.5	77.9

Table 5.6: Relative difference of parameters from different scenarios compared to kerosene baseline for 2500 km

Outputs	**Full Hydrogen** Δ	**Reserve on kerosene** Δ	**50/50, hydrogen first** Δ	**50/50, kerosene first** Δ
		Configuration Outputs		
l_{fus} (%)	+10	+6	+1	+3
l_{tank} (%)	+115	+64	+17	+40
S (%)	-3	-3	-3	-3
A (%)	+3	+3	+3	+3
S_h (%)	+1	-10	-6	-8
S_v (%)	-11	-7	-3	-5
S_h/S (%)	+4	-7	-3	-5
W/S (%)	0	0	0	0
T/W (%)	+14	+10	+6	+8
T_{TO} (%)	+11	+7	+3	+5
$L/D_{midcruise}$ (%)	-1	+1	+2	0
C_{D_0} (%)	+5	+3	+2	+2
m_{JetA} (%)	–	-69	-44	-57
m_{H_2} (%)	–	–	–	–
m_{tank} (%)	+206	+122	+48	+85
η_{tank} (%)	–	–	–	–
$MTOW$ (%)	-3	-3	-3	-3
OEW (%)	+12	+8	+3	+5
FW (%)	-63	-43	-28	-37
		Performance output: SEC (%) of mission including reserve phase		
TTW_{H_2+JetA} (%) of mission only, without reserve phase	+3	+3	-1	-1

Continued on next page

Table 5.6 – *continued from previous page*

Outputs	**Full Hydrogen** Δ %	**Reserve on kerosene** Δ %	**50/50, hydrogen first** Δ %	**50/50, kerosene first** Δ %
TTW_{H_2+JetA} (%)	+2	+2	-1	0
TTW_{H_2} (%)	–	–	–	–
TTW_{JetA} (%)	–	-69	-44	-57
$WTT_{H_2,2025}$ (%)	–	–	–	–
$WTT_{H_2,2035}$ (%)	–	–	–	–
$WTT_{H_2,2050}$ (%)	–	–	–	–
$WTW_{H_2+JetA,2025}$ (%)	+66	+46	+26	+35
$WTW_{H_2+JetA,2035}$ (%)	+61	+43	+24	+32
$WTW_{H_2+JetA,2050}$ (%)	+61	+42	+24	+32
Performance output: CO_2eq (%) of mission including reserve phase				
$TTW_{H_2+JetA,2025}$ (%)	+11	+8	+3	+4
$TTW_{H_2+JetA,2035}$ (%)	-12	-8	-7	-8
$TTW_{H_2+JetA,2050}$ (%)	-46	-31	-21	-27
$TTW_{H_2,2025}$ (%)	–	–	–	–
$TTW_{H_2,2035}$ (%)	–	–	–	–
$TTW_{H_2,2050}$ (%)	–	–	–	–
TTW_{JetA} (%)	–	-69	-44	-57
$WTT_{H_2,2025}$ (%)	–	–	–	–
$WTT_{H_2,2035}$ (%)	–	–	–	–
$WTT_{H_2,2050}$ (%)	–	–	–	–
$WTW_{H_2+JetA,2025}$ (%)	+80	+56	+32	+43
$WTW_{H_2+JetA,2035}$ (%)	+38	+27	+14	+20
$WTW_{H_2+JetA,2050}$ (%)	-15	-10	-8	-10

Comparing the outcomes of the scenarios at 2500 km to the kerosene baseline, the results show similar trends to the comparison at 5000 km in terms of the increase and decrease of parameters, however, the amount of increase or decrease shows some differences. For the fuselage length, the increase in length for full hydrogen is around half of the increase in fuselage length at 5000 km. However, for the other scenarios, with reduced hydrogen use, the increase in fuselage length is less at 2500 km range than at 5000 km range. This can explained by the fact that the parts flown on hydrogen take up a smaller part of entire mission at reduced range. Similar behaviour is noticed for the increase in OEW with increasing hydrogen weight. The reduction in total fuel weight for 2500 km is similar compared to 5000 km. Regarding the 50/50 scenarios, also at 2500 km a decrease in combined fuel weight and an increase in OEW can be seen for the 50/50 scenario when kerosene is used first. However, the combination of these effects cause MTOW to decrease by a small amount for the kerosene first scenario as well, which was not the case at 5000 km.

As the energy consumption and CO_2 are expressed per passenger-kilometre, these parameters show large similarities for 2500 km compared to 5000 km. This means that also the increase of the specific fuel consumption and equivalent CO_2 emissions are similar to 5000 km, such that a reduction in WTW emissions is also only observed for the year 2050.

Table 5.7: Relative difference of parameters from different scenarios compared to full hydrogen for 2500 km

Outputs	**Reserve on kerosene** Δ %	**50/50, hydrogen first** Δ %	**50/50, kerosene first** Δ %
Configuration Outputs			
l_{fus} (%)	-4	-8	-6
l_{tank} (%)	-24	-45	-35
S (%)	0	0	0
A (%)	0	0	0
S_h (%)	-10	-6	-9
S_v (%)	+5	+9	+7
S_h/S (%)	-11	-6	-9
W/S (%)	0	0	0
T/W (%)	-4	-7	-5
T_{TO} (%)	-4	-7	-5
$L/D_{midcruise}$ (%)	+2	+2	0
C_{D_0} (%)	-3	-4	-3
m_{JetA} (%)	–	–	–
m_{H_2} (%)	-31	-58	-45
m_{tank} (%)	-27	-52	-40
η_{tank} (%)	-1	-4	-3
$MTOW$ (%)	0	0	0
OEW (%)	-4	-8	-6
FW (%)	+54	+95	+72
Performance output: SEC (%) of mission including reserve phase			
TTW_{H_2+JetA} (%) of mission only, without reserve phase	0	-4	-4
TTW_{H_2+JetA} (%)	0	-3	-3
TTW_{H_2} (%)	-31	-58	-45
TTW_{JetA} (%)	–	–	–
$WTT_{H_2,2025}$ (%)	-31	-58	-45
$WTT_{H_2,2035}$ (%)	-31	-58	-45
$WTT_{H_2,2050}$ (%)	-31	-58	-45
$WTW_{H_2+JetA,2025}$ (%)	-12	-24	-19
$WTW_{H_2+JetA,2035}$ (%)	-11	-23	-18
$WTW_{H_2+JetA,2050}$ (%)	-11	-23	-18
Performance output: CO_2eq (%) of mission including reserve phase			
$TTW_{H_2+JetA,2025}$ (%)	-3	-7	-6
$TTW_{H_2+JetA,2035}$ (%)	+5	+6	+5
$TTW_{H_2+JetA,2050}$ (%)	+27	+46	+35
$TTW_{H_2,2025}$ (%)	-31	-58	-45
$TTW_{H_2,2035}$ (%)	-31	-58	-45
$TTW_{H_2,2050}$ (%)	-31	-58	-45
TTW_{JetA} (%)	–	–	–
$WTT_{H_2,2025}$ (%)	-31	-58	-45

Continued on next page

Table 5.7 – *continued from previous page*

Outputs	**Reserve on kerosene** Δ %	**50/50, hydrogen first** Δ %	**50/50, kerosene first** Δ %
$WTT_{H_2,2035}$ (%)	-31	-58	-45
$WTT_{H_2,2050}$ (%)	-31	-58	-45
$WTW_{H_2+JetA,2025}$ (%)	-13	-27	-21
$WTW_{H_2+JetA,2035}$ (%)	-8	-17	-13
$WTW_{H_2+JetA,2050}$ (%)	+6	+8	+6

Comparing the relative difference of scenarios 2, 3 and 4 with respect to the full hydrogen concept at 2500 km, similar trends can be observed as for this comparison at 5000 km. However, there are still some differences worth noting.

First of all, the decrease in fuselage length for decreasing hydrogen use is smaller than for 5000 km. This is also the case for the decrease in OEW. Regarding the fuel weight, a 10% larger decrease in hydrogen weight is observed for the reserve on kerosene scenario at 2500 km than at 5000 km. This is due to the fact that the nominal cruise part is now shorter, whereas the reserve part remained the same. Due to the same reason, the increase in total fuel weight is larger for the reserve on kerosene and 50/50 hydrogen first scenarios at 2500 km compared to 5000 km. For the 50/50 kerosene first scenario, the decrease in hydrogen weight is less at 2500 km, as the reserve part of equal length is now flown on hydrogen.

The larger decrease in hydrogen weight at 2500 km for the reserve on kerosene scenario also results in a larger decrease of the specific energy consumption and equivalent WTT and TTW CO_2 emissions, as well as the equivalent WTW CO_2 emissions for 2025 and 2035. In Section 5.1.4 below, the weight breakdowns of the kerosene baseline and aircraft concepts for each scenario at 2500 km range are presented.

5.1.4. Scenarios weight breakdown: 2500 km

The pie-charts below show the breakdown of the MTOW and OEW for the kerosene baseline aircraft and each scenario for the range of 2500 km.

Weight breakdown kerosene baseline

At 2500 km, the OEW contributes for almost 60% to the MTOW of the kerosene baseline concept. This is a slight increase compared to the kerosene baseline at 5000 km. This is mainly due to the fact that the kerosene contributes less to the MTOW at this reduced range, as can be seen in Figure 5.15. The OEW breakdown of the kerosene baseline in Figure 5.16 shows large similarities with the one at 5000 km, meaning that the fuselage takes up little over a quarter of the OEW and the wing close to a fifth.

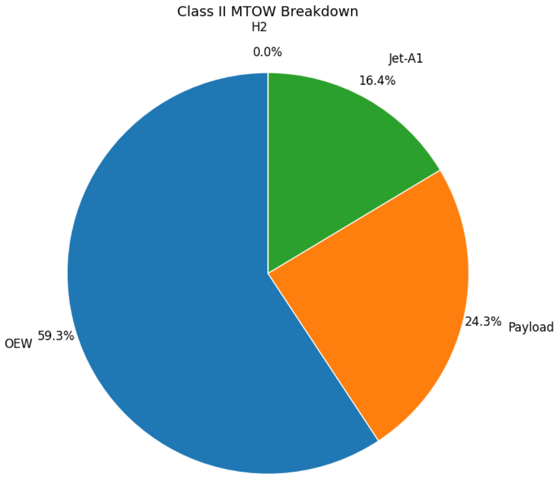

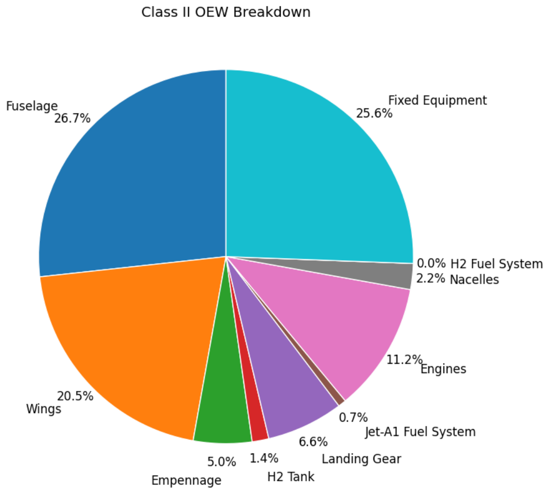

Figure 5.15: MTOW breakdown kerosene baseline at 2500 km range

Figure 5.16: OEW breakdown kerosene baseline at 2500 km range

Scenario 1: Full hydrogen

For the full hydrogen scenario, the expected increase in OEW as part of the MTOW is visible in the MTOW breakdown in Figure 5.17. The contribution of OEW to the MTOW is pretty much similar for this scenario at 2500 km range as it was at 5000 km. However, the contribution of the hydrogen weight is about a third lower at this reduced range. As can be seen in Figure 5.18, this lower hydrogen weight increase is also reflected in a smaller contribution of the hydrogen tank to the OEW. Also the fuselage weight contributes less to OEW at 2500 km than at 5000 km range.

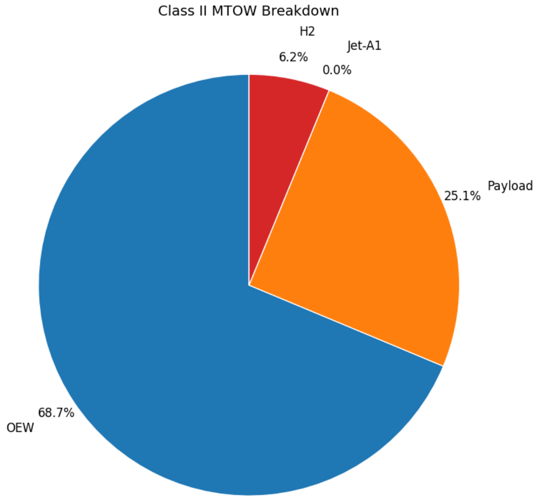

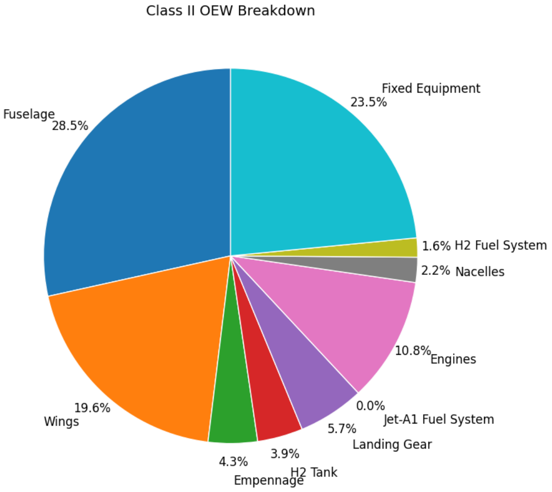

Figure 5.17: MTOW breakdown full hydrogen at 2500 km range

Figure 5.18: OEW breakdown kerosene baseline at 2500 km range

Scenario 2: Reserve on kerosene

For the scenario where the reserve phase is flown on kerosene, it can be seen in Figure 5.19 that the OEW contributes less to the MTOW compared to the full hydrogen scenario. For scenario 2, the contribution of OEW is equal at 2500 km and 5000 km range. The contribution of the kerosene weight is also very similar. At the reduced range, it can again be noted that the contribution of the hydrogen weight reduces. This also results in the hydrogen tank to contribute less to the OEW at 2500 km, as shown by Figure 5.20. The same goes for the fuselage weight.

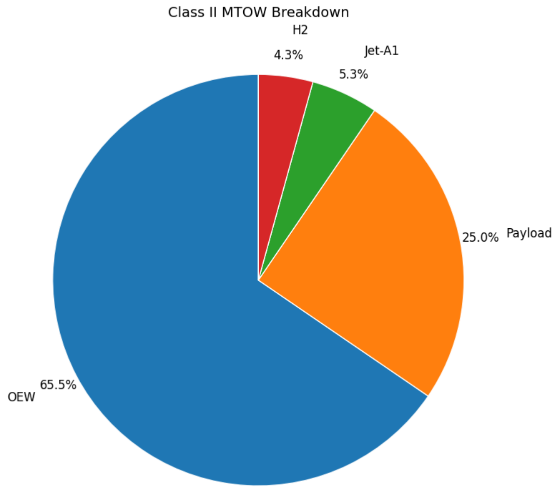

Figure 5.19: MTOW breakdown reserve at 2500 km range

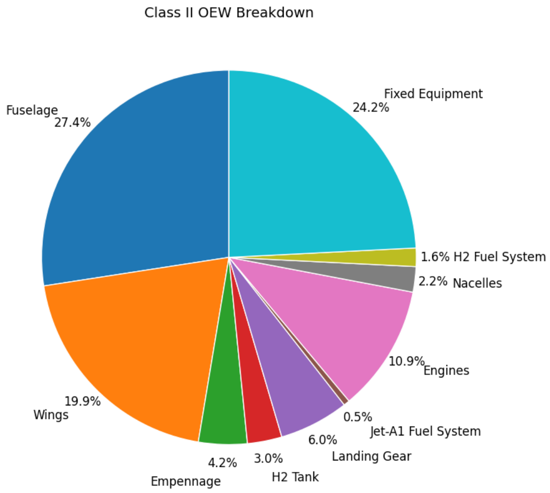

Figure 5.20: OEW breakdown reserve on kerosene at 5000 km range

Scenario 3: 50/50 cruise hydrogen first

For the 50/50 scenario where hydrogen is used first, Figure 5.21 shows that both the contribution of hydrogen and kerosene weight to the MTOW is reduced compared to this scenario at 5000 km, and therefore the OEW contributing more. Figure 5.22 shows a slight decrease in hydrogen tank and fuselage contribution compared to scenario 2 at 2500 km and also scenario 3 at 5000 km. The contribution of the wing is increased slightly for both of these cases.

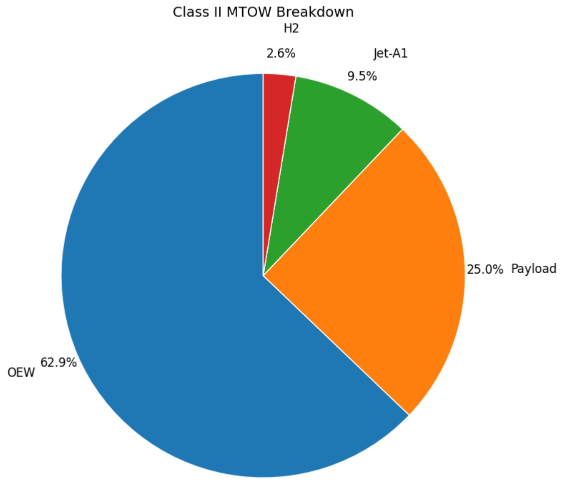

Figure 5.21: MTOW breakdown 50/50 fuel split cruise, hydrogen first at 2500 km range

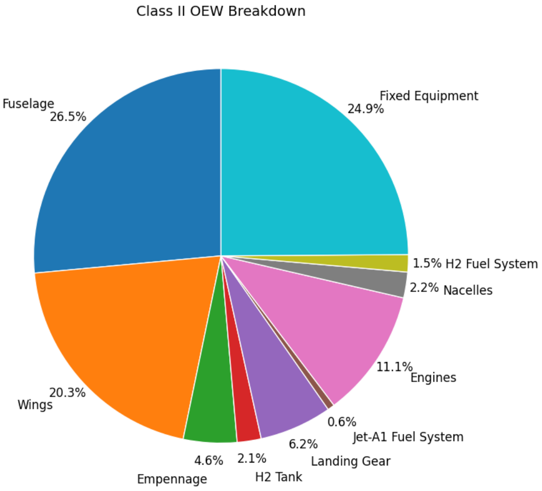

Figure 5.22: OEW breakdown 50/50 fuel split cruise, hydrogen first at 2500 km range

Scenario 4: 50/50 cruise kerosene first

Finally, for the 50/50 scenario where kerosene is used first, Figure 5.23 shows that the contribution of hydrogen weight to MTOW is increased compared to scenario 3 at this range, whereas the contribution of kerosene is reduced. The increase in hydrogen weight causes the hydrogen tank and fuselage to take up a larger part of the OEW at this range, as seen in Figure 5.24. However, at 2500 km range, the contributions of the fuel weights are smaller than at 5000 km range for this scenario. Therefore, also the contributions of hydrogen tank and fuselage weight to the OEW are smaller at 2500 km than at 5000 km.

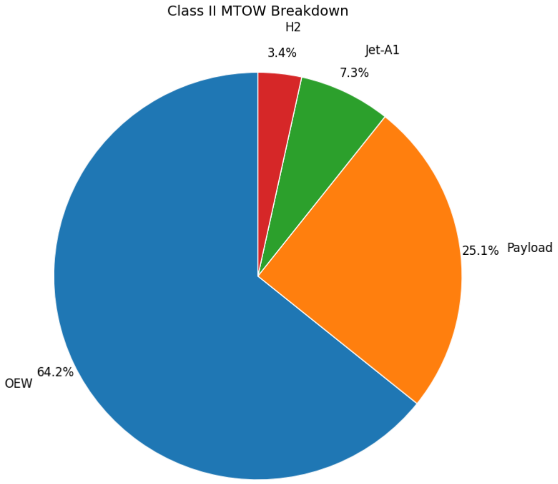

Figure 5.23: MTOW breakdown 50/50 fuel split cruise, kerosene first at 2500 km range

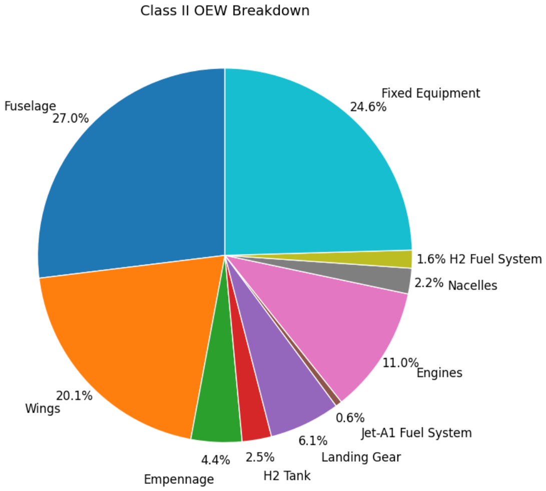

Figure 5.24: OEW breakdown 50/50 fuel split cruise, kerosene first at 2500 km range

5.1.5. General observations from the comparative analysis

After having analysed the outcomes of the scenarios and the weight breakdowns at both 5000 and 2500 km range, some general observations can be made.

First of all, the increase in hydrogen use causes an increase in fuselage length compared to the kerosene baseline. At 5000 km, this increase is significant, whereas the effect is less pronounced at 2500 km range. Employing partial instead of full use of hydrogen during the mission, the effect of the fuselage length increase is damped. At 2500 km range, this effect is more pronounced than at 5000 km range.

Secondly, the increase in hydrogen weight causes the total fuel weight to reduce significantly. However, the accompanying increase in hydrogen tank mass and fuselage mass result in the OEW to increase significantly. The result is that the MTOW shows a slight decrease with increasing hydrogen weight. The more damped effect of hydrogen weight and fuselage length increase at 2500 km compared to 5000 km, also results in the OEW increase to be less pronounced for the reduced range.

Finally, the increase in hydrogen weight causes the well-to-wake specific energy consumption to increase significantly. This is largely contributed to by the energy required to produce hydrogen (well-to-tank). This also causes the well-to-wake equivalent CO_2 emissions to increase significantly compared to the kerosene baseline for the years 2025 and 2035, in which the carbon intensity of the hydrogen production is still high. Therefore, for these years, reducing the amount of hydrogen by flying a dual-fuel mission results in the well-to-wake specific energy consumption and equivalent CO_2 emissions to be decreased compared to the use of only hydrogen. For the year 2050, the projected reduction in the equivalent CO_2 emissions of hydrogen production results in a decrease in well-to-wake emissions compared to the kerosene baseline. Therefore, also employing the dual-fuel use is less favourable from an emissions point of view at that point in the future, as the use of kerosene now negatively impacts the equivalent CO_2 emissions.

5.2. Sensitivity Analysis

Next to a comparative analysis, sensitivity analyses are done to get more insight in the effect of changing parameters on the aircraft design. First of all, Section 5.2.1 will look into varying the fuel split during the cruise phase. Section 5.2.2 will present a sensitivity analysis into varying payload and range requirements.

5.2.1. Varying fuel split during cruise

To get a better understanding of the effect of varying the amount of hydrogen during the mission, a sensitivity study is performed in which the fuel split during the cruise phase is varied. The variation in fuel split is done from a fuel split for the cruise phase from 0 (100% kerosene) to 1 (100% hydrogen) with 10% increments. Furthermore, the flight phases until cruise are flown on hydrogen, whereas the descend and reserve phases after the cruise phase are flown on kerosene. To visually clarify this, Figure 5.25 and Figure 5.26 show the mission profiles at the start and end of this sensitivity analysis, respectively.

As in the comparative analysis, this cruise fuel split sensitivity analysis is done for a flight range of 5000 km and 2500 km.

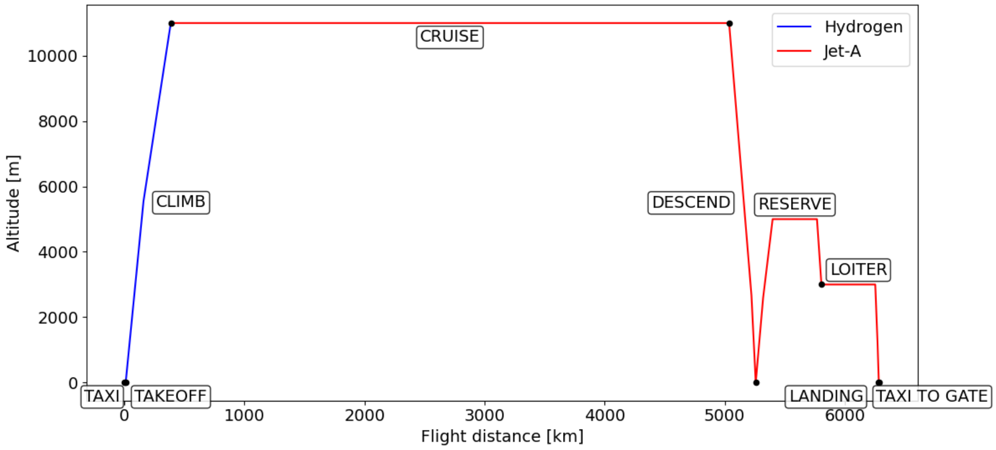

Figure 5.25: Mission profile for fuel split cruise phase equal to 0

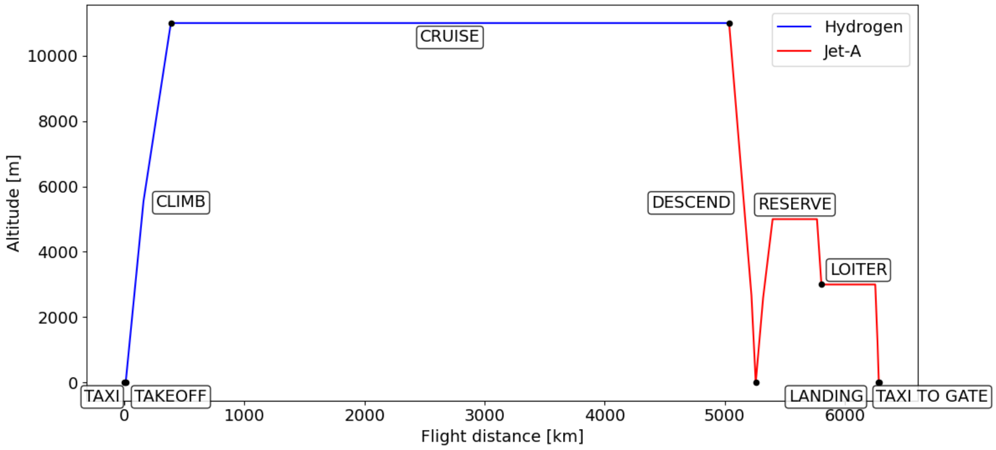

Figure 5.26: Mission profile for fuel split cruise phase equal to 1

Weight change at 5000 km range

Figure 5.27 shows the change of aircraft weight components with increasing fuel split in the cruise phase. Below that, Figure 5.28 shows change in OEW in relation to the change in fuselage, wing and hydrogen tank weight.

From these figures, it can be observed that the MTOW does not change much with increasing hydrogen use. This results from a combination of an increase in OEW with hydrogen weight increase, but a reduction in fuel weight that is mainly driven by a reduction in kerosene weight.

Looking at the progression of OEW, it can be seen that the increase in OEW is mainly contributed to by a increase in hydrogen tank and fuselage weight.

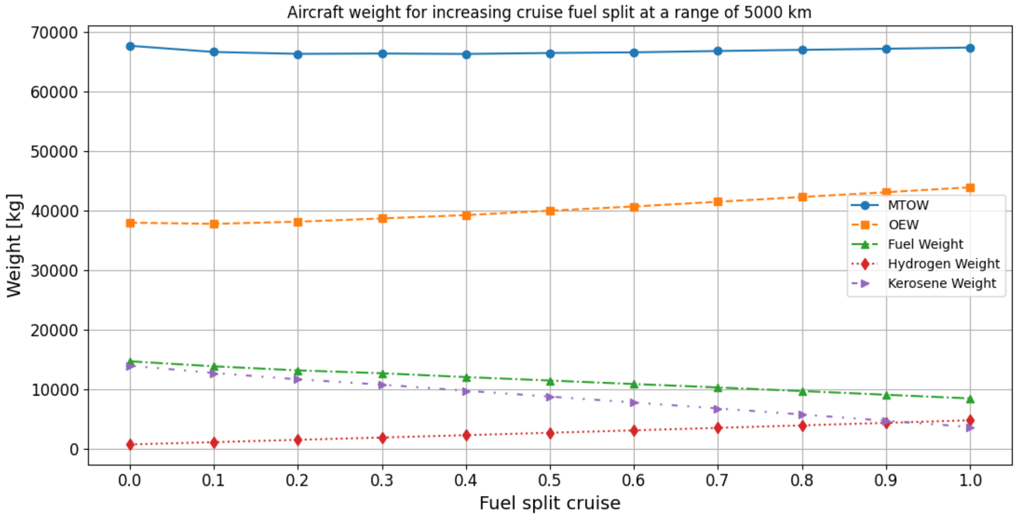

Figure 5.27: Change of weight components for increasing cruise fuel split at 5000 km range

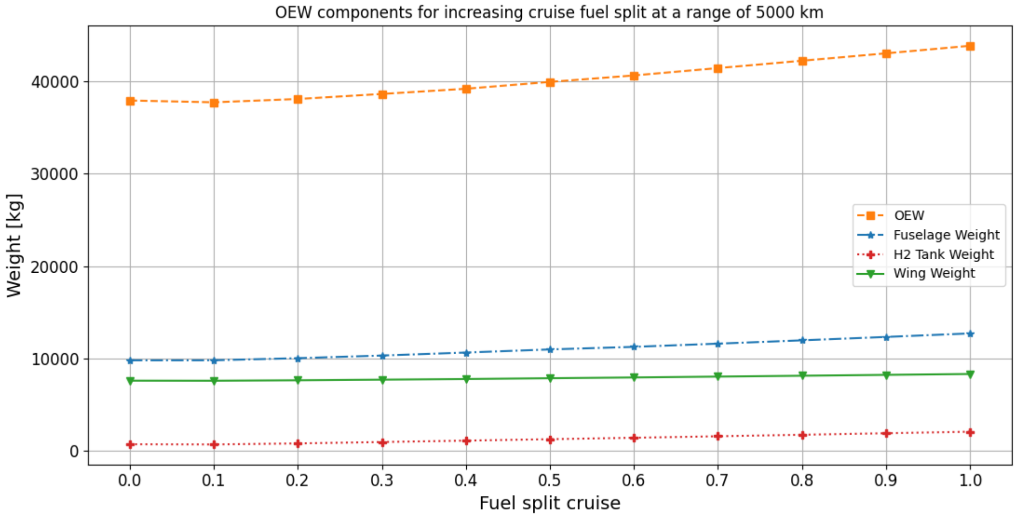

Figure 5.28: Breakdown OEW components for increasing cruise fuel split at 5000 km range

Aircraft geometry change at 5000 km range

The change in weight is mainly driven by a change in aircraft geometry. Figure 5.29 shows the change in fuselage and hydrogen tank length for increasing cruise fuel split at 5000 km range. Next to that, Figure 5.30 shows the change in wing and tail area at this range.

From the figures it can be seen that the fuselage and hydrogen tank follow a similar trend with increasing fuel split. From a fuel split of 0.2 onwards, it can be observed that the length of the fuselage and the hydrogen tank increases in linear fashion with increasing fuel split. This is in line with the increase of hydrogen weight discussed before. However, from a fuel split 0 to 0.1, the fuselage length remains almost constant. This can be explained by the fact that at fuel split 0, the spherical tank that was already in the aircraft suffices and is filled only to around three-quarters, such that at fuel split 0.1 the increase in tank length and thereby fuselage length is limited compared to later fuel splits. Regarding the wing area, it is noticed in Figure 5.30 that this remains almost constant with increasing fuel split, whereas the horizontal tailplane initially decreases with increasing fuel split, but starts increasing after a fuel split of 0.4.

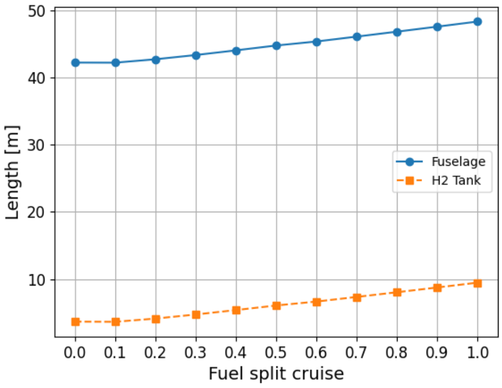

Figure 5.29: Change in fuselage and hydrogen tank length for increasing cruise fuel split at 5000 km range

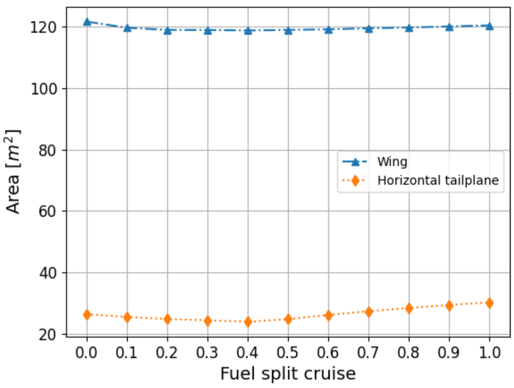

Figure 5.30: Wing and horizontal tailplane area for increasing cruise fuel split at 5000 km range

Lift-to-drag ratio change at 5000 km range

The change in wing and horizontal tail area, as well as the fuselage length, relates closely to the aerodynamic efficiency of the aircraft. Figure 5.31 shows the change in lift-to-drag ratio for increasing fuel split at 5000 km range. From this figure it can be seen that the L/D-ratio initially increases with increasing hydrogen weight until a cruise fuel split of 0.4. After this, the L/D ratio reduces due to the combination of the increase in horizontal tailplane area and fuselage length and thereby increasing drag.

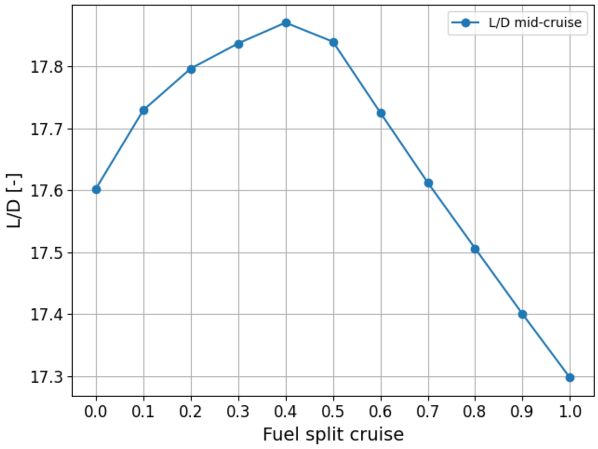

Figure 5.31: Change in lift-to-drag ratio for increasing cruise fuel split at 5000 km range

Energy & emissions at 5000 km

Changing fuel weight affects the energy consumption of the aircraft and the emissions produced by it. As explained in Section 3.11, the energy and emissions are evaluated at three moments in time, 2025, 2035 and 2050, based on projections of a decarbonising global electricity grid and efficiency gains in hydrogen electrolysis and energy required for hydrogen liquefaction. Figure 5.32 and Figure 5.33 show the change in specific energy consumption and equivalent CO_2 emissions with increasing fuel split, respectively. Similar to the results presented in the comparative analysis, SEC and CO_2eq are split into the WTT and TTW contributions. Both graphs also contain lines showing CO_2eq and SEC for the kerosene baseline and full hydrogen aircraft concepts as mentioned in Section 5.1, such that a comparison can be made between these single-fuel and dual-fuel concepts.

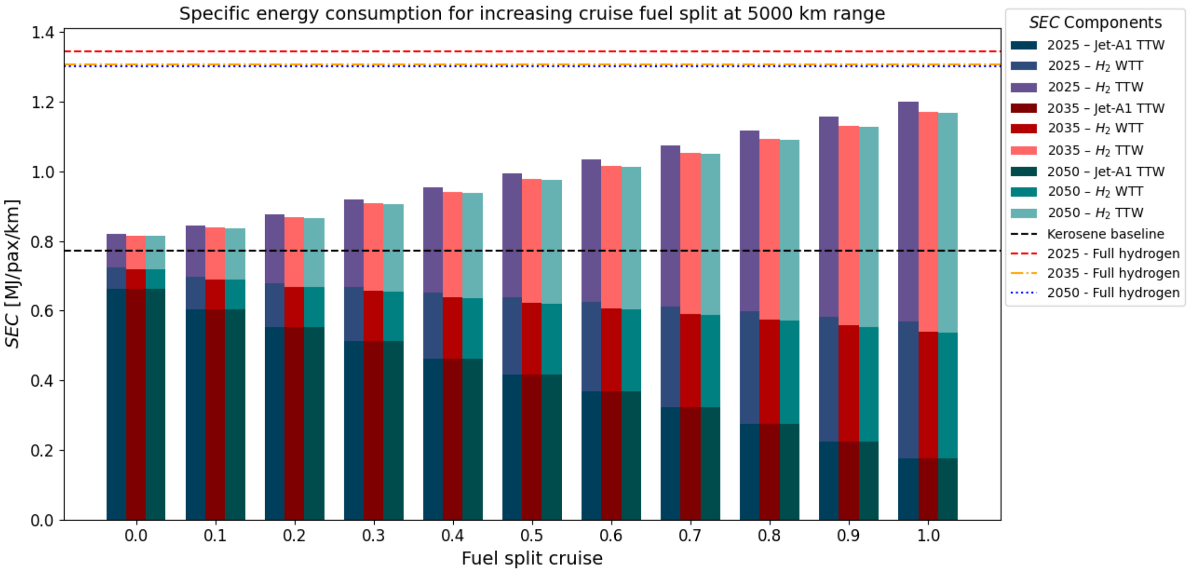

Figure 5.32: Change in specific energy consumption for increasing cruise fuel split at 5000 km range

In Figure 5.32 above, it can be seen that the total specific energy consumption increases with increasing hydrogen use for all timepaths. This can be attributed to the large WTT and TTW energy consumption of hydrogen, which increases more than the reduction in energy consumption from reducing the kerosene use. Even though the energy consumption of the kerosene baseline is exceeded, the energy consumption is still lower than the full hydrogen concepts.

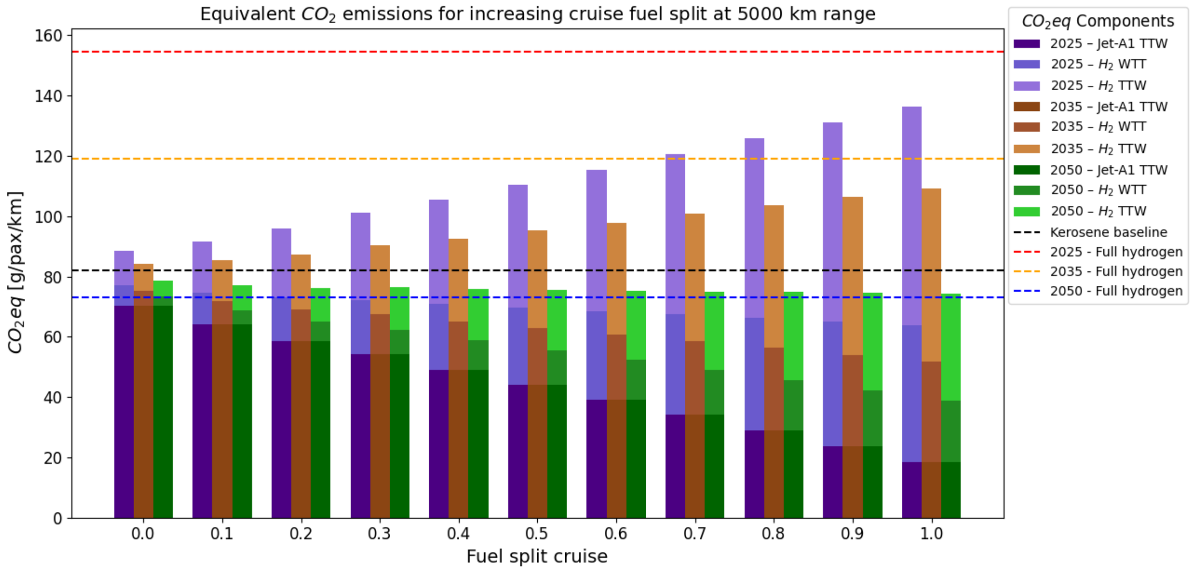

Figure 5.33: Change of equivalent CO_2 emissions for increasing cruise fuel split at 5000 km range

Figure 5.33 above shows that the total equivalent CO_2 emissions increase with increasing hydrogen use for the years 2025 and 2035, even though the emissions from kerosene reduce. However, what can be noted is that combining hydrogen and kerosene results in lower equivalent CO_2 emissions than the full hydrogen concepts for 2025 and 2035. Only for the year 2050, the carbon intensity of hydrogen production is low enough to cause a decrease in total equivalent CO_2 emissions. At a fuel split of 1.0, meaning the mission is comparable to the ‘reserve on kerosene’ mission, except for the descend phase, as presented in Section 5.1, the total WTW equivalent CO_2 emissions are almost equal to the full hydrogen case.

Below, the graphs resulting from the sensitivity analysis of varying the fuel split in the cruise phase are shown for a range of 2500 km.

Weight change at 2500 km range
Figure 5.34 below shows a similar decrease in MTOW with increasing hydrogen weight as compared to 5000 km. The increase in hydrogen weight and the decrease in kerosene weight are also less steep for 2500 km compared to 5000 km. Next to that, it can also be noticed that the OEW increases less with increasing hydrogen weight. This smaller increase is caused by the hydrogen tank and fuselage weight increase to be less, as can be seen in Figure 5.35.

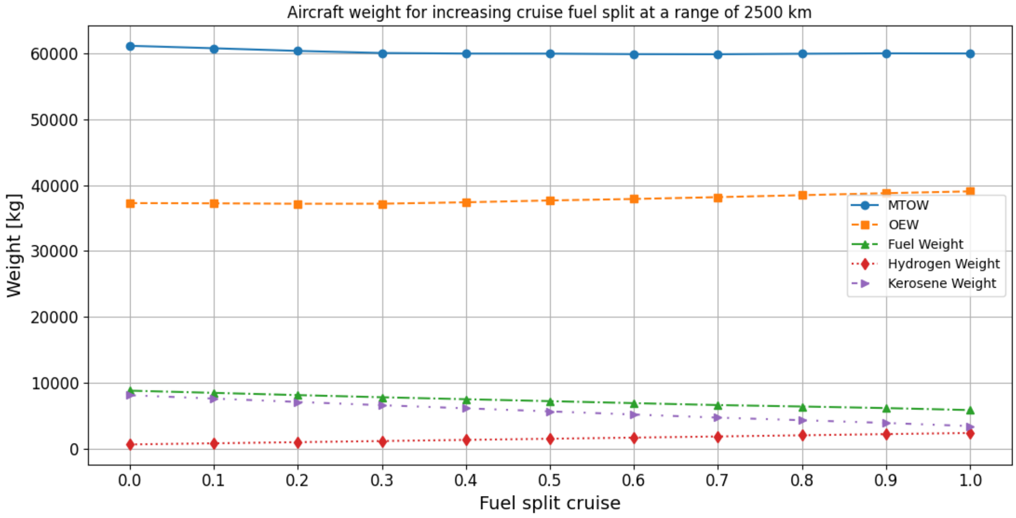

Figure 5.34: Change of weight components for increasing cruise fuel split at 2500 km range

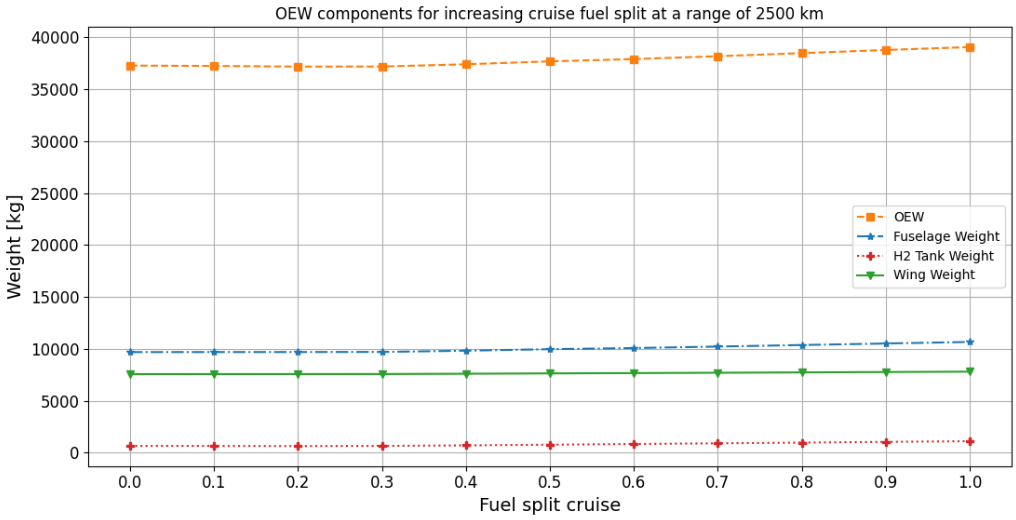

Figure 5.35: Breakdown OEW components for increasing cruise fuel split at 2500 km range

Aircraft geometry change at 2500 km range

Looking at Figure 5.36 below, it can be seen that the length of the fuselage and hydrogen tank increases with increasing hydrogen use. However, the increase in length is less steep compared to 5000 km.

The progression of the wing area in Figure 5.37 shows an initial small decrease with increasing fuel split, after which it remains (almost) constant, similar to what could be observed at 5000 km. What is different to 5000 km, is that the horizontal tailplane area keeps on decreasing with increasing fuel split at 2500 km range.

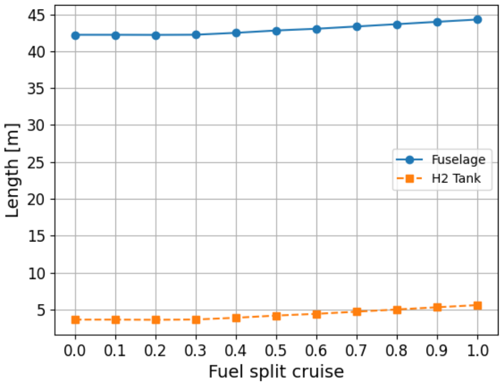

Figure 5.36: Change in fuselage and hydrogen tank length for increasing cruise fuel split at 2500 km range

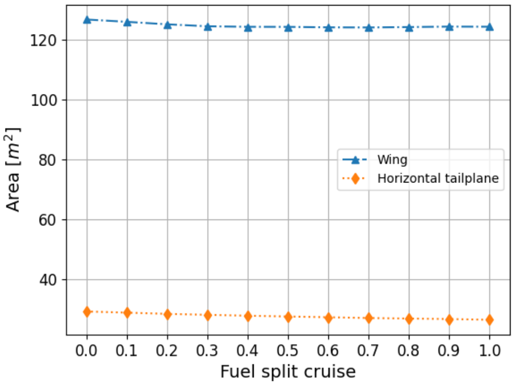

Figure 5.37: Wing and horizontal tailplane area for increasing cruise fuel split at 2500 km range

Lift-to-drag ratio change at 2500 km range

The progression of the lift-to-drag ratio at 2500 km, as seen below in Figure 5.38, shows similar behaviour as for 5000 km, meaning an initial increase until about a fuel split of 0.5. However, the magnitude of the change is smaller for 2500 km range when compared to 5000 km.

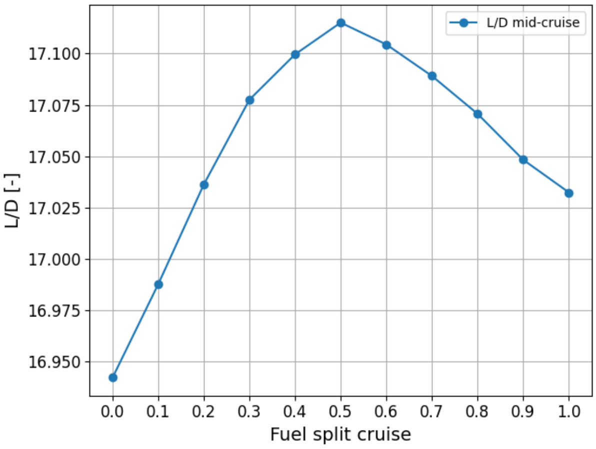

Figure 5.38: Change in lift-to-drag ratio for increasing cruise fuel split at 2500 km range

Energy & emissions at 2500 km

Figure 5.39 below shows a similar increase in specific energy consumption with increasing fuel split for 2500 km range as could be observed for 5000 km. A difference can be noted in the fact that SEC is higher at a fuel split of 0.0 and increases less steeply than for 5000 km range.

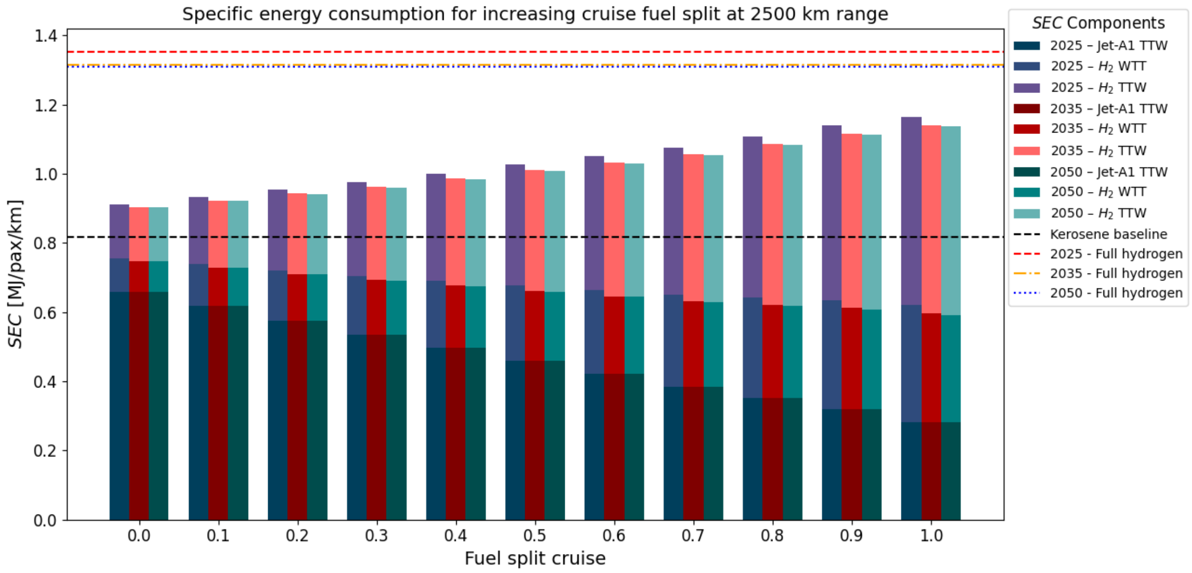

Figure 5.39: Change in specific energy consumption for increasing cruise fuel split at 2500 km range

Just like the progression of SEC showing similar behaviour for 2500 and 5000 km, this is also the case for the progression of equivalent CO_2 emissions at 2500 km, shown in Figure 5.40 below, when comparing to 5000 km range. Next to that, the smaller increase of SEC that was noted at 2500 km, is also reflected by a smaller increase of equivalent CO_2 for 2025 and 2035, and a smaller decrease of equivalent CO_2 for 2050 at 2500 km range. Additionally, it can be noted, similar to 5000 km, that the combination of hydrogen and kerosene results in lower equivalent CO_2 emissions than a full hydrogen concept for 2025 and 2035. However, for 2050 the full hydrogen concept results in lower equivalent CO_2 emissions.

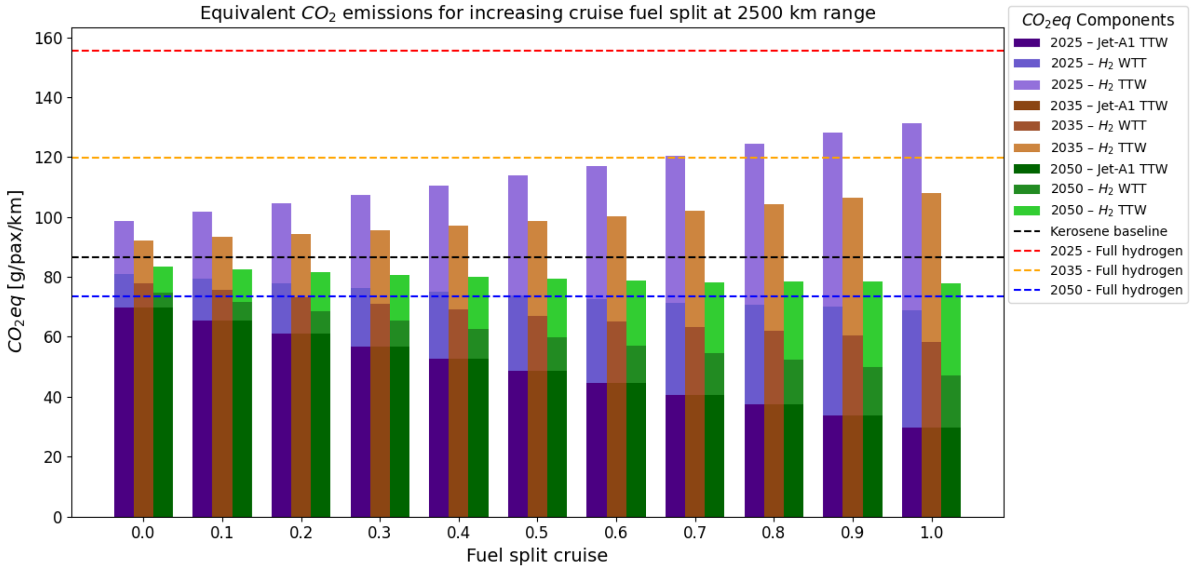

Figure 5.40: Change of equivalent CO_2 emissions for increasing cruise fuel split at 2500 km range

5.2.2. Varying payload and range

To get more insight into the effect of changing payload, i.e. the number of passengers, and range, a sensitivity analysis was done where these parameters were varied. The effect on MTOW, OEW and SEC and CO_2eq will be shown in subsequent figures below. In these figures, also the change in fuel split was included, such that the effect of changing this parameter can be compared to changes in range and number of passengers. Furthermore, the baseline case is a mission at a cruise range of 2500 km, 150 passengers and a fuel split in cruise of 0.5, meaning hydrogen is used from the start of the mission until half of the cruise phase and kerosene is used for the second half of the cruise phase and the reserve and loiter part of the mission.

Effect on MTOW and OEW

Figure 5.41 and Figure 5.42 below show the change in MTOW and OEW, respectively, for a changing range, number of passengers and the fuel split in cruise, compared to a baseline case. From these figures, it can be observed that MTOW and OEW show little sensitivity to a change in the fuel split during cruise, which already became apparent from the cruise fuel split analysis previously presented in Section 5.2.1. Next to that, it can be observed that changing the range has a larger effect on OEW and MTOW, but it is still limited. What stands out from these figures is that changing the number of passengers has a large effect on MTOW and OEW.

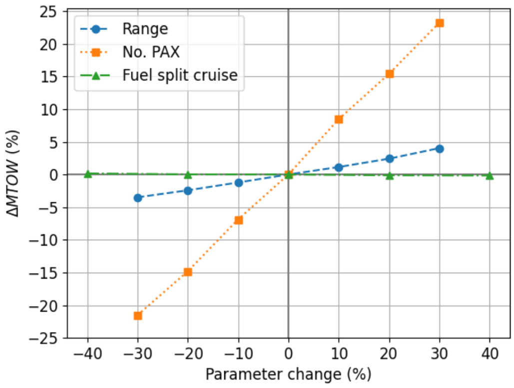

Figure 5.41: Sensitivity of MTOW to change in range, PAX, and cruise fuel split

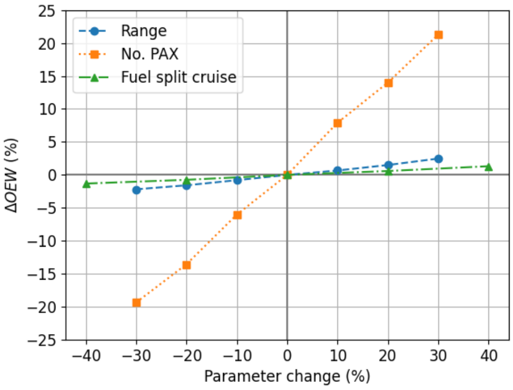

Figure 5.42: Sensitivity of OEW to change in range, PAX, and cruise fuel split

Effect on fuel weight

Figure 5.43 shows the change in total fuel weight for a changing range, number of passenger and fuel split in cruise. It can be observed that the fuel weight shows a similarly large sensitivity to a change in the number of passengers as was seen for the MTOW and OEW. Next to that, the fuel weight also shows large sensitivity to a change in flight range. Regarding the fuel split in cruise, it can be observed that an increase of this parameter results in a decrease in fuel weight, due to increased hydrogen use and decreased kerosene use. The sensitivity of the fuel weight to this parameter is smaller than to the change in range and PAX.

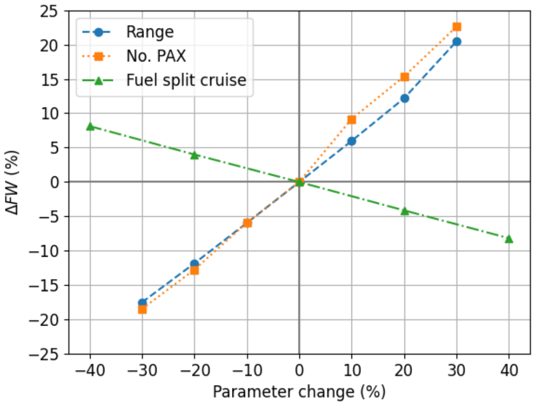

Figure 5.43: Sensitivity of fuel weight to change in range, PAX, and cruise fuel split

Figure 5.44 and Figure 5.45 below show the sensitivity of the hydrogen and kerosene weight, respectively. It can be seen that the change in fuel split in cruise logically has an inverse effect on the change in hydrogen and kerosene weight, but also that the effect is stronger than for combined fuel weight parameter. This is especially the case for hydrogen weight. These two effects combined also explain the more limited sensitivity of the total fuel weight to a change in fuel split.

Furthermore, changing the number of passengers has a significant, and similar, effect on the change of hydrogen and kerosene weight. The same goes for changing the range, for which the effect is even stronger for the change in hydrogen weight than for the change in kerosene weight.

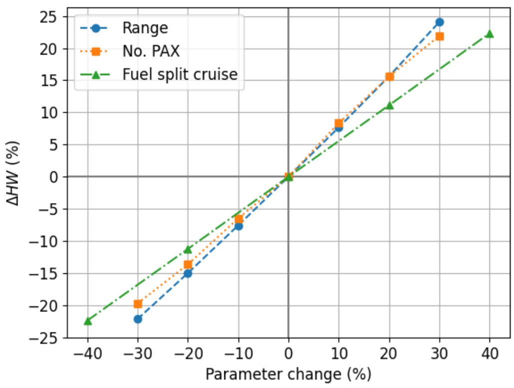

Figure 5.44: Sensitivity of hydrogen weight to change in range, PAX, and cruise fuel split

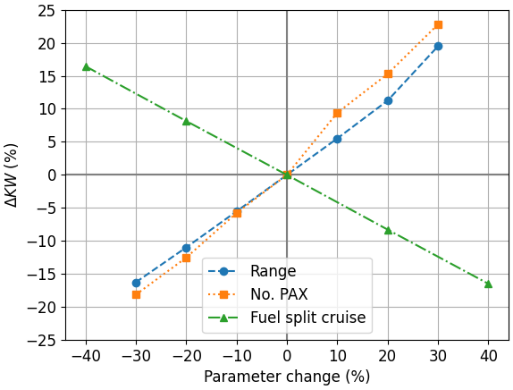

Figure 5.45: Sensitivity of kerosene weight to change in range, PAX, and cruise fuel split

Effect on energy & emissions

Lastly, the sensitivity of the specific energy consumption and equivalent CO_2 emissions to a change in range, number of passengers and fuel split in cruise will be looked into. Figure 5.46 shows the sensitivity of the SEC to these changes for 2025. For 2035 and 2050, it was found that the figures look (nearly) identical, so they were left out for conciseness. Since the SEC is computed per passenger-kilometre, a reduction in range and number of passengers increases the SEC. On the contrary, for an increase in range and passengers, a decrease of the SEC is expected. This is true for the number of passengers, for which the SEC shows a strong sensitivity. For the range, Figure 5.46 also shows a decrease in SEC for a 10% and 20% increase in range. However, this increase is smaller than the decrease in SEC for a decreasing range. Next to that, at 30% increase in range, an increase in SEC is observed. Finally, it can be observed that the SEC decreases with decreasing fuel split in cruise. This can be attributed to the decrease in WTT and TTW energy consumption of hydrogen. Even though the energy consumption from kerosene increases, the total SEC decreases. This was already observed in Figure 5.39. On the contrary, the SEC increases for an increase in fuel split during cruise.

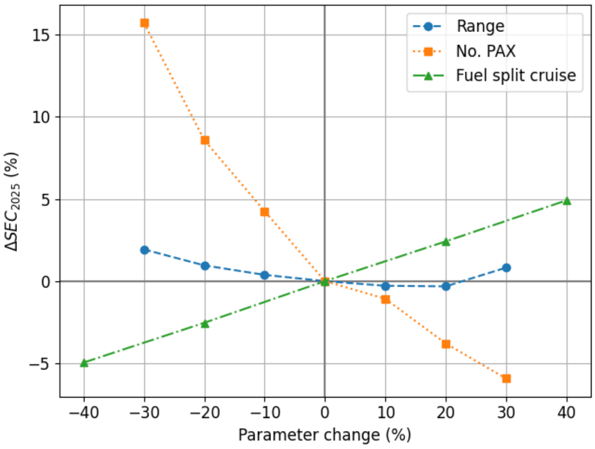

Figure 5.46: Sensitivity of specific energy consumption in 2025 to change in range, PAX, and cruise fuel split

Figures 5.47, 5.48 and 5.49 show the sensitivity of equivalent CO_2 emissions to a changing range, number of passengers and cruise fuel split for 2025, 2035 and 2050, respectively. Similar to the SEC, CO_2eq is expressed per passenger-kilometre. Therefore, for a decrease in range and number of passengers, a decrease in CO_2eq can be noticed. The sensitivity to a change in passengers is (nearly) identical for the three years. The sensitivity to a change in range also shows similar progression for the three years. However, the sensitivity is stronger further into the future, due to the projected decarbonisation of the electricity grid that the hydrogen is derived from. This aspect can also be noted when comparing the sensitivity of CO_2eq for changing fuel split in the cruise phase, as for 2025, a decrease in hydrogen use (reduced fuel split) results in a decrease in CO_2eq and vice versa. For 2035, this effect can still be noticed but is reduced due to the decarbonisation of hydrogen production. However, for 2050, further decarbonisation of hydrogen production results in an increase in CO_2eq for a reduction in hydrogen use, and a decrease in CO_2eq for an increase in hydrogen use (increased fuel split).

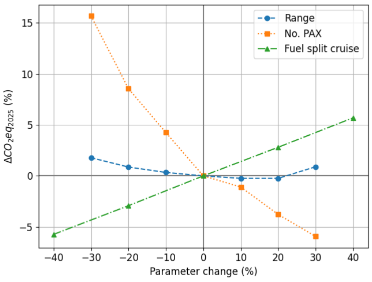

Figure 5.47: Sensitivity of equivalent CO_2 emissions in 2025 to change in range, PAX, and cruise fuel split

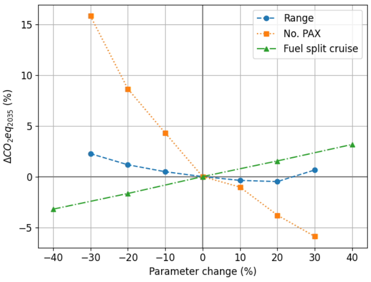

Figure 5.48: Sensitivity of equivalent CO_2 emissions in 2035 to change in range, PAX, and cruise fuel split

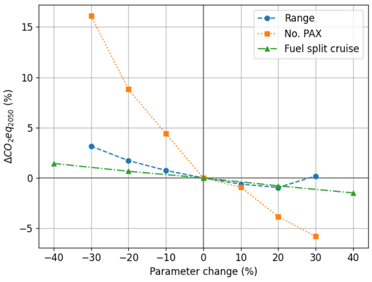

Figure 5.49: Sensitivity of equivalent CO_2 emissions in 2050 to change in range, PAX, and cruise fuel split

5.2.3. Passenger capability for fuselage length limit

In Section 5.1, it was found that implementing a hydrogen tank in the fuselage in order to fly on hydrogen has a large impact on the fuselage length for a set amount of passengers. However, it was also found that by employing a dual-fuel strategy, this effect could be limited. Additionally, in Section 5.2.2, it was presented that the number of passengers has a large effect on the weight of the aircraft concept. Combining these findings, the question rises how the operational capability in terms of the number of passengers that can be taken on board is affected for a dual-fuel aircraft. Therefore, an analysis was done to investigate potential passenger reductions required to stay within a certain fuselage length limit.

For this analysis, the aircraft design model presented in this study was used to analyse the four scenarios presented in Section 5.1 for a varying number of passengers, both for 5000 km and 2500 km range. In the passenger range, steps of six passengers were taken, which is equivalent to one row of seats for the 3-3 seats abreast configuration assumed in this study. The limit on the fuselage length was set at 45 m, as this limit is close to the maximum length of 44.5 m of the Airbus A321, which is the stretched version of the Airbus A320, that was used as reference aircraft for the comparative analysis[6]. Next to that, the results from the comparative analysis in Table 5.2 and Table 5.5 showed that the fuselage length for the different scenarios lie around this number. Figure 5.50 and Figure 5.51 below show, for 5000 and 2500 km range, respectively, the stepwise change in fuselage length for 90 to 180 passengers for the four scenarios.

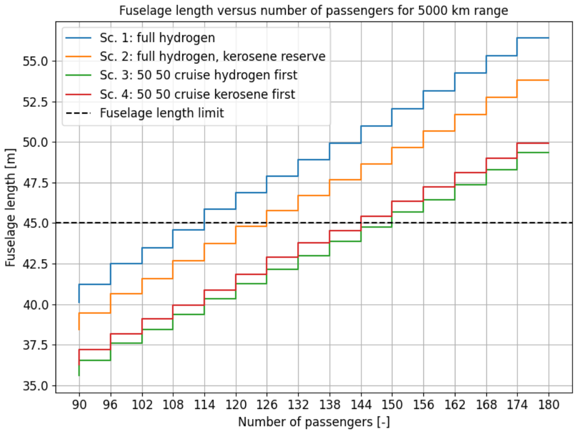

Figure 5.50: Fuselage length versus number of passengers at 5000 km range

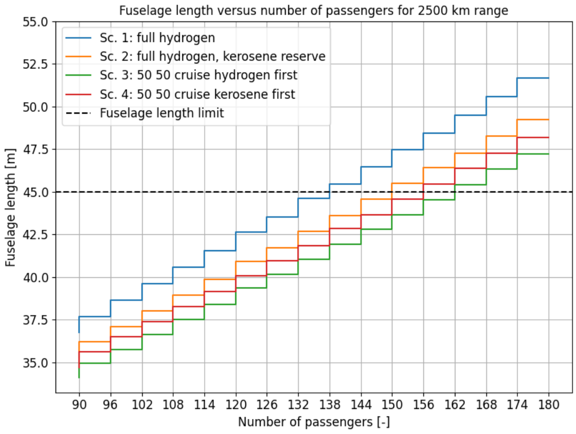

Figure 5.51: Fuselage length versus number of passengers at 2500 km range

From Figure 5.50 it can be observed that for 5000 km range, the full hydrogen exceeds the fuselage length limit already at 114 passengers. When flying the reserve part of the mission on kerosene, the number of passengers can be increased to 126 passengers. For the 50/50 scenarios, the number of passengers can be further increased, to 144 passengers for the kerosene first scenario, and 150 passengers for the hydrogen first scenario.

Looking at the comparison at 2500 km range in Figure 5.51, it can be observed that the number of passengers that can be taken on board within the fuselage length limit is increased significantly compared to 5000 km range for all scenarios. For both scenario 1 and 2, four additional rows of passengers can be taken on board. In this case, scenario 2 already meets the 150 passengers from the reference case. For the 50/50 scenarios, two additional rows of passengers can be taken on board compared to 5000 km range. Compared to 5000 km, the passenger count where the fuselage length limit is exceeded lies closer together at the reduced range of 2500 km.

This comparison shows that the employment of a dual-fuel configuration with hydrogen accompanied by kerosene or SAF can reduce the operational penalty regarding the number of passengers that can be taken on board compared to flying solely on hydrogen, especially when requiring a longer flight range from the aircraft.

---

[6] `https://customer.janes.com/`

6

Conclusion & Recommendations

6.1. Conclusion

In this study, the impact of the implementation of a dual-fuel propulsion system on the performance of a narrowbody tube and wing turbofan aircraft was investigated. The aim was to evaluate how dual-fuel capability affects aircraft design, fuel usage, and operational performance, and to determine whether such a configuration can function as an effective intermediate step between conventional kerosene operation and full hydrogen aviation. For this purpose, a parametric aircraft model was developed using the commercial ParaPy Python package, in which Class I aircraft sizing, mission analysis and Class II weight estimation were combined. Based on the results from comparing different scenarios and performing sensitivity analyses, several conclusions can be drawn.

First of all, the fuselage length is the main design parameter influenced by the implementation of a hydrogen tank. Across all scenarios, fuselage length increases due to the lower volumetric energy density of hydrogen, but the extent of this increase depends strongly on the share of hydrogen to be used in the mission. At 2500 km range, the fuselage length remained closer to the kerosene baseline than was the case at 5000 km range. This shows that dual-fuel operation can partially mitigate the volume penalty typically seen in full hydrogen concepts.

Secondly, the comparison of the different scenarios allows a clear distinction between the effects of hydrogen and kerosene usage on MTOW and fuel weight. This shows that an increase in the amount of hydrogen that is used results in a strong reduction of total fuel weight, due to a reduction in the use of the heavier kerosene. However, the addition of the hydrogen tank and fuselage extension causes the OEW to increase significantly with increasing use of hydrogen. Combined with the decreasing overall fuel weight, the MTOW of the aircraft concepts does not change significantly, but shows a small decrease. This is the case for both the 5000 and 2500 km range. The sensitivity analysis on varying the fuel split in cruise confirms the fact that an increase in hydrogen use causes a decrease in total fuel weight, but an increase in OEW caused by the hydrogen tank and fuselage, and, therefore, the MTOW to stay around similar values.

Thirdly, an increase in the use of hydrogen increases the tank-to-wake (in-flight) specific energy consumption (SEC), due to the higher energy content per kilogram of hydrogen compared to kerosene. Taking into account the well-to-tank energy required to produce hydrogen, the total SEC is increased even further. Considering equivalent CO_2 emissions from tank-to-wake, the increase in hydrogen use has the potential to reduce the CO_2 emissions compared to a full kerosene aircraft concept. However, when considering the total equivalent CO_2 emissions of the use of both fuels, results show that potential reductions of the equivalent CO_2 emissions largely depends on the equivalent emissions from hydrogen production. Considering hydrogen production from a world-average electricity grid that is decarbonising over the years, results show that reduction of equivalent emissions compared to a kerosene baseline is only achievable in 2050. However, partly operating on kerosene actually results in a reduction in equivalent CO_2 emissions compared to a full hydrogen aircraft concept.

Finally, the sensitivity analysis shows that the required range and passenger capacity strongly influence the aircraft design. The results demonstrate that employing dual-fuel operation helps limit the necessary passenger reduction when a fuselage length constraint is imposed. For a 45 meter fuselage limit, the 50/50 hydrogen-kerosene scenarios remained close to 150 passengers at 5000 km range, whereas the full hydrogen aircraft is limited to 114 passengers and the kerosene-reserve scenario to 126 passengers. When the range requirement is reduced to 2500 km, the passenger penalty decreases for full hydrogen flight. Dual-fuel operation still allows for additional passengers within the fuselage length limit, although the advantage over the full hydrogen concept becomes smaller at this shorter range.

Combining the findings presented above, it can be concluded that the implementation of a dual-fuel propulsion system on hydrogen and kerosene mainly affects the aircraft design through an increase in fuselage length due to the integration of a hydrogen tank. The results show that this effect varies strongly with hydrogen share and required range, and that dual-fuel operation can partially mitigate the fuselage growth typically seen in full hydrogen concepts. The use of hydrogen reduces total fuel weight, while the addition of the tank and fuselage extension increases OEW. Because these two effects counteract one another, the MTOW shows only a small decrease across all scenarios at both 2500 km and 5000 km range. Regarding emissions, the equivalent CO_2 tank-to-wake emissions decrease with increasing hydrogen use, but the well-to-tank energy required for hydrogen production can lead to higher overall equivalent emissions when production relies on electricity with significant carbon impact. Only under 2050 grid assumptions do all hydrogen-containing scenarios outperform the kerosene baseline in well-to-wake emissions, while dual-fuel operation shows a clear advantage over full-hydrogen concepts in the nearer term. Finally, dual-fuel aircraft can limit the passenger reduction required under a fuselage length constrained, especially at longer missions. This indicates that dual-fuel operation can improve operational flexibility and payload capability compared to full hydrogen aircraft, while still offering a meaningful step towards long-term decarbonisation of the aviation industry.

6.2. Recommendations for Future Research

For the work in this study, assumptions were made and limitations present. Based on these, several recommendations for future research can be made.

Generally, more detailed analysis of components in the presented methodology will aid in more certain conclusions about dual-fuel aircraft configurations to be drawn. First of all, it is recommended to include higher fidelity aerodynamic modelling, taking into lift and drag contributions of high-lift devices and landing gear. Next to that, it is recommended to obtain the drag polar at varying flight conditions throughout the mission analysis, such as at take-off and landing, and at reserve and loiter conditions. This would lead to a more accurate estimate of the fuel consumption in the mission analysis. Also potential aeroelastic effects from reduced fuel storage in the wings on the aerodynamics are interesting to investigate.

With a more accurate fuel weight estimation, it would also be of added value to incorporate higher fidelity wing and fuselage weight estimations. Aspects that would be useful to take into account could be, but are not limited to: crash structures around the hydrogen tank, safety margins and systems around the hydrogen tank, the effect of a hydrogen tank on the local fuselage structure and structural implications of reduced fuel storage in the wings. Also, the sizing of the hydrogen tank structure and insulation through a pressure build-up model is recommended to obtain a higher fidelity estimation of the tank model.

In terms of the estimation of fuel consumption, future research could investigate component level implications of a turbofan that can operate on both on hydrogen and kerosene or SAF, such as the combustion chamber geometry, fuel injection, and thermal management and the effect this has on fuel consumption estimations used in the mission analysis. Also, the implications of in-flight fuel switching on the aircraft engine and other systems are recommended to further investigate.

Emissions are currently evaluated for kerosene. Another recommendation for future research is to incorporate SAF and investigate how this affects lifecycle energy consumption and emissions. Next to that, it is recommended to investigate the cost aspect of hydrogen, SAF and kerosene, as well as to further investigate the effect on climate impact from dual-fuel use based on in-flight emissions.

Finally, looking at the overall design methodology, the model is currently set up in such a way that an aircraft concept is created bottom-up based on the inputs and requirements given to the model. It would be interesting for future research to incorporate elements from a top-down design approach. Examples would be to specify a priori a limit on the length of the fuselage or the number of passengers, and to let the design tool explore possible dual-fuel concepts and fuel split specifications. Linked to this, the recommendation is made to incorporate an optimisation around the design methodology that can optimise for different objectives, such as lowest lifecycle emissions, or minimal weight. Next to that, a clear limitation in the current set up of the design model lies in the presence of an empty hydrogen tank in the aircraft model even if no hydrogen use is specified. This makes comparison to a kerosene baseline aircraft less straightforward and it is thus recommended that this limitation is addressed in future developments and research.

References

[1] A.G. Rao, F. Yin, and H.G.C. Werij. “Energy Transition in Aviation: The Role of Cryogenic Fuels”. In: *Aerospace* 7.12 (Dec. 2020), p. 181. ISSN: 2226-4310. DOI: `10.3390/aerospace7120181`.

[2] D.S. Lee et al. “The contribution of global aviation to anthropogenic climate forcing for 2000 to 2018”. In: *Atmospheric Environment* 244 (Jan. 2021), p. 117834. ISSN: 13522310. DOI: `10.1016/j.atmosenv.2020.117834`.

[3] Fuel Cells and Hydrogen 2 Joint Undertaking. *Hydrogen-powered aviation: A fact-based study of hydrogen technology, economics, and climate impact by 2050*. Publications Office, 2020. DOI: `10.2843/471510`.

[4] E.J. Adler and J.R.R.A. Martins. “Energy demand comparison for carbon-neutral flight”. In: *Progress in Aerospace Sciences* 152 (Jan. 2025), p. 101051. ISSN: 03760421. DOI: `10.1016/j.paerosci.2024.101051`.

[5] E.J. Adler and J.R.R.A. Martins. “Hydrogen-powered aircraft: Fundamental concepts, key technologies, and environmental impacts”. In: *Progress in Aerospace Sciences* 141 (Aug. 2023), p. 100922. ISSN: 0376-0421. DOI: `10.1016/j.paerosci.2023.100922`.

[6] E. Cabrera and J.M.M. De Sousa. “Use of Sustainable Fuels in Aviation—A Review”. In: *Energies* 15.7 (Mar. 2022), p. 2440. ISSN: 1996-1073. DOI: `10.3390/en15072440`. (Visited on 01/29/2025).

[7] S. Tiwari, M.J. Pekris, and J.J. Doherty. “A review of liquid hydrogen aircraft and propulsion technologies”. In: *International Journal of Hydrogen Energy* 57 (Feb. 2024), pp. 1174–1196. ISSN: 03603199. DOI: `10.1016/j.ijhydene.2023.12.263`.

[8] B. Graver, PhD., D. Rutherford, PhD., and S. Zheng. *CO2 emissions from commercial aviation: 2013, 2018, and 2019*. Tech. rep. The International Council on Clean Transportation, Oct. 2020. URL: `https://theicct.org/wp-content/uploads/2021/06/CO2-commercial-aviation-oct2020.pdf` (visited on 02/03/2025).

[9] European Commission: Directorate-General for Mobility and Transport and European Commission: Directorate-General for Research and Innovation. *Flightpath 2050 – Europe’s vision for aviation – Maintaining global leadership and serving society’s needs*. Publications Office, 2011. URL: `https://data.europa.eu/doi/10.2777/50266` (visited on 01/14/2025).

[10] E.S. van der Sman et al. “Destination 2050”. en. In: (2020). Publisher: Netherlands Aerospace Centre NLR. URL: `http://hdl.handle.net/10921/1555` (visited on 01/27/2025).

[11] *Elysian Aircraft*. URL: `https://www.elysianaircraft.com` (visited on 01/28/2025).

[12] *Maeve*. URL: `https://maeve.aero/` (visited on 01/28/2025).

[13] *Heart Aerospace | Electrifying regional air travel*. URL: `https://heartaerospace.com/` (visited on 01/28/2025).

[14] G. Çınar. *Electric planes are coming: Short-hop regional flights could be running on batteries in a few years*. Sept. 2022. URL: `http://theconversation.com/electric-planes-are-coming-short-hop-regional-flights-could-be-running-on-batteries-in-a-few-years-190098` (visited on 01/28/2025).

[15] *Velis Electro*. URL: `https://www.pipistrel-aircraft.com/products/velis-electro/` (visited on 01/28/2025).

[16] D. Verstraete. “The Potential of Liquid Hydrogen for long range aircraft propulsion”. PhD Thesis. Cranfield University, Apr. 2009. URL: `https://dspace.lib.cranfield.ac.uk/items/dc023873-db96-4dd6-882b-835ea7cbf3d0` (visited on 01/06/2025).

[17] S.S. Jagtap, P.R.N. Childs, and M.E.J. Stettler. “Performance sensitivity of subsonic liquid hydrogen long-range tube-wing aircraft to technology developments”. In: *International Journal of Hydrogen Energy* 50 (Jan. 2024), pp. 820–833. ISSN: 03603199. DOI: `10.1016/j.ijhydene.2023.07.297`.

[18] M. Prewitz, J. Schwärzer, and A. Bardenhagen. “Potential analysis of hydrogen storage systems in aircraft design”. In: *International Journal of Hydrogen Energy* 48.65 (July 2023), pp. 25538–25548. ISSN: 03603199. DOI: `10.1016/j.ijhydene.2023.03.266`.

[19] G.L. Mills, B. Buchholtz, and A. Olsen. “Design, fabrication and testing of a liquid hydrogen fuel tank for a long duration aircraft”. In: Spokane, Washington, USA, 2012, pp. 773–780. DOI: `10.1063/1.4706990`.

[20] *HyPoint partners with GTL to extend zero-emission flight with ultralight liquid hydrogen tanks*. Jan. 2025. URL: `https://www.compositesworld.com/news/hypoint-partners-with-gtl-to-extend-zero-emission-flight-with-ultralight-liquid-hydrogen-tanks` (visited on 02/02/2025).

[21] V. Cipolla et al. “A Parametric Approach for Conceptual Integration and Performance Studies of Liquid Hydrogen Short–Medium Range Aircraft”. In: *Applied Sciences* 12.14 (July 2022), p. 6857. ISSN: 2076-3417. DOI: `10.3390/app12146857`.

[22] S.S. Jagtap, P.R.N. Childs, and M.E.J. Stettler. “Energy performance evaluation of alternative energy vectors for subsonic long-range tube-wing aircraft”. In: *Transportation Research Part D: Transport and Environment* 115 (Feb. 2023), p. 103588. ISSN: 13619209. DOI: `10.1016/j.trd.2022.103588`.

[23] G. Onorato, P. Proesmans, and M.F.M. Hoogreef. “Assessment of hydrogen transport aircraft: Effects of fuel tank integration”. In: *CEAS Aeronautical Journal* 13.4 (Oct. 2022), pp. 813–845. ISSN: 1869-5582, 1869-5590. DOI: `10.1007/s13272-022-00601-6`.

[24] J. Huete and P. Pilidis. “Parametric study on tank integration for hydrogen civil aviation propulsion”. In: *International Journal of Hydrogen Energy* 46.74 (Oct. 2021), pp. 37049–37062. ISSN: 03603199. DOI: `10.1016/j.ijhydene.2021.08.194`.

[25] A. Ebrahimi et al. “A review on liquid hydrogen fuel systems in aircraft applications for gas turbine engines”. In: *International Journal of Hydrogen Energy* 91 (Nov. 2024), pp. 88–105. ISSN: 03603199. DOI: `10.1016/j.ijhydene.2024.10.121`.

[26] F. Healy, D. Gu H.and Rezgui, and J. Cooper. “Conceptual Design of Hydrogen-Powered Aircraft: High Aspect Ratio Wings and Floating Wingtips”. In: Florence: ICAS Proceedings, Sept. 2024. URL: `https://www.scopus.com/record/display.uri?eid=2-s2.0-85208784047&origin=inward&txGid=edb16f2dc171039427bb9ce4d7e28c00` (visited on 12/18/2024).

[27] H. Gu et al. “Sizing of High-Aspect-Ratio Wings with Folding Wingtips”. In: *Journal of Aircraft* 60.2 (Mar. 2023), pp. 461–475. ISSN: 0021-8669, 1533-3868. DOI: `10.2514/1.C036908`.

[28] D.E. Calderon et al. “Sizing High-Aspect-Ratio Wings with a Geometrically Nonlinear Beam Model”. In: *Journal of Aircraft* 56.4 (July 2019), pp. 1455–1470. ISSN: 1533-3868. DOI: `10.2514/1.C035296`.

[29] K. Barabanova. *ZeroAvia Flight Testing Hydrogen-Electric Powerplant*. Jan. 2023. URL: `https://zeroavia.com/flight-testing/` (visited on 01/28/2025).

[30] B. Sampson. *Flight testing of Universal Hydrogen’s fuel cell test aircraft starts*. Sept. 2023. URL: `https://www.aerospacetestinginternational.com/news/electric-hybrid/flight-test-campaign-starts-for-universal-hydrogens-fuel-cell-test-aircraft.html` (visited on 01/28/2025).

[31] *DLR - Zero-emission air transport*. URL: `https://www.dlr.de/en/latest/news/2016/20160929_zero-emission-air-transport-first-flight-of-four-seat-passenger-aircraft-hy4_19469` (visited on 01/28/2025).

[32] A. Baroutaji et al. “Comprehensive investigation on hydrogen and fuel cell technology in the aviation and aerospace sectors”. In: *Renewable and Sustainable Energy Reviews* 106 (May 2019), pp. 31–40. ISSN: 13640321. DOI: `10.1016/j.rser.2019.02.022`.

[33] V. Sosounov and V. Orlov. “Experimental turbofan using liquid hydrogen and liquid natural gas as fuel”. In: *26th Joint Propulsion Conference*. Orlando,FL,U.S.A.: American Institute of Aeronautics and Astronautics, July 1990. DOI: `10.2514/6.1990-2421`.

[34] N. Bovenizer. *Rolls-Royce successfully tests hydrogen in take-off engine conditions*. Sept. 2023. URL: `https://www.airport-technology.com/news/rolls-royce-tests-hydrogen-take-off-conditions/` (visited on 01/28/2025).

[35] *Airbus and CFM International to pioneer hydrogen combustion technology | Airbus*. Feb. 2022. URL: `https://www.airbus.com/en/newsroom/press-releases/2022-02-airbus-and-cfm-international-to-pioneer-hydrogen-combustion` (visited on 01/28/2025).

[36] G. Dahl and F. Suttrop. “Engine control and low-NOx combustion for hydrogen fuelled aircraft gas turbines”. In: *International Journal of Hydrogen Energy* 23.8 (Aug. 1998), pp. 695–704. ISSN: 03603199. DOI: `10.1016/S0360-3199(97)00115-8`.

[37] C. Marek, T. Smith, and K. Kundu. “Low Emission Hydrogen Combustors for Gas Turbines Using Lean Direct Injection”. In: *41st AIAA/ASME/SAE/ASEE Joint Propulsion Conference & Exhibit*. Tucson, Arizona: American Institute of Aeronautics and Astronautics, July 2005. ISBN: 978-1-62410-063-5. DOI: `10.2514/6.2005-3776`.

[38] S.S. Jagtap, P.R.N. Childs, and M.E.J. Stettler. “Conceptual design-optimisation of a subsonic hydrogen-powered long-range blended-wing-body aircraft”. In: *International Journal of Hydrogen Energy* 96 (Dec. 2024), pp. 639–651. ISSN: 03603199. DOI: `10.1016/j.ijhydene.2024.11.331`.

[39] G. D. Brewer et al. *Study of Fuel Systems for LH2-Fueled Subsonic Transport Aircraft*. Contractor Report NASA-CR-145369-VOL-1. NASA Langley Research Center, July 1978. URL: `https://ntrs.nasa.gov/citations/19780023142` (visited on 02/02/2025).

[40] U.C.J. Rischmüller et al. “Conceptual Design of a Hydrogen-Hybrid Dual-Fuel Regional Aircraft Retrofit”. In: *Aerospace* 11.2 (Jan. 2024), p. 123. ISSN: 2226-4310. DOI: `10.3390/aerospace11020123`.

[41] D. Debney et al. *Zero-Carbon Emission Aircraft Concepts*. Tech. rep. Aerospace Technology Institute, Mar. 2022. URL: `https://www.ati.org.uk/wp-content/uploads/2022/03/FZO-AIN-REP-0007-FlyZero-Zero-Carbon-Emission-Aircraft-Concepts.pdf`.

[42] B. Rietdijk and M. Selier. “Architecture Design for a Commercially Viable Hydrogen-Electric Powered Retrofitted Regional Aircraft”. In: 2024. URL: `https://www.scopus.com/inward/record.uri?eid=2-s2.0-85208780853&partnerID=40&md5=dff1a609c1d3e0b29bbeae88d0fbe090` (visited on 01/30/2025).

[43] D. Verstraete. “Long range transport aircraft using hydrogen fuel”. In: *International Journal of Hydrogen Energy* 38.34 (Nov. 2013), pp. 14824–14831. ISSN: 03603199. DOI: `10.1016/j.ijhydene.2013.09.021`.

[44] W.F. Lammen et al. *Hydrogen-powered propulsion aircraft: conceptual sizing and fleet level impact analysis*. Tech. rep. NLR-TP-2022-233. Netherlands Aerospace Centre, Sept. 2022.

[45] *Hydrogen Conversion Turbofan*. URL: `https://luchtvaartintransitie.nl/en/project-item/hydrogen-ombouw-turbofan/` (visited on 01/30/2025).

[46] *Dash 8 seat map | Qantas NL*. URL: `https://www.qantas.com/nl/en/qantas-experience/onboard/seat-maps/dash-8.html` (visited on 01/30/2025).

[47] *Fokker Next Gen at Farnborough 2024*. URL: `https://www.fokkernextgen.com/farnborough-2024` (visited on 01/30/2025).

[48] *E195-E2 Embraer Commercial Jet*. URL: `https://www.embraercommercialaviation.com/commercial-jets/e195-e2-commercial-jet/` (visited on 01/30/2025).

[49] P. Proesmans and R. Vos. “Comparison of Future Aviation Fuels to Minimize the Climate Impact of Commercial Aircraft”. In: *AIAA AVIATION 2022 Forum*. Chicago, IL & Virtual: American Institute of Aeronautics and Astronautics, June 2022. ISBN: 978-1-62410-635-4. DOI: `10.2514/6.2022-3288`.

[50] J.R. Smith and E. Mastorakos. “An energy systems model of large commercial liquid hydrogen aircraft in a low-carbon future”. In: *International Journal of Hydrogen Energy* 52 (Jan. 2024), pp. 633–654. ISSN: 03603199. DOI: `10.1016/j.ijhydene.2023.04.039`.

[51] A.G. Rao, F. Yin, and J.P. van Buijtenen. “A hybrid engine concept for multi-fuel blended wing body”. In: *Aircraft Engineering and Aerospace Technology* 86.6 (Sept. 2014). Ed. by Riti Singh, pp. 483–493. ISSN: 0002-2667. DOI: `10.1108/AEAT-04-2014-0054`.

[52] V. Grewe et al. “Assessing the climate impact of the AHEAD multi-fuel blended wing body”. In: *Meteorologische Zeitschrift* 26.6 (Dec. 2017), pp. 711–725. ISSN: 0941-2948. DOI: `10.1127/metz/2016/0758`.

[53] S.R. Yelugoti and W. Wang. “The combustion performance of sustainable aviation fuel with hydrogen addition”. In: *International Journal of Hydrogen Energy* 48.15 (Feb. 2023), pp. 6130–6145. ISSN: 03603199. DOI: `10.1016/j.ijhydene.2022.11.104`.

[54] H. Gürbüz et al. “The effect of euro diesel-hydrogen dual fuel combustion on performance and environmental-economic indicators in a small UAV turbojet engine”. In: *Fuel* 306 (Dec. 2021), p. 121735. ISSN: 00162361. DOI: `10.1016/j.fuel.2021.121735`.

[55] C. Reitmayr et al. “Experimental and Numerical Investigations of a Dual-Fuel Hydrogen–Kerosene Engine for Sustainable General Aviation”. In: Warrendale, Pennsylvania, United States, June 2024, pp. 2024–01–6001. DOI: `10.4271/2024-01-6001`.

[56] S. Seyam, I. Dincer, and M. Agelin-Chaab. “Investigation of two hybrid aircraft propulsion and powering systems using alternative fuels”. In: *Energy* 232 (Oct. 2021), p. 121037. ISSN: 03605442. DOI: `10.1016/j.energy.2021.121037`.

[57] *WET engine: MTU Aero Engines develops drive of the future with wet combustion*. URL: `https://www.mtu.de/newsroom/press/latest-press-releases/press-release-detail/wet-engine-mtu-aero-engines-develops-drive-of-the-future-with-wet-combustion/` (visited on 02/03/2025).

[58] *CAVENDISH*. URL: `https://clean-aviation.eu/cavendish` (visited on 02/03/2025).

[59] Embraer Commercial Aviation. *Future Aircraft Concepts*. URL: `https://embraercommercialaviationsustainability.com/concepts/#energia` (visited on 12/23/2025).

[60] J. Roskam. *Part I: Preliminary Sizing of Airplanes*. Airplane Design. 1985.

[61] J. Huete, D. Nalianda, and P. Pilidis. “Impact of tank gravimetric efficiency on propulsion system integration for a first-generation hydrogen civil airliner”. In: *The Aeronautical Journal* 126.1302 (Aug. 2022), pp. 1324–1332. ISSN: 0001-9240, 2059-6464. DOI: `10.1017/aer.2022.60`.

[62] E. Torenbeek. *Synthesis of Subsonic Airplane Design*. Dordrecht: Springer Netherlands, 1982. ISBN: 978-90-481-8273-2. DOI: `10.1007/978-94-017-3202-4`.

[63] G.D. Brewer. *Hydrogen Aircraft Technology*. 1st ed. Bosa Roca: CRC Press LLC, 1991. ISBN: 978-0-8493-5838-8.

[64] EASA. *Easy Access Rules for Large Aeroplanes (CS-25)*. Jan. 2023. URL: `https://www.easa.europa.eu/en/document-library/easy-access-rules/easy-access-rules-large-aeroplanes-cs-25`.

[65] L. Jenkinson, P. Simpkin, and D. Rhodes. *Civil Jet Aircraft Design*. Washington, DC: American Institute of Aeronautics and Astronautics, Inc., Jan. 1999. ISBN: 978-1-56347-350-0. DOI: `10.2514/4.473500`.

[66] R.L.A. de Jonge. “Development of a Knowledge- Based Engineering Application to Support Conceptual Fuselage Sizing and Cabin Configuration”. PhD thesis. Jan. 2017.

[67] J. Roskam. *Part III: Layout Design of Cockpit, Fuselage, Wing and Empennage: Cutaways and Inboard Profiles*. Airplane Design. 1986.

[68] R. Vos, J.A. Melkert, and B.T.C. Zandbergen. *AE1222-II Lecture on Fuselage Design*. Mar. 2018.

[69] J. Roskam. *Part II: Preliminary Configuration Design and Integration of the Propulsion System*. Airplane Design. 1985. ISBN: 978-1-884885-43-3.

[70] E. Torenbeek. *Advanced aircraft design: conceptual design, analysis, and optimization of subsonic civil airplanes*. Aerospace series. Chichester, West Sussex, United Kingdom: John Wiley & Sons Inc, 2013. ISBN: 978-1-118-56811-8. DOI: `10.1002/9781118568101`.

[71] D.P. Raymer. *Aircraft design: a conceptual approach*. 5. ed. AIAA education series. Reston, Va: AIAA, American Inst. of Aeronautics and Astronautics, 2012. ISBN: 978-1-60086-911-2.

[72] E. Obert. *Aerodynamic design of transport aircraft*. Amsterdam: IOS press, 2009. ISBN: 978-1-58603-970-7.

[73] H. Tran. “Efficient Modeling of Hybrid Electric Aircraft for Design and Performance Optimization Studies”. PhD thesis. Delft University of Technology, Dec. 2020.

[74] G.J.A. di Summa. “The Effect of the Internal Layout of Hydrogen Combustion Blended Wing Body Concepts on Performance”. MA thesis. Delft University of Technology, June 2025. URL: `https://resolver.tudelft.nl/uuid:21494bbc-7149-45bb-bad3-7d6a62408231`.

[75] N. Tarbah. “Developing a Framework for the Design of Hydrogen Fuel Cell Supply Architectures”. MA thesis. Delft University of Technology, June 2024. URL: `https://resolver.tudelft.nl/uuid:02440a00-fe95-4a13-9192-2f9277894c21`.

[76] IAE International Aero Engines AG. *IAE V2500*. 2024. URL: `https://prd-sc102-cdn.rtx.com/-/media/pw/products/commercial-jet-engines/v2500/files/ce_v2500_pcard.pdf?rev=1fbb81a571404d49bbcab203125208a3&hash=5936BE6BD8A4727C80234F19441E6154` (visited on 03/25/2025).

[77] EASA. *IAE 2500 Series Type-Certificate Data Sheet*. Dec. 2019. URL: `https://web.archive.org/web/20191231034604/https://www.easa.europa.eu/sites/default/files/dfu/IM%20E%20069%20Issue04_20191212.pdf` (visited on 03/25/2025).

[78] W.P.J. Visser. “Generic Analysis Methods for Gas Turbine Engine Performance”. Doctoral Thesis. Delft: Delft University of Technology, 2014. URL: `https://repository.tudelft.nl/file/File_83952476-0900-4200-88a0-c922f4c496e2?preview=1` (visited on 06/23/2025).

[79] A.W.X. Ang et al. “Performance analysis of an electrically assisted propulsion system for a short-range civil aircraft”. In: *Proceedings of the Institution of Mechanical Engineers, Part G: Journal of Aerospace Engineering* 233.4 (Mar. 2019), pp. 1490–1502. ISSN: 0954-4100, 2041-3025. DOI: `10.1177/0954410017754146`.

[80] O. Gur, W.H. Mason, and J.A. Schetz. “Full-Configuration Drag Estimation”. In: *Journal of Aircraft* 47.4 (July 2010), pp. 1356–1367. ISSN: 0021-8669, 1533-3868. DOI: `10.2514/1.47557`.

[81] F. Moëns. “A Fast Aerodynamic Model for Aircraft Multidisciplinary Design and Optimization Process”. In: *Aerospace* 10.1 (Dec. 2022), p. 7. ISSN: 2226-4310. DOI: `10.3390/aerospace10010007`.

[82] J. Roskam. *Part V: Component Weight Estimation*.

[83] M. Taflan, H. Smith, and J. Loughlan. “Structural sizing and mass estimation of transport aircraft wings with distributed, hydrogen, and electric propulsions”. In: *The Aeronautical Journal* 129.1333 (Mar. 2025), pp. 690–716. ISSN: 0001-9240, 2059-6464. DOI: `10.1017/aer.2024.117`.

[84] F. Oliviero. *AE3211-I Lecture on: Requirement Analysis and Design principles for A/C stability & control (Part 1)*.

[85] S. Howe, A.J. Kolios, and F.P. Brennan. “Environmental life cycle assessment of commercial passenger jet airliners”. In: *Transportation Research Part D: Transport and Environment* 19 (Mar. 2013), pp. 34–41. ISSN: 13619209. DOI: `10.1016/j.trd.2012.12.004`.

[86] B. Khandelwal et al. “Hydrogen powered aircraft : The future of air transport”. In: *Progress in Aerospace Sciences* 60 (July 2013), pp. 45–59. ISSN: 03760421. DOI: `10.1016/j.paerosci.2012.12.002`.

[87] M. Drela and H. Youngren. *AVL User Primer*. Feb. 2017. URL: `https://web.mit.edu/drela/Public/web/avl/` (visited on 11/23/2025).

[88] R. Elmendorp, R. Vos, and G. La Rocca. “A conceptual design and analysis method for conventional and unconventional airplanes”. In: *29th Congress of the International Council of the Aeronautical Sciences, ICAS 2014* (Jan. 2014).

[89] K. Risse et al. “Central Reference Aircraft data System (CeRAS) for research community”. In: *CEAS Aeronautical Journal* 7.1 (Mar. 2016), pp. 121–133. ISSN: 1869-5582, 1869-5590. DOI: `10.1007/s13272-015-0177-9`.

[90] J. Huete, D. Nalianda, and P. Pilidis. “Propulsion system integration for a first-generation hydrogen civil airliner?” In: *The Aeronautical Journal* 125.1291 (Sept. 2021), pp. 1654–1665. ISSN: 0001-9240, 2059-6464. DOI: `10.1017/aer.2021.36`.

[91] Rolls-Royce PLC. *Rolls-Royce Trent XWB*. 2015. URL: `https://www.rolls-royce.com/~/media/Files/R/Rolls-Royce/documents/civil-aerospace-downloads/High-Res-posters/High-Res-poster_Trent-XWB.pdf` (visited on 11/10/2025).

[92] MTU Aero Engines. *LEAP-1A/-1B*. URL: `https://www.mtu.de/engines/commercial-aircraft-engines/narrowbody-and-regional-jets/leap-1a/-1b/` (visited on 11/10/2025).